



UNIVERSITÀ DEGLI STUDI DI PADOVA

Dipartimento Di Ingegneria Dell'Informazione

Corso di Laurea Magistrale in Ingegneria Elettronica

TESI DI LAUREA

Impact of thermal and intermediate energy neutrons on the semiconductor memories for the CERN accelerators

Laureando:

Matteo Cecchetto

Relatore:

Prof. Simone Gerardin

CERN supervisor:

Dott. Rubén García Alía

10 Luglio 2017

Anno accademico 2016/2017

Abstract

(ENGLISH)

A wide quantity of SRAM memories are employed along the Large Hadron Collider (LHC), the main CERN accelerator, and they are subjected to high levels of ionizing radiations which compromise the reliability of these devices. The Single Event Effect (SEE) qualification for components to be used in the complex high-energy accelerator at CERN relies on the characterization of two cross sections: 200-MeV protons and thermal neutrons. However, due to cost and time constraints, it is not always possible to characterize the SEE response of components to thermal neutrons, which is often regarded as negligible for components without borophosphosilicate glass (BPSG). Nevertheless, as recent studies show, the sensitivity of deep sub-micron technologies to thermal neutrons has increased owing to the presence of Boron 10 as a dopant and contact contaminant. The very large thermal neutron fluxes relative to high-energy hadron fluxes in some of the heavily shielded accelerator areas imply that even comparatively small thermal neutron sensitivities could dominate the overall Single Event Upset (SEU) rate. For instance, in some locations that host electronic devices, the thermal neutrons fluence can be up to 15 times larger than that of the high-energy hadron. For this reason, in this work I explore the option of measuring the thermal neutron sensitivity through high-energy mixed field irradiations, in conditions with different ratios between the thermal and high-energy hadron fluxes. I studied SEU and SEL SRAM cross sections using the Cern High energy Accelerator Mixed-field (CHARM) facility, where a wide variety of accelerator environments can be reproduced by combining different test positions and shielding configurations. The mixed-field radiation environment simulated in the past with the FLUKA Monte Carlo tool was investigated in order to select a location with a large thermal neutron fluence compared with the equivalent high-energy hadron fluence. From this perspective, I selected a location with a strong contribution from thermal and intermediate energy neutrons and I characterized it, by combining FLUKA Monte Carlo simulations and the Radiation Monitor (RadMon) measurements. In order to vary the amount of thermal

neutrons in the selected position, I designed and built a box of boron carbide, a material that has a high capture cross section for thermal neutrons. After preliminary FLUKA simulations to outline the spectra outgoing the boron carbide absorber, I carried out the RadMon tests-analysis with the purpose of experimentally verifying the results. The former evidences that a large portion of the neutron spectra is fully absorbed below 1 eV and partially cut until 0.01 MeV, while hardly affecting the high-energy flux. Once the neutron test-position was calibrated, I tested and studied the upset and latch-up sensitivities of different SRAM memories to thermal neutrons and high-energy hadron. This investigation was made with differential measurements using the boron carbide box as a thermal neutrons absorber. One of the tested components was the ESA SEU Monitor, an SRAM-based radiation detector employed to prove the effectiveness of the differential approach and to assess the beam spatial uniformity. Moreover, to benchmark the cross sections results retrieved on the neutron-dominated position at CHARM, I tested the same memories in two facilities in Grenoble (France): a 14 MeV mono-energetic neutrons source and a reactor providing a thermal neutron spectrum for testing electronics. Since 14 MeV neutron beams are typically more accessible and cost-efficient than several hundred MeV protons at cyclotron facilities, this work also evaluates their possible use for deriving the saturation cross section, representative of the high-energy hadron response of candidate components. Furthermore I worked on an Americium-Beryllium neutron source at CERN to assess its possible use for SEU testing when CHARM is not available. After the calibration of the facility carried out with FLUKA simulations and ESA Monitor experimental measurements, I proved its potential employment for future tests.

Finally, I compared the mono-energetic neutron beam test approach results against those at CHARM, obtaining a highly satisfactory agreement between the memories cross sections measured in these facilities. In this way, CHARM is shown to successfully reproduce the conditions to obtain an SEE qualification compatible with that at standard mono-energetic facilities.

(ITALIANO)

Una grande quantità di memorie SRAM sono utilizzate all'interno del Large Hadron Collider (LHC), l'acceleratore principale del CERN e sono sottoposte ad alti livelli di radiazione ionizzante che compromette l'affidabilità di questi dispositivi. La qualificazione dei Single Event Effect (SEE) per quei componenti che saranno impiegati nel complesso dell'acceleratore ad alta energia del CERN si basa sulla caratterizzazione di due cross section: protoni a 200-MeV e neutroni termici. Tuttavia, a causa dei costi e restrizioni di tempo, non è sempre possibile caratterizzare la risposta ai SEE dei componenti per quanto concerne i neutroni termici, la quale è spesso considerata trascurabile per quei componenti privi di borofosfosilicati (BPSG). Tuttavia, come hanno mostrato recenti studi, la sensibilità ai neutroni termici in tecnologie molto scalate è aumentata a causa della presenza del Boro 10 come drogante e contaminante nei contatti. Gli estesi flussi di neutroni termici relativi agli adroni ad alta energia presenti in aree dell'acceleratore fortemente schermate, implica che anche relativamente basse sensibilità ai neutroni termici possono dominare l'intero tasso dei Single Event Upset (SEU). Ad esempio, in alcune alcove che ospitano dispositivi elettronici, la fluenza di neutroni termici può essere fino a 15 volte maggiore di quella dovuta dagli adroni ad alta energia. Per questo motivo, in questo lavoro ho esplorato la possibilità di misurare la sensibilità ai neutroni termici attraverso spettri misti di radiazione ionizzante, in condizioni con differenti rapporti tra flussi termici e adroni ad alta energia. Ho studiato le cross section di SRAM ai SEU e SEL utilizzando la Cern High energy Accelerator Mixed-field (CHARM) facility, dove un'ampia varietà di ambienti dell'acceleratore possono essere riprodotti combinando differenti posizioni di test e configurazioni di schermatura. Il campo di radiazione misto simulato in passato con il pacchetto FLUKA basato sul metodo Monte Carlo è stato analizzato allo scopo di selezionare una posizione con un'alta fluenza di neutroni termici in confronto agli adroni ad alta energia. In questa prospettiva, ho selezionato e caratterizzato una posizione con un forte contributo di neutroni termici e a energia intermedia tramite le simulazioni FLUKA e misure con il Radiation Monitor (RadMon). Con l'obiettivo di variare la quantità di neutroni termici sulla posizione selezionata, ho progettato e costruito un box di carburo di boro, un materiale che ha un'elevata cross section di cattura ai neutroni termici. Dopo delle preliminari simulazioni FLUKA per delineare lo spettro di particelle in uscita dal carburo di boro, ho effettuato i test-analisi con il RadMon allo scopo di verificare sperimentalmente i risultati. Le prime hanno evidenziato che una larga porzione di neutroni termici viene completamente assorbita sotto 1 eV e parzialmente tagliata fino a 0.01 MeV, mentre non vengono fortemente influenzati i flussi ad alta energia. Calibrata la

posizione dominata da neutroni, ho testato e studiato la sensibilità degli upset e latch-up di differenti memorie SRAM ai neutroni termici e adroni ad alta energia. Questa ricerca è stata effettuata con misure differenziali utilizzando il carburo di boro per assorbire i neutroni termici. Uno dei componenti studiati è stato l'ESA SEU Monitor, un rilevatore di radiazione SRAM che ho impiegato per dimostrare l'efficacia dell'approccio differenziale e valutare l'uniformità spaziale del campo di radiazione. Inoltre, per validare i risultati sulle cross section ricavate dalla posizione dominata da neutroni a CHARM, ho misurato le stesse memorie in due facility a Grenoble (Francia): una sorgente mono - energetica a 14 MeV e un reattore che fornisce uno spettro di neutroni termici per test di elettronica. Essendo i fasci a 14 MeV tipicamente più accessibili e convenienti rispetto ai ciclotroni a protoni con centinaia di MeV, questo lavoro valuta anche il loro possibile impiego per ricavare le cross section di saturazione, rappresentative della risposta agli adroni ad alta energia dei componenti. Inoltre ho lavorato con una sorgente di neutroni Americio-Berillio al CERN per valutare il suo possibile impiego per misure SEU quando CHARM non è disponibile. Dopo la calibrazione della facility eseguita con simulazioni FLUKA e misure sperimentali con l'ESA Monitor, ho dimostrato il suo potenziale utilizzo per test futuri.

Infine, ho confrontato i risultati utilizzando fasci di neutroni mono - energetici con quelli ottenuti a CHARM, ottenendo una concordanza estremamente soddisfacente tra le cross section delle memorie misurate in queste facility. In questo modo, CHARM ha dimostrato poter riprodurre le condizioni per ottenere una qualifica dei SEE compatibile con quella di facility standard mono-energetiche.

Contents

Abstract	iii
List of Abbreviations	ix
List of Symbols	xi
1 Introduction	1
2 Radiation environment at CHARM focusing on neutron-dominated positions	5
2.1 HEH, HEHeq, thermal neutrons, R-factor, cross section definitions	5
2.1.1 High-Energy Hadrons	5
2.1.2 Thermal neutrons	8
2.1.3 R-factor	9
2.1.4 Events and cross sections	9
2.2 CHARM introduction	10
2.2.1 TIMBER software	14
2.3 BLM signal analysis and operational use	16
2.3.1 Beam Loss Monitor detector	16
2.3.2 BLM Analysis	17
2.3.3 Impact of material in primary beam on CHARM intensity	21
2.4 Boron carbide thermal neutrons absorber and its impact on M0	24
2.4.1 Boron carbide tiles	24
2.5 Radiation environment at G0 and M0	26
2.5.1 M0 calibration and RadMon system	28
2.5.2 Mixed-field radiation calculation and monitoring	33
2.5.3 FLUKA simulations	37
2.6 Comparison with shielded areas in accelerator and atmospheric spectrum	41
2.6.1 Radiation environment in the LHC	41

3	SEE test results at CHARM for thermal and high-energy neutrons	45
3.1	Measured effects, components tests and experimental setups	45
3.1.1	SEU and SEL effects	45
3.1.2	Tested components	48
3.2	Proposed mixed-field differential approach	56
3.3	SEU results	61
3.4	SEL results	64
3.4.1	Events and fluence	70
4	Radiation neutron tests in other facilities	73
4.0.1	Tested memories and experimental setup	74
4.0.2	Flux and homogeneity cross-calibration with the ESA Monitor . .	76
4.1	Thermal neutrons: ILL	76
4.1.1	ILL results	82
4.2	14 MeV neutrons: LPSC	83
4.2.1	LPSC results	88
4.3	Am-Be neutron source and spectrum	90
5	SEE results: standard test approach versus CHARM	97
6	Conclusions and Outlook	101
	Appendix	105
	Acknowledgements	117
	Bibliography	117

List of Abbreviations

B4C Boron carbide

BLM Beam Loss Monitor

CHARM Cern High-energy AcceleRator Mixed-filed

COTS Component On The Shelf

FLUKA FLUktuierende KAskade (Monte Carlo simulation package)

IRRAD cern IRRADiation facilities

HEH High energy Hadrons

HEHeq High energy Hadrons equivalent

POT Proton on Target

PS Proton Synchrotron

R R-factor (ThN/HEH)

RadMon Radiation Monitor

SEC Secondary Emission Chamber

SEE Single Event Effect

SEU Single event Upset

SEL Single event Latch-up

ThN Thermal neutrons

ThNeq Thermal neutrons equivalent

TIMBER Timeseries Information Mastering: Browsing, Extraction and Rendering

UTC Coordinated Universal Time

SEL Single event Latch-up

List of Symbols

σ - Cross section [cm^2] or [cm^2/bit]

Φ - General fluence [cm^{-2}]

φ - Flux [cm^{-2}/s]

Φ_{HEH} - High Energy Hadron fluence

Φ_{HEHeq} - High Energy Hadron equivalent (intermediate-energy neutrons) fluence

Φ_{thn} - Thermal neutron fluence

R - R factor (Thermal to HEH fluences ratio)

R_{eq} - R equivalent factor (Thermal to HEH equivalent fluences ratio)

N_{SEE} - Number of Single Event Effects

Chapter 1

Introduction

CERN, the European Organization for Nuclear Research, is the biggest research center for particle physics in the world situated in Switzerland and France. It was born in 1954 with the synchrocyclotron (SC), the first 600 MeV proton accelerator that detected the pion, suggested by Enrico Fermi. Over the years CERN became bigger and bigger by hosting more and more large and powerful accelerators. Nowadays the complex is formed by a chain of six accelerators as shown in Figure 1.1: LINAC, Booster, LEIR, PS, SPS and finally the Large Hadron Collider (LHC) with its 27 km of circumference and located 100 m underground. Is thanks to the latter that in 2012 the Higgs boson, in honour of Peter Higgs was discovered, ensuring the consistency of the standard model. Moving from one accelerator to the other, the energy of the proton beam increases up to 7 TeV through a radio frequency cavity and the beam focus is maintained by means of magnets, controlled by a very precise current. In the LHC, the beams pass in opposite directions through two vacuum pipes in order to collide inside huge detectors like ATLAS, built in a cave with an area comparable to that of a cathedral. To reduce as much as possible the power dissipation for the 12000 A of current required from the magnets, an impressive cryogenic system is installed to cool down the complex up to -270°C . As can be alleged, a wide quantity of electronic devices are needed for the operation of the entire structure and a great effort on the part of engineers and physicists is required to ensure the reliability of the machine. Scientists from all the world are working together on a vast amount of experiments which application fields, ranging from the physics, electronics, mechanics, chemistry and not least, medicine. The main purpose is to answer the questions concerning the origin of the universe and how the most elementary particles were combined for the creation of nuclei, atoms, molecules and increasingly complex systems. Nevertheless, inventions which have every day life implications derive from CERN like the World Wide Web, technological revolution developed with the purpose of communicating among scientists spread around

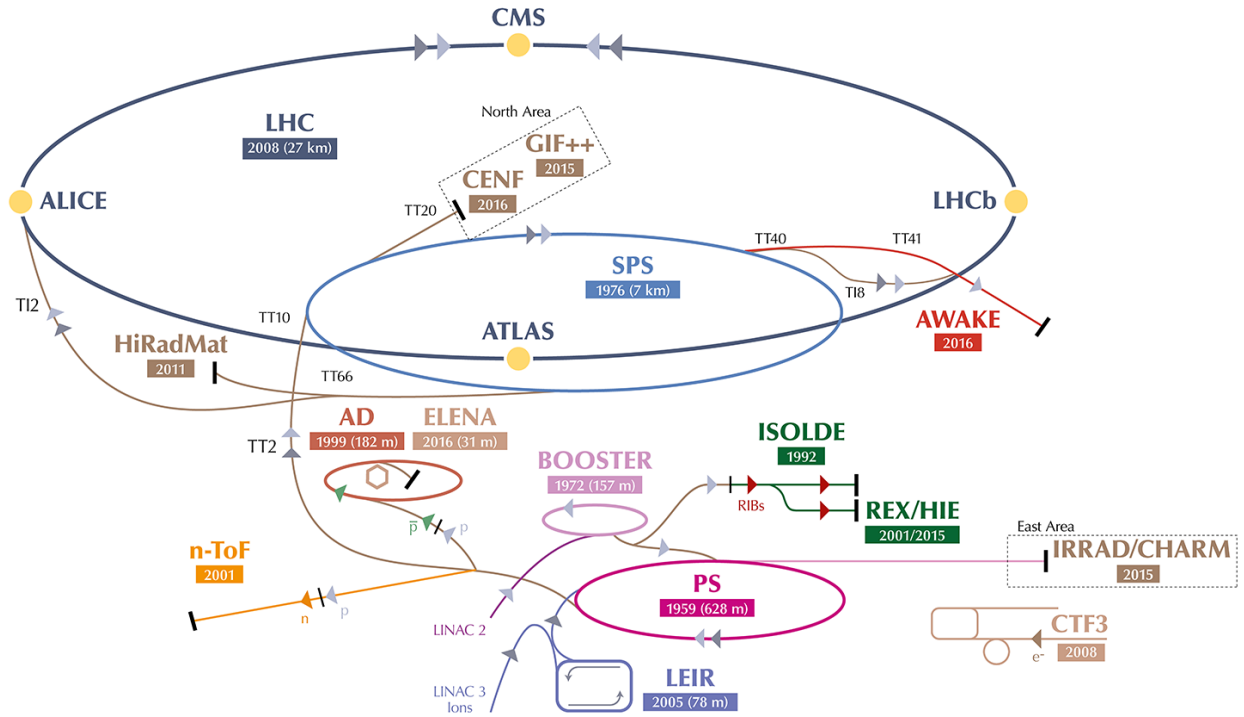


Figure 1.1: CERN accelerators; to the right the CHARM facility employed in this work, supplied from the PS.

the world; or the PET in medicine, owe its early foundation stages at CERN. One of the important challenges relies on the correct functioning of the electronic devices subjected to a very intense and complex radiation environment, which varies on the basis of the type of particle and its carried energy. Just to give an example, SRAM, FPGA, power MOSFET, microprocessors, embedded systems, etc. employed in the accelerators must to be radiation-resistant when installed along the machines. However in most of the cases Commercial Off The Shelf components (COTS) are the best candidates due to their conditions, as opposed to radiation hardened devices and not least for their high performance and availability on the market. Beside they need to be tested in order to assess their proper operation under radiation environment. By aiming to these studies, the Radiation to Electronic (R2E) project at CERN is working on. To carry out these verifications there is the need of knowing the radiation environment for the tests, achieved with experimental measurements with dedicated devices such as the Radiation Monitor (RadMon) system and the comparison of these against FLUKA simulations. Indeed from the latter we can have an estimation of the expected radiation fluences, from which particles the contribution is associated, which energy they are carrying and benchmark these information with the experimental data.

- chapter 2 outlines the main quantities and definitions used throughout this work. The CHARM facility is introduced and sub-chapter 2.3 shows the correlation between the mixed-field levels and the primary beam intensity through the study of the BLM ionization chamber signal. The boron carbide material is described and used for the following calibration of the neutron-dominated position M0 at CHARM by employing the RadMon system and FLUKA simulations. In addition, chapter 2.6 presents a brief comparison between some accelerator environments and those that CHARM can reproduce, as well as the agreement as regards ground level applications, since its neutron spectrum is similar to that present at sea level.
- chapter 3, after an overview about the tested memories and experimental setups reports the high-energy hadron and thermal neutron cross section results obtained at CHARM regarding SEU and SEL tests with SRAM memories.
- chapter 4 provides the descriptions, setups and results carried out in three different facilities, a thermal neutrons reactor (25 meV), a 14 MeV mono-energetic neutron source and the Americium-Beryllium neutron source (up to 10 MeV).
- chapter 5 compares the cross section results obtained at CHARM against those of the other facilities with a brief summary.
- chapter 6 finally summarizes the the objective achieved with this thesis work.

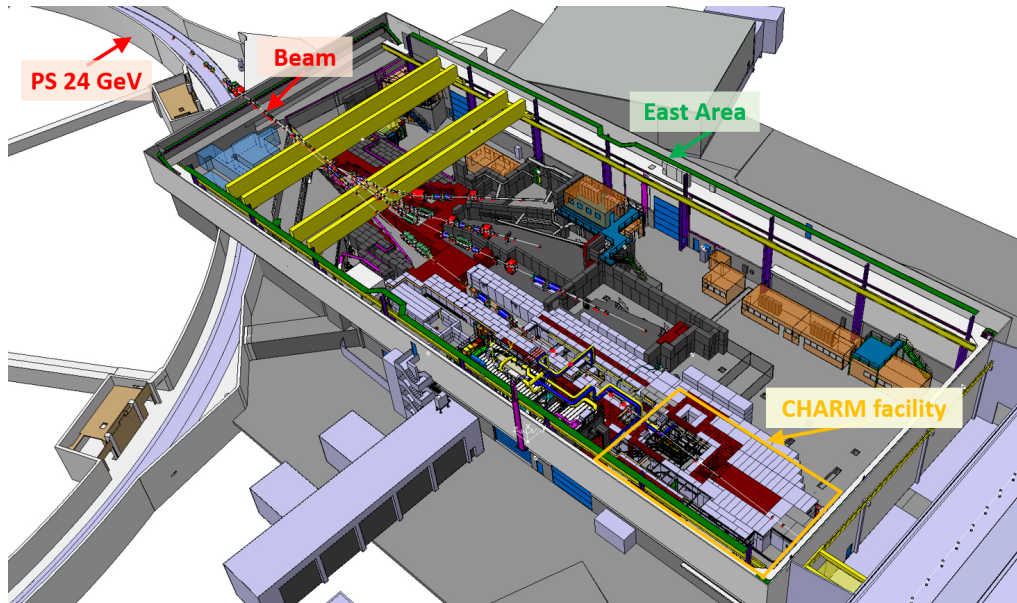


Figure 1.2: 3D view of the PS beam arriving in the East Area facilities with CHARM at the end.

Chapter 2

Radiation environment at CHARM focusing on neutron-dominated positions

2.1 HEH, HEHeq, thermal neutrons, R-factor, cross section definitions

2.1.1 High-Energy Hadrons

Hadrons are subatomic particle composed by quark and antiquark and according to their composition they can be protons, neutrons, pions or kaons. With High-Energy Hadrons (HEH) term, are designed hadron that carry a large quantity of energy the order of MeV. Hadrons can induce Single Event Effects because they produce inelastic nuclear interactions in matter. However, charged hadrons (pprotons, pions, kaons) under 20 MeV are in general considered as not being able to generate SEEs either because they can not go through the component package or due to their very low energy deposition. The Single Event Effect (SEE) qualification approach is based on the characterization of two individual cross sections: 200-MeV protons (or equivalents fluxes at high-energy) and thermal neutrons with a kinetic energy of 0.025-eV. Based on these values, the SEE response as a function of energy is assumed to be a step function at 20 MeV as regards charged hadrons; a Weibull-like response for intermediate energy neutrons (0.2-20 MeV) and a function decreasing as $E^{-\frac{1}{2}}$ for thermal neutrons, as expected for processes dominated by neutron capture. An easy interpretation of this behaviour can be explained saying that starting from the thermal neutron, more the energy increases, faster is the neutron so that its capture probability decreases until a point after which multiple mechanisms

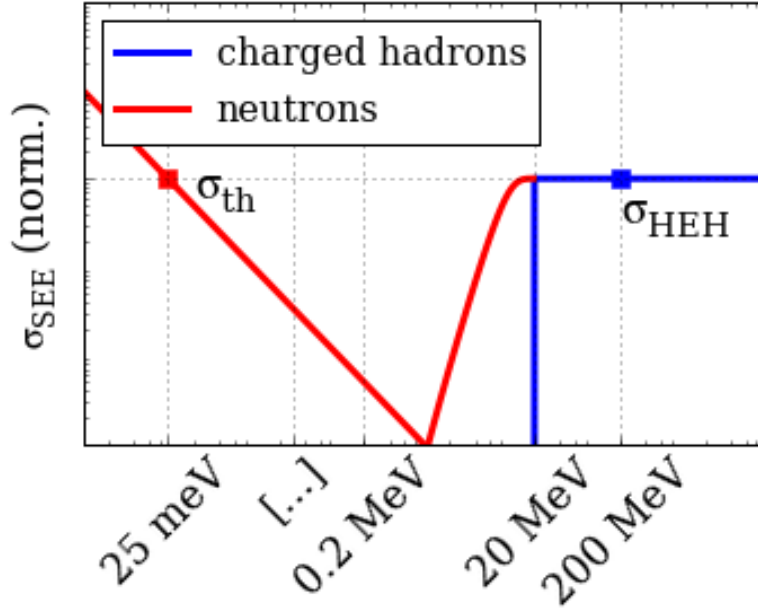


Figure 2.1: Charged hadrons and thermal neutrons cross sections as a function of the energy.

are activated and the cross section starts again to raise. Reached the 20 MeV of energy, hadrons have roughly a constant probability to be captured independently from the energy. The response introduced above is schematically shown in figure 2.1, where 200 MeV is considered to be an energy well representative of the energy-saturated SEE cross section. The response can then be folded with the mixed-field spectra, yielding the expected operational SEE rate. More details concerning this approach can be found in [6].

The sum of the differential flux of hadrons above 20 MeV is defined as the high-energy hadron (HEH) flux and measured in $\left[\frac{\text{particles}}{\text{cm}^2 \cdot \text{s}}\right]$. At the CHARM facility employed for the experiment (described in chapter 2.2), the contribution to the hadrons is basically due to protons, neutrons and pions equally regarded in the HEH flux because above 20 MeV they retain the same probability of inducing SEUs. Therefore:

$$\varphi_{HEH} = \int_{20\text{MeV}}^{\infty} \sum_{i=1}^3 \frac{d\varphi_i(E)}{dE} dE = \int_{20\text{MeV}}^{\infty} \frac{d\varphi_{HEH}(E)}{dE} dE \quad (2.1)$$

The fluence $\left[\frac{\text{particles}}{\text{cm}^2}\right]$ is obtained integrating the flux over the time:

$$\Phi_{HEH} = \int_{t_0}^{t_1} \int_{20\text{MeV}}^{\infty} \frac{d\varphi_{HEH}(E)}{dE} dE dt = \int_{t_0}^{t_1} \varphi_{HEH} dt \quad (2.2)$$

The previous fluence is responsible to induce both SEU and SEL on an electronic memory but regarding the former they are caused not only from the HEH but also from

the intermediate energy neutrons below 20 MeV and until 0.2 MeV. Since this range of energy corresponds to a fall-off on the neutron cross section, a weighted function is required to fit the experimental data: a Weibull function is the appropriate weight for the neutron flux. Together, HEH with the intermediate energy neutron contributions compose what is called High-Energy Hadron equivalent flux, defined as follows:

$$\varphi_{HEHeq} = \int_{0.2MeV}^{20MeV} \frac{d\varphi_n(E)}{dE} \cdot \sigma(E) dE + \int_{20MeV}^{\infty} \frac{d\varphi_{HEH}(E)}{dE} dE \quad (2.3)$$

and the respective HEH equivalent fluence:

$$\begin{aligned} \Phi_{HEHeq} &= \int_{t_0}^{t_1} \left(\int_{0.2MeV}^{20MeV} \frac{d\varphi_n(E)}{dE} \cdot \sigma(E) dE + \int_{20MeV}^{\infty} \frac{d\varphi_{HEH}(E)}{dE} dE \right) dt = \\ &= \int_{t_0}^{t_1} \varphi_{HEHeq} dt \end{aligned} \quad (2.4)$$

Where the general Weibull fit expression is:

$$\sigma(E) = \sigma_{sat} \cdot \left(1 - e^{-\left(\frac{E-E_{th}}{W}\right)^S} \right) = \sigma_{sat} \cdot w(E) \quad (2.5)$$

As described in [22] the Weibull parameters are retrieved from the Toshiba, a 4 Mbit SRAM memory (technology of $0.4\mu m$ and date code TC554001AF-70L) installed on the RadMon, an electronic Radiation Monitor as will be further detailed later. The fit parameters for the RadMon can be found in Table 2.1 where the experimental data are based on PTB neutron source, for energies below 20 MeV, respectively of 5, 8, 14.8 MeV, and PSI proton beam for these above 20 MeV.

Table 2.1: Weibull fit parameters for the Toshiba memory response.

Parameter	Description	Value
E_{th}	Energy threshold	0.2 MeV
W	Shape	9.25
S	Shape	3.02

The reason why the intermediate energy neutrons are not considered for SEL response is because they are negligible compared to the HEH; their fit function would be liable to give to the effect rate a overall weight close to zero. E_{th} of 0.2 MeV is the lower energy threshold capable of producing a reaction $n - \alpha$, namely when a neutron generates an α particle and the latter induces the SEU. In fact the neutron has not charge to induce upsets, but when they clash against a nucleus and the fission nuclear reaction occurs, they can produce, either a proton but we assume that it has not enough charge for inducing

SEUs, or an α particle, much more energetic and efficient to causes the soft event. The energy of 0.2 MeV is the lower energy value among those of all the typical material used in the physical memory composition and it corresponds to that of the nitrogen.

2.1.2 Thermal neutrons

Thermal neutrons are the third considered SEU source on an electronic device due to their interaction with the boron 10 as illustrated in Figure 2.2 and in [1].

R.C. Baumann, E.B. Smith / Microelectronics Reliability 41 (2001) 211–218

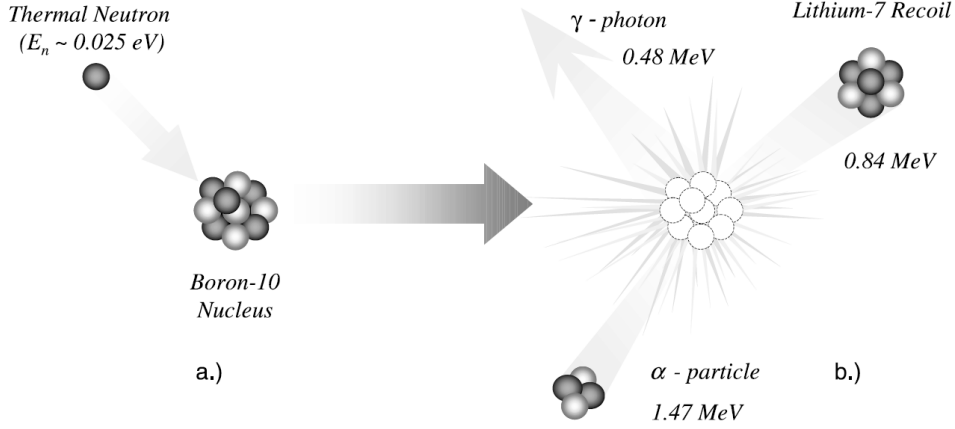


Figure 2.2: a) ^{10}B nuclear fission with a thermal neutron, b) reaction products: photon, ^7Li and the α particle that will induce the SEU.

The thermal neutron fluence is computed weighting the neutron flux with the inverse of the square root of the energy, this leads the first decreasing curve of Figure 2.1. As it can be inferred this definition includes not only the 0.025 eV neutrons but a wider spectrum, in a similar way to the Φ_{HEHeq} and for this reason there is not a Φ_{thNeq} .

$$\varphi_{thN} = \int_0^\infty \sigma(E) \cdot \frac{d\varphi_n(E)}{dE} dE \quad (2.6)$$

$$\Phi_{thN} = \int_{t_0}^{t_1} \int_0^\infty \sigma(E) \cdot \frac{d\varphi_n(E)}{dE} dE dt = \int_{t_0}^{t_1} \varphi_{thN} dt \quad (2.7)$$

where

$$\sigma(E) = \sigma_{thn} \cdot w(E) \quad (2.8)$$

It is to be noted that during the experimental tests the devices are subjected to the Φ_{HEHeq} (and/or Φ_{thN}) but not to the only Φ_{HEH} , the latter can be only simulated with

proper tools; the physical spectrum is composed from both HEH and intermediate energy neutron contributions, and Φ_{HEHeq} aims to describe it as well as possible.

2.1.3 R-factor

In general the factor R involves the ratio between thermal neutrons and high-energy hadrons fluences as shown in 2.9. It is a dimensionless quantity that expresses how many thermal neutrons relative to HEH are present in a specific area subject to the analysis. All the LHC locations are defined by means of this factor in order to assess whether a potential electronic component useful for the machine operation can survive in that radiation environment. The R-factor refers either to a quantity obtained from experimental data fluences measured on the studied location or from those of the simulations.

$$R = \frac{\Phi_{thN}}{\Phi_{HEH}} \quad (2.9)$$

Relation 2.9 is neither the only possible definition nor the most useful. Actually the previous one is more a theoretical quantity; since in most of the cases the mixed field is composed also from the intermediate energy neutrons, the R-factor retrieved for instance from an experimental measurement, shall enclose the HEHeq contribution. Therefore:

$$R_{eq} = \frac{\Phi_{thN}}{\Phi_{HEHeq}} \quad (2.10)$$

2.1.4 Events and cross sections

Cross section varies as a function of the energy, as well as the fluence. The number of measured SEE on an electronic memory, is therefore determined from all the single event contributions with varying of the energy as illustrated in Figure 2.1. Note the fact that in these expressions the flux is already integrated in time to obtain the fluence as a function of the energy.

$$N_{SEE} = \int_0^{+\infty} \sigma(E) \cdot \frac{d\Phi(E)}{dE} dE \quad (2.11)$$

However, it is typical to have a disposal only two cross section values, respectively thermal and HEH and it is not feasible to retrieve all the possible cross sections, energy dependent. Therefore the previous formula is divided taking into account these two

contributions:

$$\begin{aligned}
 N_{SEE} &= \int_0^{+\infty} \sigma(E) \cdot \Phi(E) dE = \\
 &= \int_0^{+\infty} \sigma_{thn}(E) \cdot \Phi_{thn}(E) dE + \int_0^{+\infty} \sigma_{HEH}(E) \cdot \Phi_{HEH}(E) dE = \\
 &= \sigma_{thn} \int_0^{+\infty} \Phi_{thn}(E) \cdot w_{thn}(E) dE + \sigma_{HEH} \int_0^{+\infty} \Phi_{HEH}(E) \cdot w_{HEH}(E) dE = \\
 &= \sigma_{thn} \cdot \Phi_{thn} + \sigma_{HEH} \cdot \Phi_{HEHeq}
 \end{aligned} \tag{2.12}$$

From the second to the third step, the cross sections are decomposed as $\sigma_i(E) = \sigma_i \cdot w(E)$ with σ_i constant and $w(E)$ a weighting function. The latter is the same used in the thermal neutrons definition for the left term in which it assumes the value 1 at 25 meV, whereas is not the Weibull fit of the definition as far as it is concerned the HEH. $w_{HEH}(E)$ is 1 at 200 MeV, it is formed by the Weibull function $w(E)$ between 0.2 and 20 MeV and zero elsewhere. It's this formalism which permits to have only two numeric values of cross sections although they are a function of the energy. They are often indicated in $\left[\frac{\text{particles}}{\text{cm}^2 \cdot \text{bit}} \right]$ or $\left[\frac{\text{particles}}{\text{cm}^2 \cdot \text{chip}} \right]$, dividing the cross section by the total bit number of the memory or chip respectively.

2.2 CHARM introduction

The CERN High energy AcceleRator Mixed Field (CHARM) is a new facility operating since 2014, used for testing electronic components and systems in a mixed-field radiation environment obtained using different combinations of shielding, target and test positions. It can simulate radiation fields such as that present at ground level, atmospheric - space environments and high-energy accelerator. The latter is that of our interest because we are interested in studying the sensitivity of electronic components used in systems operating in the LHC and its vicinity.

As can be seen in Figure 2.3, CHARM is placed after the IRRAD facility and the beam of 24 GeV is extracted from the Proton Synchrotron (PS).

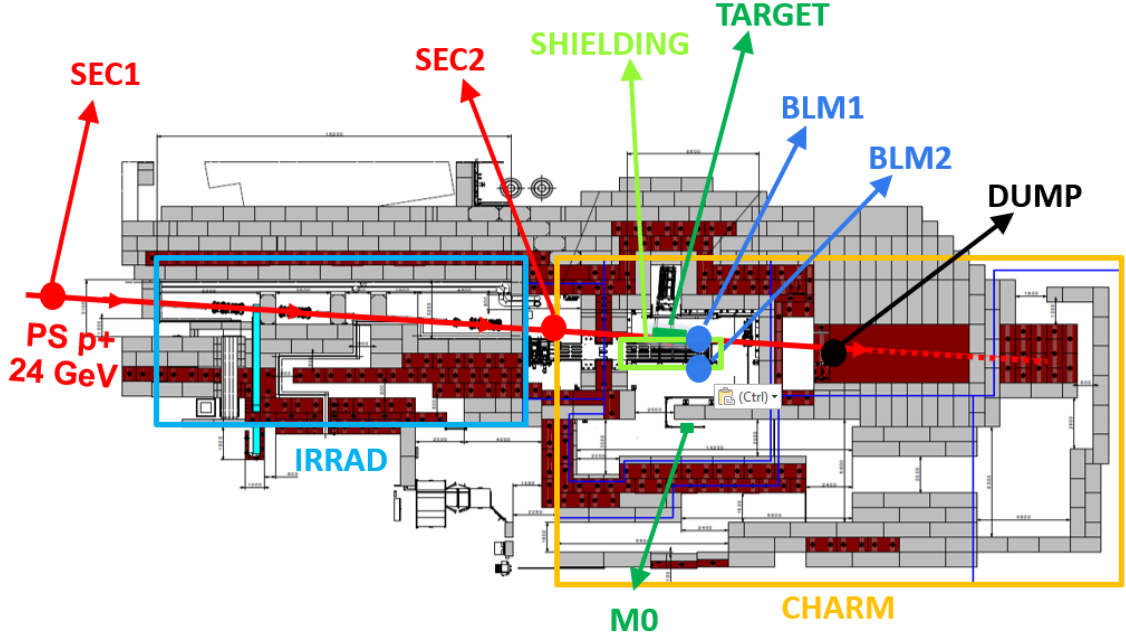


Figure 2.3: IRRAD, CHARM, SEC1 and the BLM detectors, M0 position employed in this work.

As shown in Figure 2.4 the shielding is composed of 4 different blocks respectively of concrete-iron-iron-concrete and they can be moved to obtain the required particle spectra inside the chamber. When the blocks are inside, the energy and intensity of the mixed field decreases and there is a greater contribution of neutrons, thus mimicking the conditions in the LHC alcove areas. The 24 GeV proton beam coming from PS impacts against a target, usually of copper, and the mixed field is produced from this interaction. In picture all the shielding blocks are in position so that the HEH intensity is lower. The notation $XX - abcd$ is used to denote the shielding configuration, where XX is the metal target (Copper Cu, Aluminium Al, Aluminium hole Alh) and $abcd$ is the shielding status: C=concrete, I=iron, O=out. For instance, the most common configuration employed during the period reported in this thesis was $CuOOOO$, i.e. copper target with no shielding.

Configuration: Cu0000

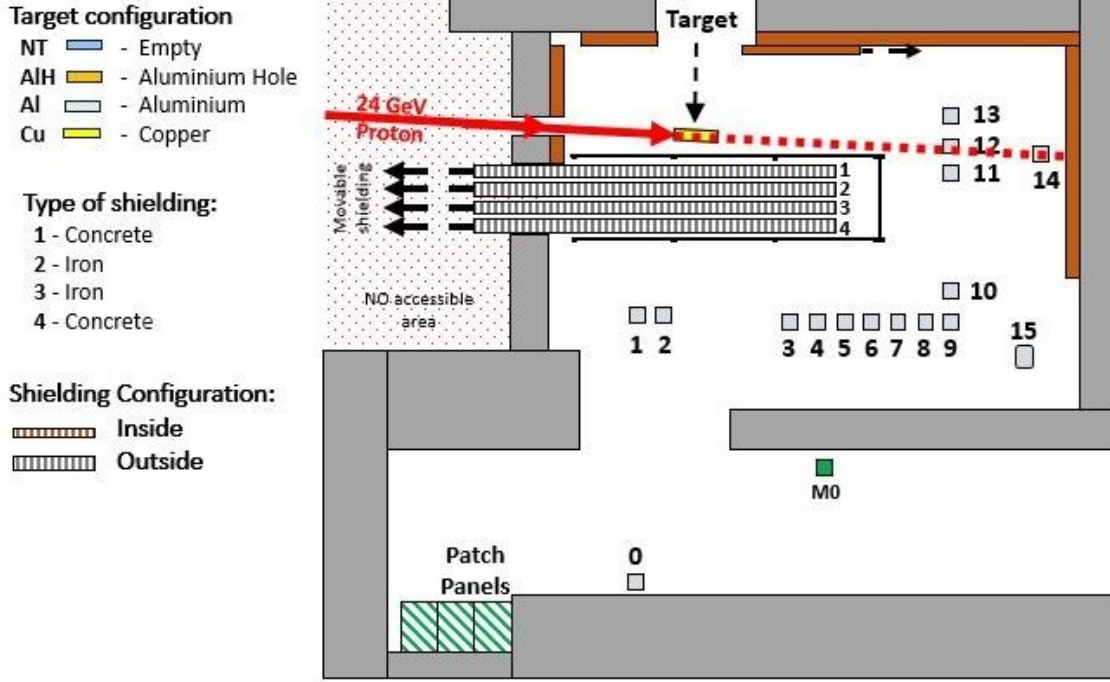


Figure 2.4: CHARM facility with the numbered positions inside the main chamber; M0 and G0 (0) in the corridor were the locations neutron-dominated used in the experiments.

There are many possible positions at CHARM for the testing of devices (see Figure 2.4), most of them inside the ionization chamber and in order to carry equipment there, an Automatic Guided Vehicle is used. Some available locations are present in the corridor also, and one of them is the M0 position that has been characterized in a first stage of this work in order to test electronic memories, basically for two reasons:

- The high relative thermal neutron flux presence (high R-factor).
- It has direct accessibility from the corridor (the main room is not easily reachable due to Radiation Protection constraints).

Accesses at CHARM during its operation period take place on the morning of every Wednesday. Normally, the beam is turned off two days before the access to wait that the radiation levels are lowered and then turned on the Wednesday afternoon. Experiments were performed from September to November 2016 and from mid-May to mid-June

Table 2.2: SEC1 calibration with aluminium foils.

Variable	Calibration Factor	Stdev	Relative Stdv
SEC1	1.84E7	0.096E7	5.22%

2017 due to the LHC and injector shut-down and therefore of all the accelerators chain, including the PS and the operation at CHARM.

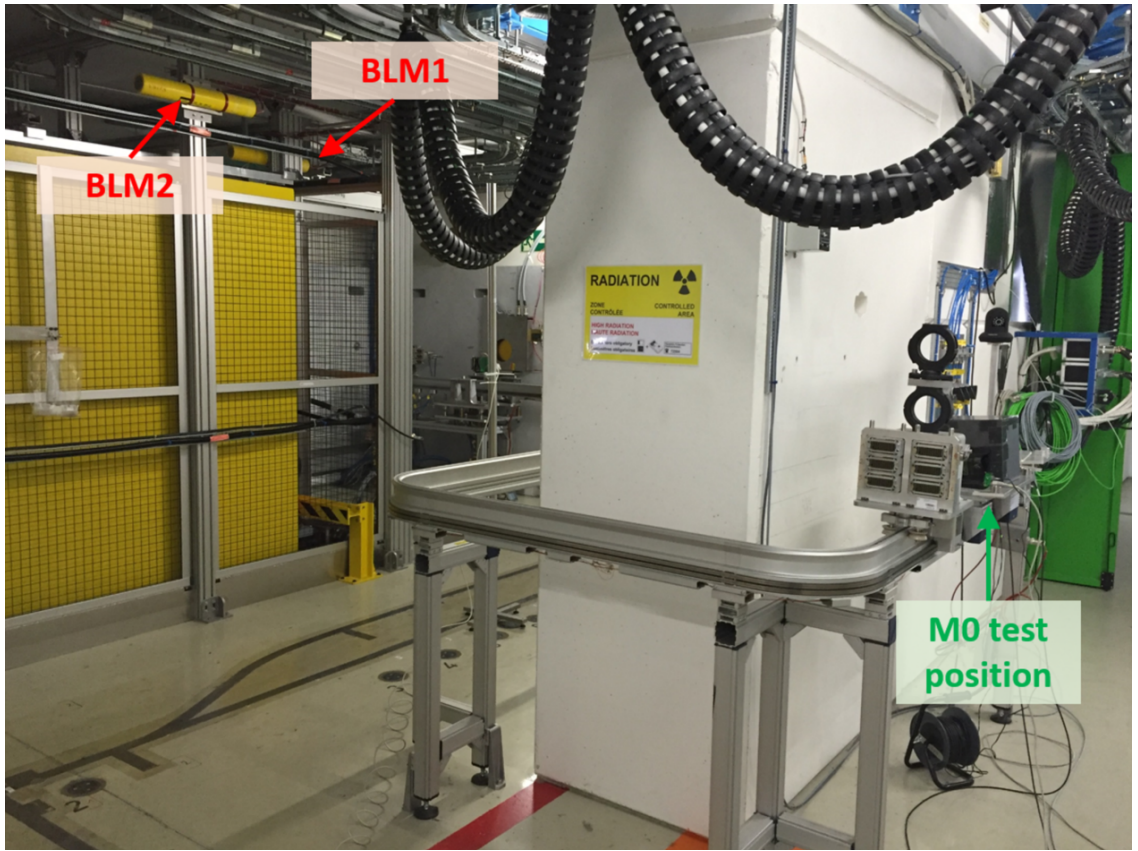


Figure 2.5: To the right: the corridor with M0 position. To the left: the main chamber with the shielding in place and the two BLMs.

An important variable is the calibrated signal from the secondary emission counter SEC1 from which the number of proton on target (POT) is retrieved multiplying the SEC1 value by 1.84E7 [3].

This calibration value was obtained using aluminum activation measurements foils placed directly in the IRRAD beam [20].

Secondary Emission Chamber detector

The Secondary Emission Chamber is a vacuum chamber composed by thin aluminium foils used as collector (anode) and source (cathode) of electrons, as shown in Figure 2.6. When the beam crosses the cathode foil, electrons are produced due to its interaction with the aluminium atoms. The electrons with enough energy to escape the metal surface, rejected from the high negative voltage applied on the cathode, travel through the vacuum gap and are collected on the grounded anode. This charge is then read out with a current-to-frequency converter that, with a comparator provides the count value. The advantage of using the SEC is that it can operate to higher intensity compared with that of the ionisation chamber that would saturate with the PS beam intensity.

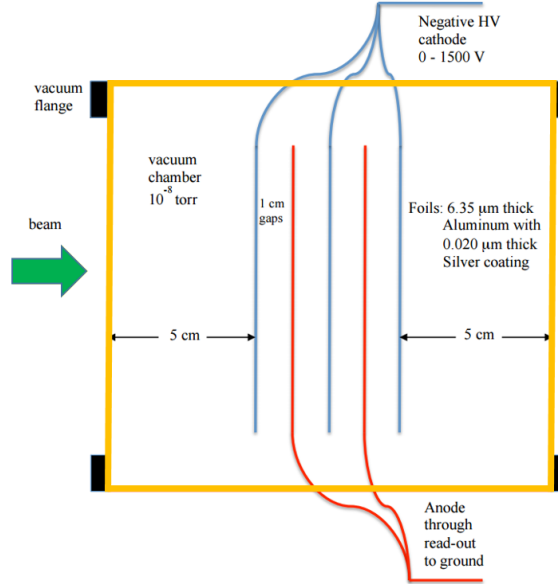


Figure 2.6: SEC

Since the beam entering at CHARM passes through the previous facility IRRAD, the beam characteristics could be affected from its operation. This is an important aspect to take into account for the analysis and will be evaluate in 2.3.3. In addition for the monitoring of the primary beam intensity, the secondary radiation field in CHARM is measured through ionization chambers (BLMs) and COTS-based detectors (the LHC RadMon system).

2.2.1 TIMBER software

Raw data from the CHARM detectors (and more in general, from all the experiments) such as SEC1 counts, BLMs, Radmon SEU, are available in TIMBER, acronym of Timeseries

Information Mastering: Browsing, Extraction and Rendering (Figure 2.7). The variables selected for the subsequent analysis are listed and outlined in Table 2.3.

Variable name	Description
MSC01.ZT8.107:COUNTS	Counts numbers from the SEC1
BLMEI.00PS.B0R10_CHARM:LOSS_RS08	BLM1 raw data
BLMEI.00PS.B0R20_CHARM:LOSS_RS08	BLM2 raw data
SIMA.CHARMB7:SEU_B1_COUNTS_INT	Total Cypress SEU number recorded from the RadMon n7*
SIMA.CHARMB7:SEU_B2_COUNTS_INT	Total Toshiba SEU number recorded from the RadMon n7*
SIMA.CHARMB1:SEUS_7	Single SEU number recorded from the RadMon n7* on one memory chip. The number after CHARMB selects the memory: Cypress (1,2,3,4), Toshiba (5,6,7,8)

Table 2.3: Main TIMBER variables retrieved for the data analysis. *RadMon can be selected changing the number in the variable.

The variables can be either plotted in a chart directly on the Query-Output window or saved in an excel file, choosing the time interval in which extract the values. The data can be retrieved just as they were recorder by the respective detectors (no options) or by applying a time-scale every fixed period time and implementing an operation of sum or average¹ over that window. In the following tables the schedule time is reported in weeks with the notation *Week – number* where it corresponds to the elapsed weeks since the beginning of the year, the latter specified on table caption. As CHARM operation take place from Wednesday to Wednesday, the week number refers to the starting week of the irradiation. The time convention of the date was UTC then when compared with local time $UTC_{time} = LOCAL_{time} - 2$ hours in Geneva (Summer time).

¹TIMBER has many more options, the brief description here exposed concerns the parameters selected for this analysis.

2.3. BLM signal analysis and operational use

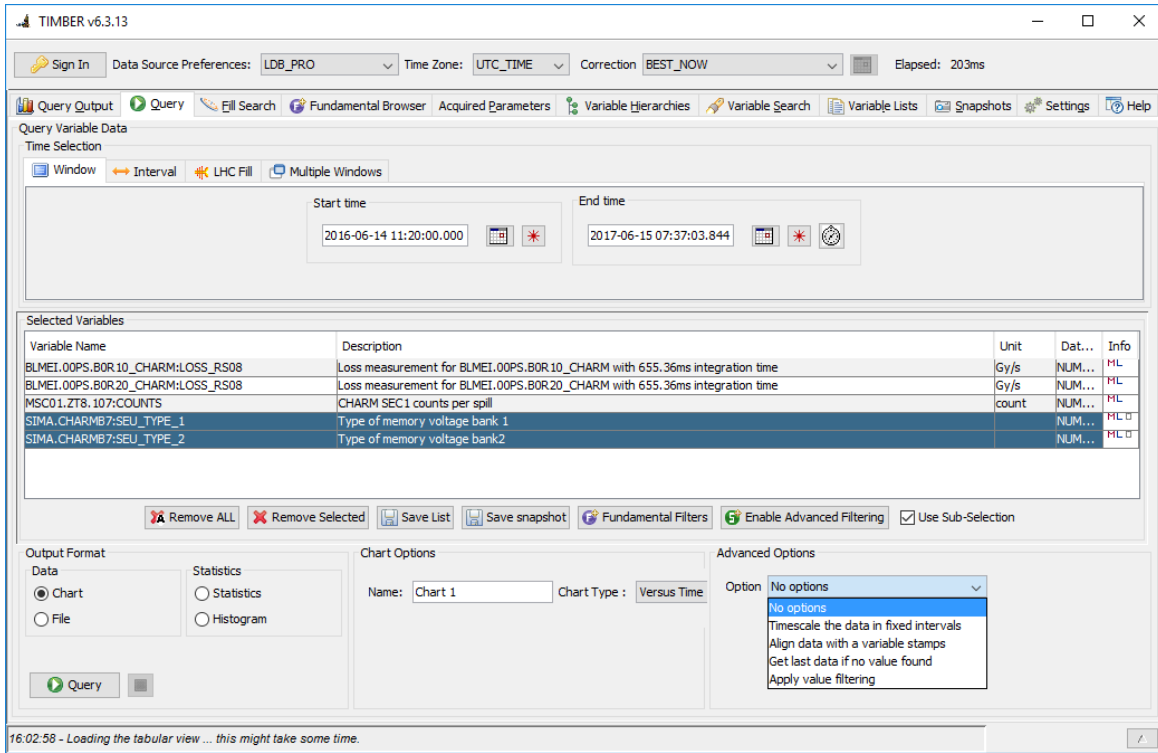


Figure 2.7: Timber software to retrieve the raw data from the experiments.

2.3 BLM signal analysis and operational use

2.3.1 Beam Loss Monitor detector

The Beam Loss Monitor (BLM) is a radiation detector incorporating an ionisation chamber. It consist in two metallic electrodes and a gap between them filled up with a gas, normally argon, air or xenon. The gas defines the sensitive volume of the chamber because when the beam passes through this, it ionizes the gas molecules producing electron-ions pairs which can move under the influence of the electric field applied between anode and cathode. Electrons are collected in the anode and this small amount of charge is measured by an electronic circuit which provides the output signal.

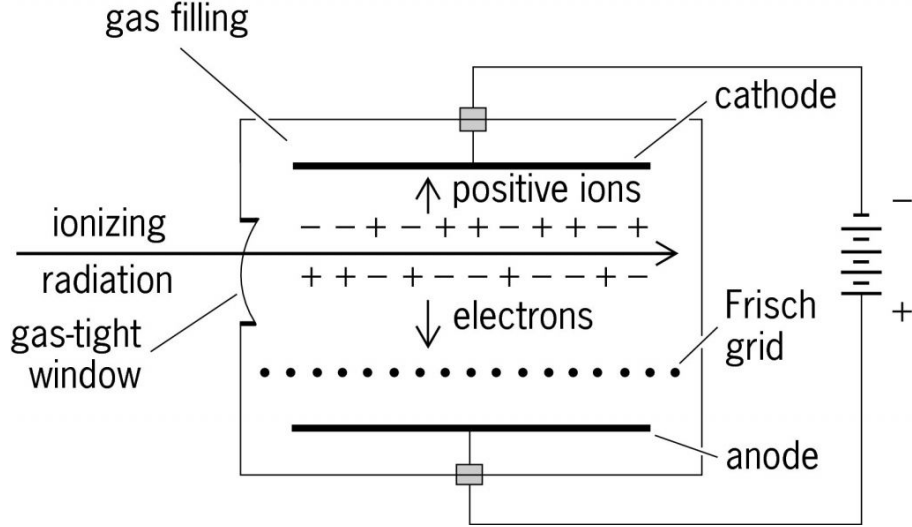


Figure 2.8: Working principle of the ionization chamber.

They are widely used along the LHC tunnel for measuring beam losses in order to intervene before that serious damages can occur on the machine parts surrounding the beam pipe. As previously shown in Figure 2.5, two BLMs are installed at the CHARM facility with the purpose of monitoring the radiation dose. According to [5] they have a relative error of 5% relative to the furnished signal that can be read-out through the TIMBER software (2.2.1).

2.3.2 BLM Analysis

The purpose of this analysis is to find a constant and reliable value which represents the target status inside CHARM, i.e. its presence and configuration since they directly affects the produced mixed-field spectra and therefore the fluence of particles investing the devices to test. This status was known from some TIMBER variables but the time intervals do not fully cover the operation period and they are not very user-friendly. Moreover as mentioned before, it would be interesting to investigate for what concern the IRRAD impact on the beam entering at CHARM and see whether this knowledge may be retrieved from the BLM signals. The data for this analysis were extracted from W25 to W45 (June, November) during 2016 and from W19 to W24 (mid-May, mid-June) in 2017 where the first week was part of the commissioning period in which beam and positions are calibrated by changing shielding configuration and target.

As first step let's look into the spill-BLM correlations. From the Secondary Emission Chamber (SEC1) that measures the beam intensity and by multiplying its count value by $1.84 \cdot 10^7$ the number of protons reaching the target (POT) have been obtained. We

can observe the raw data extracted from TIMBER in Table 2.4 referred to a window of 50 seconds during W36.

TimeStamps	BLMEI.00PS.B0...	BLMEI.00P...	MSC01.ZT8.107:COUNTS
2016-09-07 15:37:48.700	4.253E-7	3.093E-7	16164.0
2016-09-07 15:37:51.100	1.571929E-4	6.46271E-5	
2016-09-07 15:37:52.300	4.971E-7	2.872E-7	
2016-09-07 15:37:53.500	4.64E-7	3.259E-7	16284.0
2016-09-07 15:37:55.900	1.589495E-4	6.53231E-5	
2016-09-07 15:37:57.100	5.082E-7	3.093E-7	
2016-09-07 15:37:58.300	4.75E-7	3.204E-7	15831.0
2016-09-07 15:38:00.700	1.546741E-4	6.34837E-5	
2016-09-07 15:38:01.900	5.027E-7	2.983E-7	
2016-09-07 15:38:05.500	5.137E-7	3.369E-7	
2016-09-07 15:38:09.100	4.75E-7	3.204E-7	
2016-09-07 15:38:10.300	4.64E-7	2.928E-7	
2016-09-07 15:38:12.700	4.529E-7	2.928E-7	
2016-09-07 15:38:13.900	4.308E-7	2.928E-7	
2016-09-07 15:38:15.100	5.303E-7	2.872E-7	
2016-09-07 15:38:18.700	4.971E-7	3.148E-7	
2016-09-07 15:38:19.900	4.474E-7	2.872E-7	
2016-09-07 15:38:21.100	4.64E-7	3.038E-7	
2016-09-07 15:38:22.300	4.916E-7	2.928E-7	
2016-09-07 15:38:25.900	4.861E-7	3.148E-7	
2016-09-07 15:38:29.500	4.474E-7	3.148E-7	
2016-09-07 15:38:30.700	4.529E-7	2.817E-7	
2016-09-07 15:38:31.900	4.861E-7	2.762E-7	
2016-09-07 15:38:34.300	5.027E-7	2.817E-7	
2016-09-07 15:38:35.500	4.861E-7	3.093E-7	16554.0
2016-09-07 15:38:37.900	1.603635E-4	6.56269E-5	

Table 2.4: Raw data from TIMBER during a time slot in W36 with Cu-O000: BLM1 (red) BLM2 (blue), count value from the sec1 (green).

The beam structure is in spill, (see Figure 2.9) each of which has a length of 350 ms and typically they arrive at CHARM in groups of 3 spills at once where three are very close in time, spaced from 4 to 6 seconds. This cycle is repeated about every 40-50 seconds and arranged in a super-cycle of 30 bunches in order to reproduce as well as it can, a natural space radiation scenery. It is to be noted the fact that when one spill is measured from the count1, it is recognized from the BLMs with a delay of 2-3 seconds and not at the same arrival time. As highlighted in green in Figure 2.4, the first spill for instance, arrives at 15:37:48 but it's detected from the BLM1 and BLM2 at 15:37:51, hence 2.4 seconds later considering also the milliseconds. This aspect has an important consequence on the subsequent analysis when the needed of relating the BLMs and SEC1 values is relevant. For instance, it is crucial in the event that some SEC1 values need to be ruled out from the analysis relying on the BLMs signal. Since the latter is very low

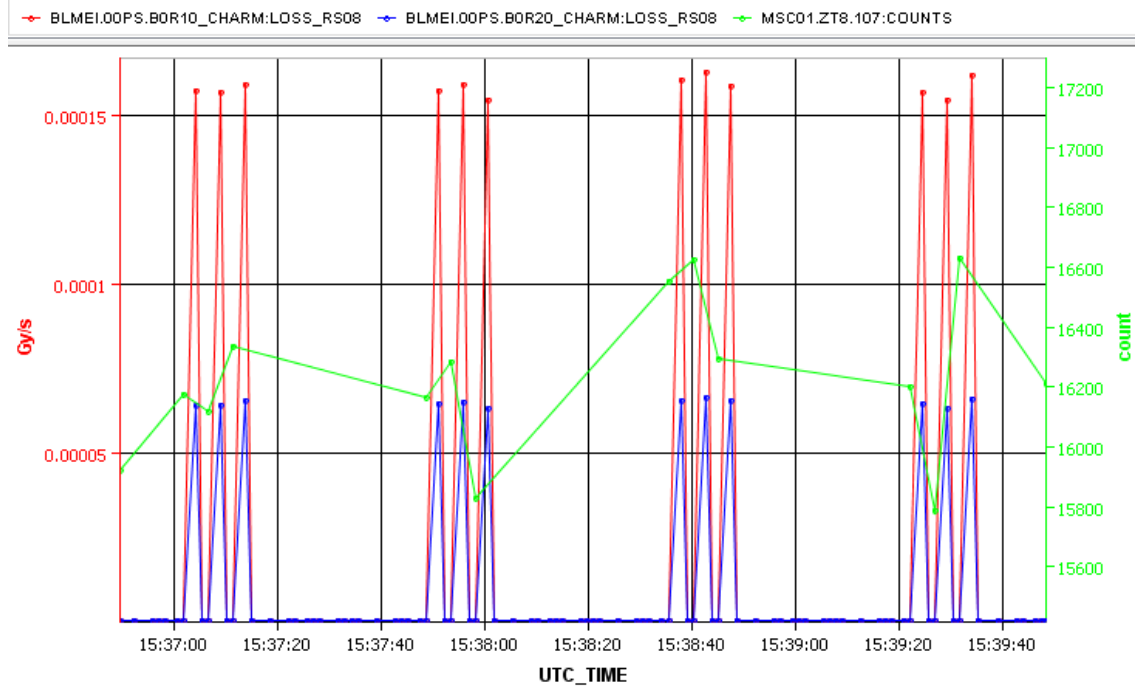
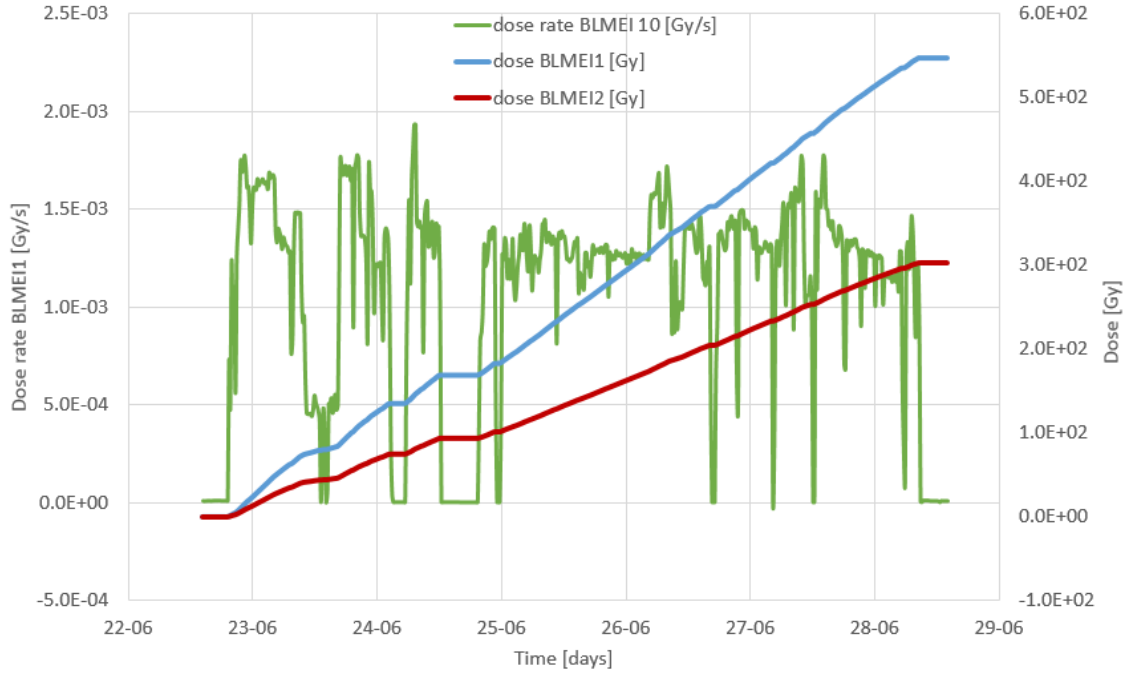


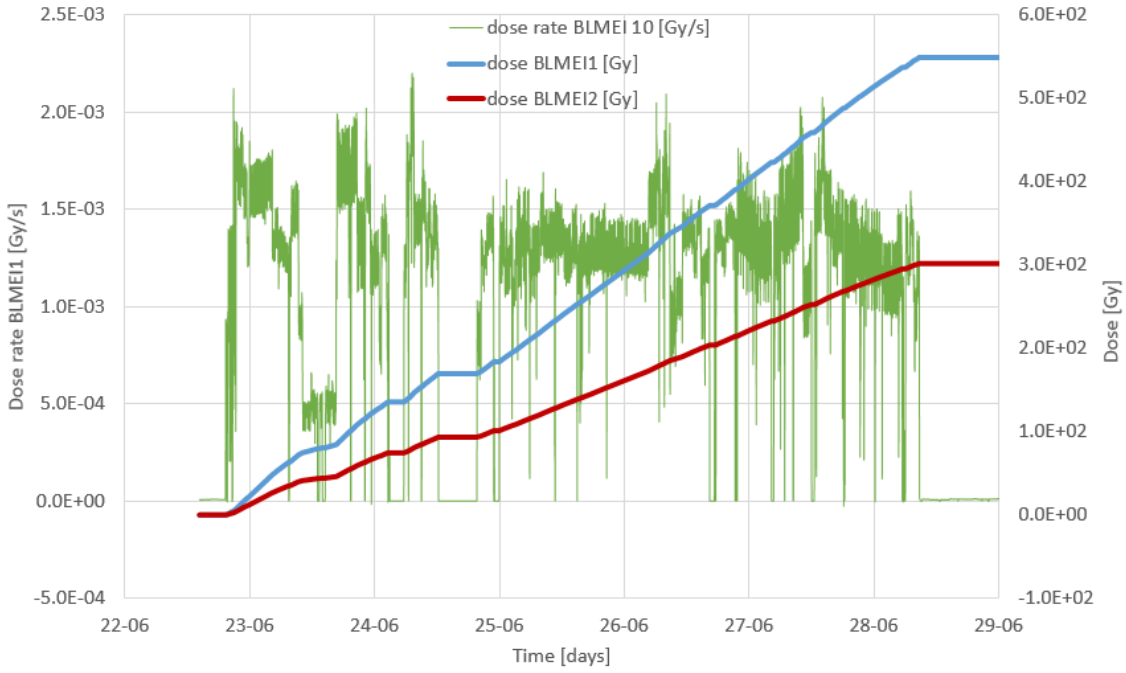
Figure 2.9: BLM1 (red), BLM2 (blue) signals and spill counter from the SEC1. The second group of three bounces is related to those of Table 2.4.

compared with that is measured with the spill presence, as they are recorded in different times, one would exclude the spill for the POT in the hypothesis that the BLM values are considered as condition to know the position of the target. For this reason and for the following two aspects the TIMBER data are retrieved every 15 minutes:

1. In one week of CHARM operation there are about 600 data with the above timescale, acceptable for analysis. With no timescale there would be about 30000 data harder to manage due to heavy files and time consumption.
2. With 15 min time window the periods are long enough so that the statistical fluctuations are small (see Figure 2.10), but short enough so that differences (as when the target is moved) as a function of time can be observed. It's clear looking at the dose rate from the graph, that extracting the data every 2 minutes, many fluctuations on the BLM signal are produced because the data are too many to display and the statistical error is higher: in this period of time there are only about 6 BLM values, instead in 15 minutes there are around 45 BLM points. However during the commissioning period in spring 2017 and for some analysis regarding the ESA SEU Monitor board (evaluated in a dedicated chapter) 3 minutes time-scale were considered.



(a) *BLM values extracted every 15 minutes intervals.*



(b) *BLM values extracted every 2 minutes intervals.*

Figure 2.10: BLM plots with data extracted every 15 minutes (top) and every 2 minutes (bottom) in W25. The *doserate* is the value every 15 min retrieved from TIMBER and *dose* is the time integrated dose rate.

Table 2.5 reports the summarized results from the detailed analysis that can be found in 6. The standard deviation and relative percentage between different week's runs is calculated for the most common configurations: Copper target with full shielding and without it. The other configurations regard the data retrieved during the calibration campaign 2017 and no statistic is available because of the single run. Nevertheless these runs rely on a very short irradiation time (few hours) as opposed to the two main configurations with a period time of about five days.

The ratio between the BLM dose and the respective POT is also called K_{BLM} -factor:

$$K_{BLM} \left[\frac{Gy}{POT} \right] = \frac{BLMdose}{POT} \quad (2.13)$$

Table 2.5: Summarizing table of the k1/k2 ratio with different configurations and target.

Config	BLM1/BLM2			BLM1/POT [Gy/POT]			BLM2/POT [Gy/POT]		
	avg	dev	%	avg	dev	%	avg	dev	%
Cu_CIIC	29.95	0.50	1.66	$5.92 \cdot 10^{-14}$	$3.20 \cdot 10^{-15}$	5.40	$1.98 \cdot 10^{-15}$	$9.99 \cdot 10^{-17}$	5.05
Cu_OOOO	1.89	0.05	2.88	$5.27 \cdot 10^{-14}$	$3.41 \cdot 10^{-15}$	6.48	$2.78 \cdot 10^{-14}$	$1.73 \cdot 10^{-15}$	6.22
Cu_CIOO	13.82			$5.64 \cdot 10^{-14}$			$4.08 \cdot 10^{-15}$		
Cu_OOOC	2.73			$5.89 \cdot 10^{-14}$			$2.16 \cdot 10^{-14}$		
ALH_OOOO	2.91			$1.37 \cdot 10^{-14}$			$4.72 \cdot 10^{-15}$		
ALH_CIOO	25.86			$1.48 \cdot 10^{-14}$			$5.74 \cdot 10^{-16}$		
ALH_CHC	36.05			$1.49 \cdot 10^{-14}$			$4.13 \cdot 10^{-16}$		

2.3.3 Impact of material in primary beam on CHARM intensity

Whit the aim of evaluating the impact that IRRAD operation may have on the CHARM beam, during 2016 some slabs of copper were placed on the upstream IRRAD and the respective beam values were measured by the BLMs. Table 2.6 outlines the K_{BLM} factors for the normal run without slabs, and with those in which a slab of 6, 3 or 1,5 cm was placed in IRRAD. The configuration was with no shielding and the percentage concerns the difference on the K-factor of a specific thickness slab with respect to the normal run.

Finally, a comparison between the nominal BLMs/POT signal with the relative standard deviation from the 2016-2017 analysis of Table 2.5 and that outlined with the slabs is shown in graph 2.11, for the two standard configurations. In green are highlighted the various K_{BLMs} factors during the normal CHARM operation with CU-OOOO, namely when the beam is not affected from IRRAD and those with distinct copper slabs in thickness. In yellow the mean BLM/POT for the copper with no shielding and respective standard deviation that considers the dispersion in the value of all the runs with respect to the mean. The latter is displayed with 1σ , thus covering 68% if the statistic relies

Table 2.6: BLMs/POT values when a slab of different thickness were inserted in the upstream IRRAD facility to find out the impact on the beam at CHARM.

Copper slab		Config	Time [hh:mm:ss]	k_{BLM1} [Gy/POT]	%	k_{BLM2} [Gy/POT]	%
nothing		CU_OOOO	00:28:50	$5.74 \cdot 10^{-14}$		$3.07 \cdot 10^{-14}$	
6 cm	12x5mm	CU_OOOO	02:21:40	$3.82 \cdot 10^{-14}$	-33	$1.92 \cdot 10^{-14}$	-37
3 cm	6x5mm	CU_OOOO	02:41:58	$4.74 \cdot 10^{-14}$	-17	$2.44 \cdot 10^{-14}$	-20
1.5 cm	3x5mm	CU_OOOO	02:31:20	$5.23 \cdot 10^{-14}$	-9	$2.74 \cdot 10^{-14}$	-11

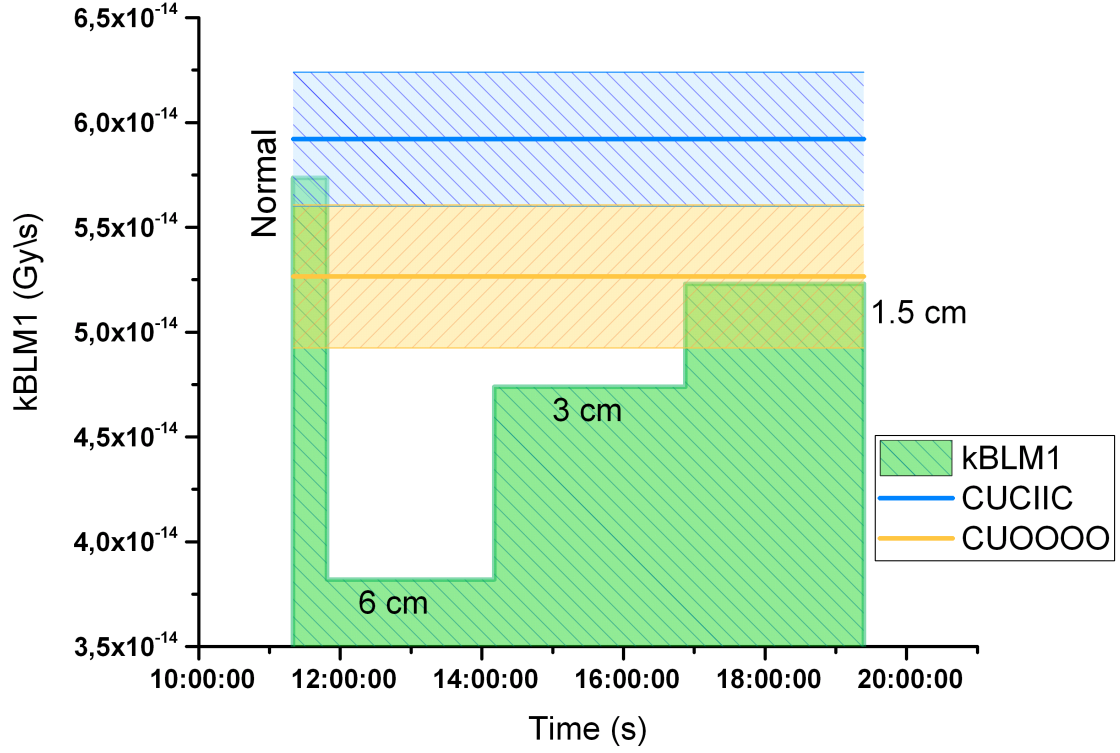
on the normal distribution (Table 2.7). Likewise the K_{BLM} is shown in blue for the full shielding configuration. The latter has only to be compared with the mean of Cu-OOOO in order to have the information of the amplitude values recorded from the same BLM but with the full shielding. Whereas for the BLM1 its signal is higher with CUCIIC, as far as it is concerned the BLM2 its output is very low with the full shielding due to its collocation behind this latter. it is clear that also considering only one standard deviation, the

Table 2.7: Standard deviation of the normal distribution.

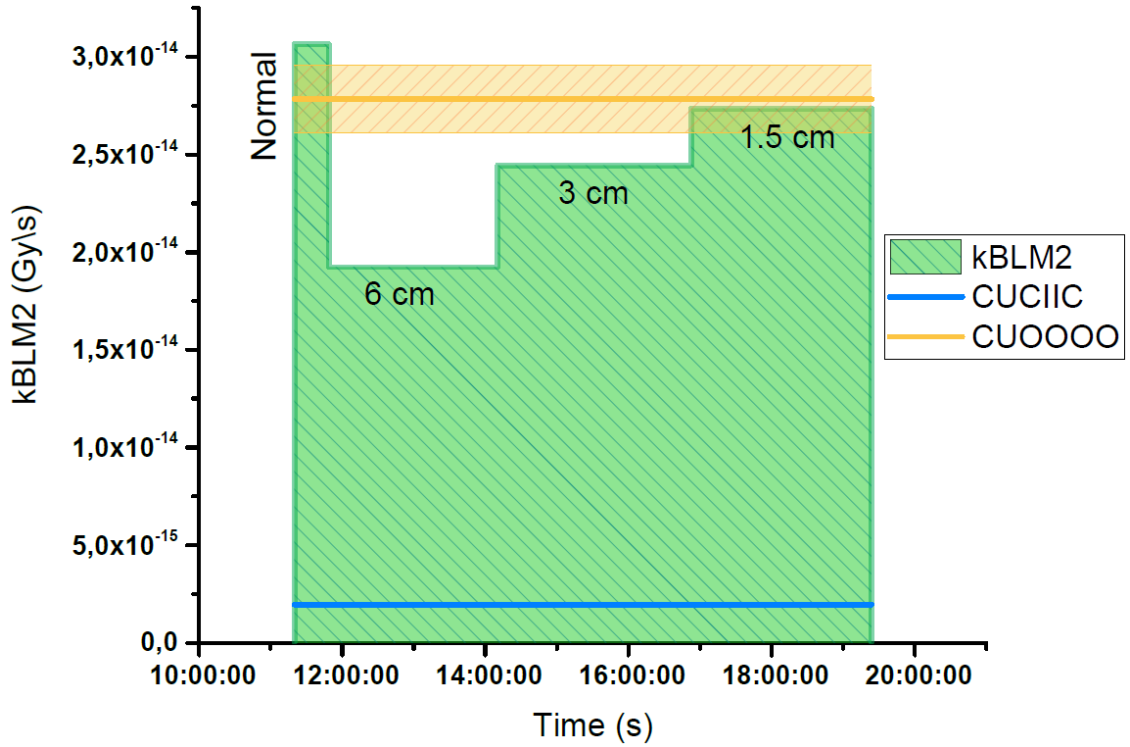
Standar deviation	Probability %
1σ	68.3
2σ	95.5
3σ	99.7

thinner slab introduced in IRRAD is not detectable from the BLMs values. In addition, whether 3σ are employed to include all possible values, only large copper thicknesses can be recognized.

In conclusion, from Table 2.5 the standard deviation of the BLM to POT is about 6% for both, therefore for reductions on the signal of more than 12% (2σ), it can be used to identify them. Considering that during the run with the slabs, the BLMs values recorded a signal above one standard deviation (normal high compared with that of the yellow line), 12% of BLM/POT variation corresponds to identify 3 cm of copper (see the percentage in Table 2.6).



(a) *BLM1/POT*.



(b) *BLM2/POT*.

Figure 2.11: BLM to POT ratio with different slab thickness. CUCIIC configuration is added only for completeness to show the difference of signal compared with that of Cu-OOOO: the BLM2 value with full shielding changes considerably due to its collocation.

2.4 Boron carbide thermal neutrons absorber and its impact on M0

The boron carbide is one of the hardest known materials composed of ceramic aggregate and for this reason it is also called *black – diamond* with chemical formula B_4C . It has many applications, from the tank armour to industrial utilizations. It's capability of absorbing neutrons without a high residual activation, make it particularly suitable for the nuclear power plants and for our interest regarding the thermal neutron absorption. In fact, it is able to remove a large fraction of the thermal neutron flux as shows in more detail through dedicated simulations. A quick idea on its good property in absorbing these particles is shown in Table 2.8 comparing its cross section with that of other common materials.

Table 2.8: Thermal neutron cross section overview for different materials. $1barn = 10^{-24}cm^2$.

Material	σ_{thn} [barn]
B4C	660
Pb	0.17
Au	99
Fe	2.56
Al	0.23

2.4.1 Boron carbide tiles

For the construction of a proper box in order to contain the electronic memories to test, two different boron carbide types were exploited: rigid tiles, and flexible B_4C one, as can be seen in pictures 2.12. The boron isotope distribution for the latter is the natural boron composition 20% ^{10}B , 80% ^{11}B . Rigid and fragile boron carbide tiles has the advantage of owning a very high content of pure boron carbide as indicate in its specifications.

Instead, the flexible material has a lower level of boron because of the glue necessary to make it flexible, but the biggest advantage is on its capacity of completely covering a surface or only a part of it by modelling the shape of the material. Again, it can be easily cut with a cutter as opposed to that in the form of tiles and it is not fragile.

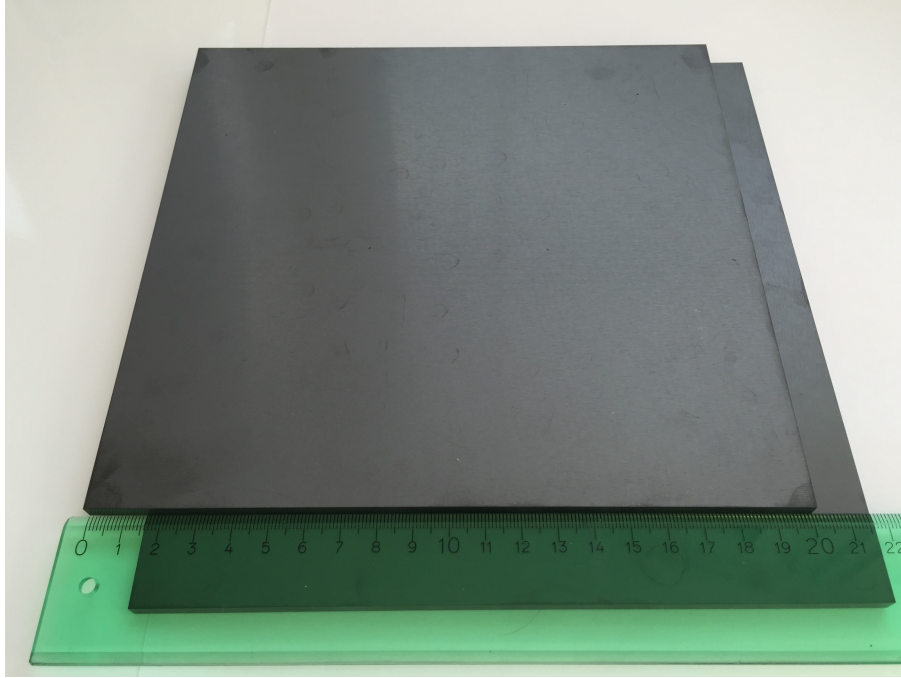


Figure 2.12: Rigid boron carbide tiles used to build the box.

	Tile	Flexible
Dimensions	200x200 mm	500x500 mm
Thickness	5 mm	5 mm
B4C content	99.5%	80%
Glue content	-	C 70%, O 25%, H 5%
Density	2.48 g/cm ³	1.36 g/cm ³
Hardness	>3300 HV	-

Table 2.9: Boron carbide specifications.

As shown in Figure 2.13, the cube was placed in M0 (see also Figure 2.5) in the corridor above a support called Montrac. The latter is a movable shuttle designed to carry small equipment inside the irradiation chamber by means of a rail but in our tests, it was always stopped in the M0 position.

To carry out the experiments three different boron carbide boxes were employed:

1. the cube-box built with 4 tiles due to non-availability of two further pieces, during 2016.
2. the complete cube-box with all the 6 tiles, during 2017.
3. the flexible cover realized according to the need of coating a specific board or system shape.

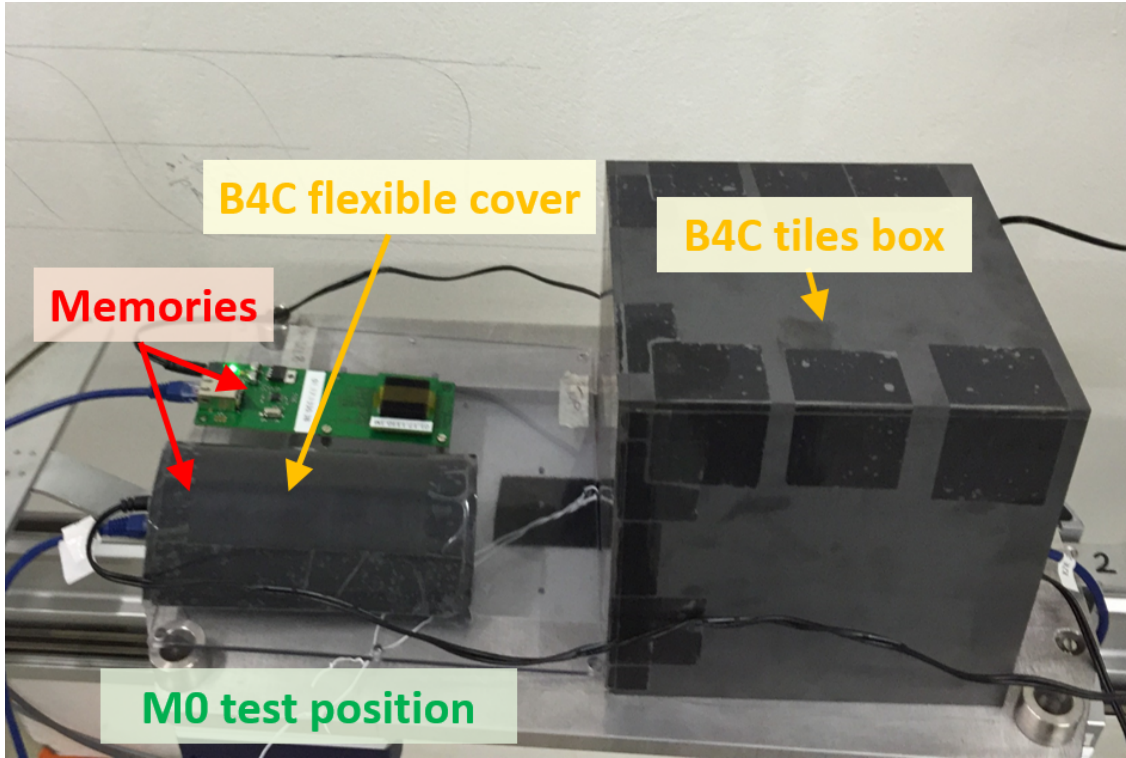


Figure 2.13: Boron carbide box and flexible cover above M0 position (Montrac base) at the CHARM facility.

Regarding the box 1., the open side of the cube was headed to the right of the previous Figure towards the exit of the corridor and the other side with no tile downward. The entire structure did not match perfectly at the base of the Montrac because of the different sizes of the two. Therefore, there was a small slit of triangular shape that allowed the passage of neutrons. However as will be exposed in the result chapter, also with only 4 tiles the thermal neutron reduction was satisfactory of a factor 4.

2.5 Radiation environment at G0 and M0

Both G0 and M0 positions are located in the corridor of CHARM. Their particles spectrum is dominated by thermal neutrons especially regarding M0 that is located behind the irradiation wall which thermalize the neutrons. However G0 is perpendicular to the main chamber entrance whereas M0 is more shielded by the wall (see Figure 2.4).

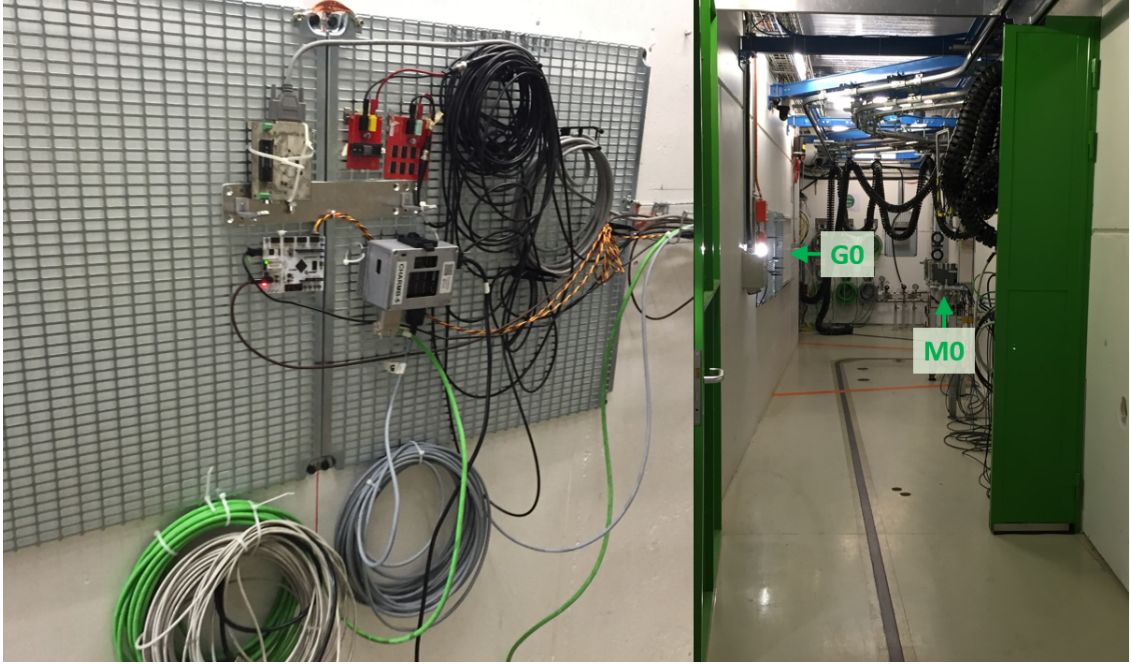


Figure 2.14: To the left the G0 position and to the right the corridor at CHARM with both positions.

Table 2.10: High-Energy Hadrons and Thermal neutrons fluxes, determined from FLUKA simulations. CuOOOO configuration.

<i>Location</i>	<i>HEH</i> [cm^{-2}/POT]	<i>HEHeq</i> [cm^{-2}/POT]	<i>Thneq</i> [cm^{-2}/POT]	<i>R</i>	<i>Req</i>
<i>1</i>	$1.99 \cdot 10^{-5}$	$3.41 \cdot 10^{-5}$	$7.13 \cdot 10^{-5}$	3.6	2.1
<i>12</i>	$2.66 \cdot 10^{-4}$	$2.74 \cdot 10^{-4}$	$8.31 \cdot 10^{-5}$	0.3	0.3
<i>M0</i>	$1.71 \cdot 10^{-6}$	$2.36 \cdot 10^{-6}$	$2.86 \cdot 10^{-5}$	16.7	12.1
<i>G0</i>	$4.70 \cdot 10^{-6}$	$7.67 \cdot 10^{-6}$	$3.53 \cdot 10^{-5}$	7.5	4.6

Table 2.10 shows the main quantities that characterize a position from FLUKA simulations ([6]). R-factor equivalent is the ratio between HEHeq and Thneq comparable with that retrieved from the measurements. It would be very imprecise using the R factor instead of that equivalent: the values, especially for M0 may differ considerably. As can be noted, the positions inside the irradiation chamber detain an R-factor rather small compared with those on the corridor in M0 and G0. Simulations has to be compared with experimental measurements in situ for a benchmark in both directions. Whereas the main locations inside the room were already calibrated, as far as it is concerned G0 and M0 only the simulations were available. As almost all the measurements regarding this work were carried out on M0, a preliminary phase of calibration has been finalized.

2.5.1 M0 calibration and RadMon system

The M0 calibration was carried out by means of the RadMon [22]. This system, is fully developed at CERN and about 400 devices are installed in the LHC for monitoring constantly the radiation levels in various areas. Indeed, most of the electronic components are COTS (Commercial On The Shelf) type and therefore they are not designed for being radiation-tolerant. Radmon system aims to measure the radiations environment, in order to understand whether a COTS component will be able of working properly in that specific area. Its working principle relies on SRAM memories with different sensitivity to radiation. It is equipped with 4x 4Mbit SRAM Toshiba TC5556001AF-70L ($0.4 \mu m$) and 4x 8Mbit Cypress CY62157EV30-LL-45ZsXI.

During 2016, from W41 to W44, the RadMon number 7 (and in addition in W44 the RadMon number 2) was installed in the M0 position, placed above the Montrac. The tests purpose was to measure the number of Cypress and Toshiba SEUs and through the different HEHeq and thN cross sections of the two memories, to retrieve the thermal neutron and HEHeq fluence and there ratio, namely the R-factor. In both RadMon 2 and 7, the Lot number was the same (see Table 2.11) so that the memories' sensitivities can be considered constant within the lot-to-lot variability.

Table 2.11: Lot number for RadMon 2 and RadMon 7 (2016).

RadMon	Cypress memory	Toshiba memory
CHARMB7	Lot. 1037	Lot. 0509
CHARMB2	Lot. 1037	Lot. 0509

Table 2.12 reports the calibrated HEH and THN cross sections for the two RadMon in $[cm^2]$ and $[cm^2/bit]$, the latter obtained multiplying the previous one by the total bit number respectively of the Cypress ($4x8Mbit = 2^{25}bit$) or Toshiba ($4x4Mbit = 2^{24}bit$). Memories were both powered up at 3V; only the Toshiba could be supplied at 5V but in this case the thN sensitivity varies.

Table 2.12: RadMon 2 and RadMon 7 cross sections.

RadMon		Cypress1037 4x8Mbit		Toshiba509 4x4Mbit	
		HEH	thn	HEH	thn
2016	3V $[cm^2/bit]$	$3.31 \cdot 10^{-13}$	$4.7 \cdot 10^{-16}$	$3.00 \cdot 10^{-14}$	$1.14 \cdot 10^{-13}$
	3V $[cm^2]$	$1.11 \cdot 10^{-5}$	$1.58 \cdot 10^{-8}$	$5.03 \cdot 10^{-7}$	$1.91 \cdot 10^{-6}$
2017	3V $[cm^2/bit]$	$3.31 \cdot 10^{-13}$	$4.70 \cdot 10^{-16}$	$5.35 \cdot 10^{-14}$	$1.84 \cdot 10^{-13}$
	3V $[cm^2]$	$1.11 \cdot 10^{-5}$	$1.58 \cdot 10^{-8}$	$8.98 \cdot 10^{-7}$	$3.09 \cdot 10^{-6}$

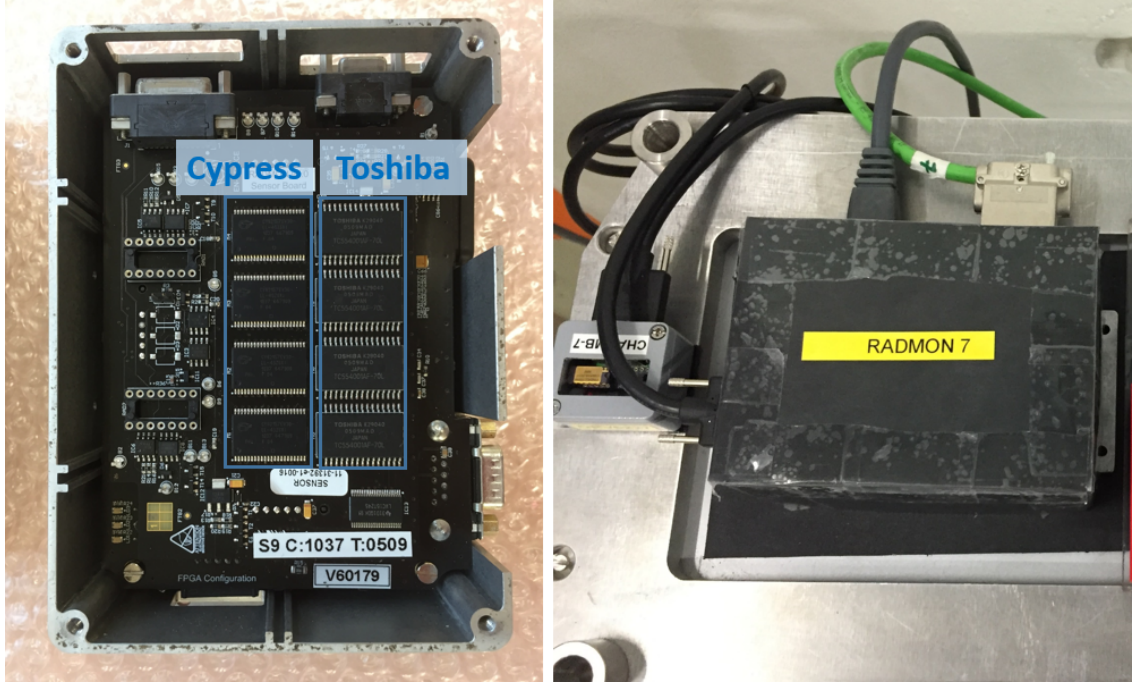


Figure 2.15: Toshiba and Cypress memories on the RadMon.

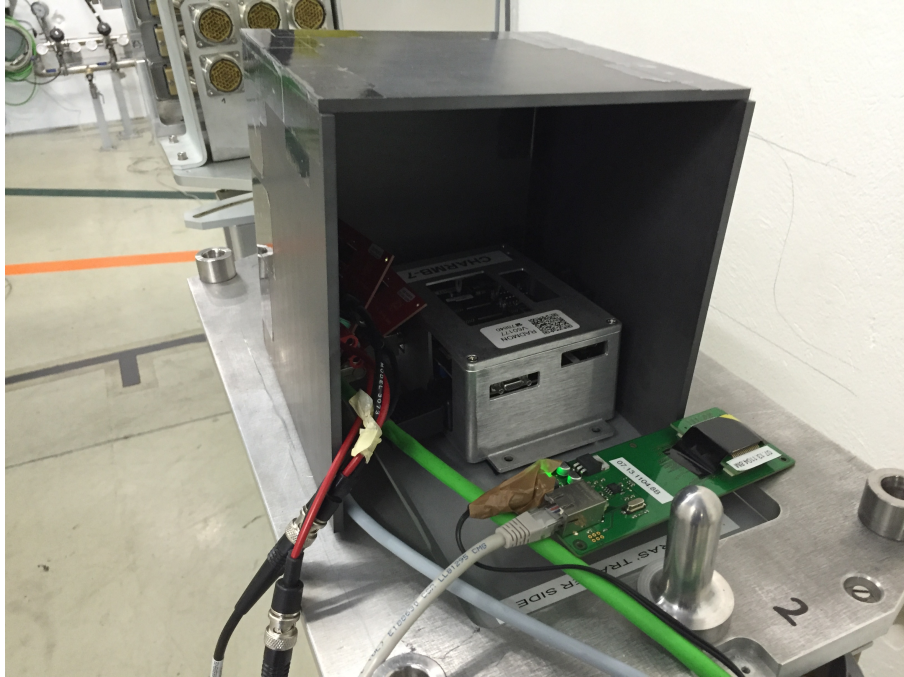


Figure 2.16: RadMon 7 inside the B4C cube above the Montrac position M0.

A summary of the 4-weeks analysis for the RadMon measurements in position M0 can be found in Table 2.13. The data for all the weeks are related to the RadMon 7 except for W44 in the experiemnt without the boron carbide, where the RadMon 2 was employed in

parallel with the RadMon 7, the latter inside the B4C box but both above the Montrac.

Table 2.13: RadMon analysis, M0 position. Numbers 7 or 2 refer to the RadMon, O and C refer to CU-OOOO and CU-CIIC respectively.

week	setup	conf	Cypress SEUs	Toshiba SEUs	HEHeq [cm-2]	kHEHeq [cm-2/POT]	Tneq [cm-2]	kTneq [cm-2/POT]	Req=tneq/ HEHeq	int POT
W41	no B4C 7	O	222895	342492	1.98E+10	1.53E-06	1.74E+11	1.34E-05	8.77	1.30E+16
W42	B4C 7	O	99215	38828	8.91E+09	1.40E-06	1.80E+10	2.82E-06	2.02	6.37E+15
W43	B4C 7	O	173380	74041	1.56E+10	1.25E-06	3.46E+10	2.78E-06	2.22	1.24E+16
W44	B4C 7	C	26784	22781	2.40E+09	1.74E-07	1.13E+10	8.20E-07	4.71	1.38E+16
W44	no B4C 2	C	17390	97777	1.49E+09	1.09E-07	5.07E+10	3.69E-06	33.96	1.38E+16

- Cypress and Toshiba SEUs are the total number of SEUs recorded during the run week. These values are extracted from TIMBER, making the difference between the last counter value and the first one relative to the run-time window. Indeed there is a SEU counter that continues to increase and do not reset over the runs. Only the last row in table regards the RadMon 2, whereas all the others refer to the RadMon 7.

- HEHeq fluence [cm^{-2}] and thneq fluence are retrieved by solving the following system of two equations

$$\begin{cases} N_1 = \sigma_{HEH1} \cdot \Phi_{HEHeq} + \sigma_{thn1} \cdot \Phi_{thn} \\ N_2 = \sigma_{HEH2} \cdot \Phi_{HEHeq} + \sigma_{thn2} \cdot \Phi_{thn} \end{cases} \quad (2.14)$$

Where the subscript 1 refers to the Cypress and 2 to the Toshiba memory. The unknowns are Φ_{HEHeq} and Φ_{thn} . The cross sections coefficients are in Tab 2.12, N1 and N2 are the RadMon SEUs number from Tab 2.13.

- $KHEHeq$ and $KTnneq$ [cm^{-2}/POT] are the previous fluences normalized by the total number of POT arrived inside the CHARM irradiation chamber which impacted against the target. The POT values area retrieved from the TIMBER analysis.
- $Req = tneq/HEHeq$ is the equivalent $R - factor$, the final result.

In principle, with the boron carbide the R-factor is supposed to tend to 0 because theoretically, the thermal neutron contribution is zero, but as the cube was not completely closed, it is reasonable that they cannot be 0. Another reason for explaining this behaviour is that the higher energy neutrons (e.g. epithermal and fast) also contribute to the thermal neutron equivalent fluence and the boron carbide absorbs a certain range of the spectra as will be show performing the FLUKA simulation.

However it is clear that the use of the boron carbide reduces more than 4 times the R-factor with configuration CuOOOO and 7 times with the full shielding CUCIIC.

It is worth noting that whereas the results for the HEHeq K-factors of W41, 42 and 43 are compatible with each other (same RadMon and facility configuration, with and without boron carbide) there is a large spread between the two values (one with and one without boron carbide) recorded in W44 with the different RadMon. As the boron carbide is not expected to alter the HEHeq fluence (simulation support will be provided in future work) this different needs to be further investigated.

These results can be compared with the FLUKA simulations for the same M0 position. It is important to bear in mind the difference between HEH (hadron fluence above 20 MeV) and HEHeq (hadron fluence above 20 MeV plus weighted neutrons contribution between 0.2 and 20 MeV). Table 2.14 illustrates well this difference in the R-factor results: the first value to the left was retrieved using the HEH and in the second column by means of the HEHEeq. In the experiments we can't measure the HEH fluence but only the HEHeq, therefore all the comparisons must be made using HEHeq that takes into account also the neutron spectra between 0.2 MeV and 20 MeV.

Table 2.14: FLUKA 2016 fluences simulation for M0 position.

Config	<i>HEH</i> [cm-2/POT]	<i>HEHeq</i> [cm-2/POT]	<i>tnEq</i> [cm-2/POT]	<i>R</i>	<i>Req</i>
Cu-OOOO	$1.71 \cdot 10^{-6}$	$2.36 \cdot 10^{-6}$	$2.86 \cdot 10^{-5}$	16.7	12.1
Cu-CIIC	$2.13 \cdot 10^{-7}$	$2.69 \cdot 10^{-7}$	$1.18 \cdot 10^{-5}$	55.3	43.7

Table 2.15: Experimental 2016 data vs FLUKA simulations (F). Cu-OOOO (O) and Cu-CIIC (C) configurations. The fluences are normalized by POT (P).

Cnf	HEHeq [cm ⁻² /P]	HEHeq(F) [cm ⁻² /P]	H(F)/ H	tnEq [cm ⁻² /P]	tnEq(F) [cm ⁻² /P]	t(F)/ t	Req	Req(F) /Req
(O)	$1.53 \cdot 10^{-6}$	$2.36 \cdot 10^{-6}$	1.55	$1.34 \cdot 10^{-5}$	$2.86 \cdot 10^{-5}$	2.14	8.77	1.38
(C)	$1.09 \cdot 10^{-7}$	$2.69 \cdot 10^{-7}$	2.48	$3.69 \cdot 10^{-6}$	$1.18 \cdot 10^{-5}$	3.19	33.96	1.29

Concerning Table 2.15, the main quantities are the same of those in Table 2.13 without the B4C consideration (therefore taking into account W41 and W44). The ratio between simulated and experimental HEHeq/POT fluence, and similarly for the thermal neutrons shows that the simulation is less precise for the ThN because it overestimates them up to 3 times (with Cu-CIIC) whereas it's better for the HEHeq. This inaccuracy is due to uncertainty in material composition in the FLUKA model, especially in the concrete of the wall that divide the main chamber and the M0 position in the corridor. For this

reason the R-factor values are always higher in the simulations. Even if both HEHeq and ThN are worse estimates with Cu-CIIC configuration compared with Cu-OOOO, the R-factors ratio are almost the same because the two terms offset each other.

Noteworthy is the quite large spread between HEHeq (simulated)/HEHeq (from the RadMon) especially with the full shielding configuration. The experimental values show that measuring directly the amount of HEH, they are much lower than those simulated with FLUKA. This difference increases more with Cu-CIIC as target and it could be because of a possible impact of intermediate energy neutron response, but it could be also due to the RadMon 2 data (for Cu-CIIC in W45) if its cross sections differ from those of the RadMon 7 (used to retrieve the data with Cu-OOOO in W41).

As has been previously shown (reported in [7]) the agreement between the measured and simulated HEHeq k-factors in the internal radiation area is much more satisfactory than the one obtained here for the M0 position. A possible reason could be associated to the strong impact from intermediate energy neutrons and the fact that whereas FLUKA uses the response function of the Toshiba SRAM, the Cypress SRAM is used to derive the HEHeq fluence in this work. This point will therefore be subject of further analysis.

Table 2.16: Fluences and R-factors comparison with and without boron carbide absorber from RadMon data in M0 position, 2016.

Config	B4C setup	HEHeq [cm^{-2}/POT]		HEHeq/ HEHeq(B)	tnEq [cm^{-2}/POT]		tnEq/ tnEq(B)
		no B4C	B4C		no B4C	B4C	
Cu-OOOO	4t		$1.30 \cdot 10^{-6}$	1.17		$2.79 \cdot 10^{-6}$	4.80
	6t	$1.53 \cdot 10^{-6}$	$9.52 \cdot 10^{-7}$	1.61	$1.34 \cdot 10^{-5}$	$4.61 \cdot 10^{-7}$	29.08
	f		$7.76 \cdot 10^{-7}$	1.97		$5.16 \cdot 10^{-7}$	25.96
CUCIIC	4t	$1.09 \cdot 10^{-7}$	$1.74 \cdot 10^{-7}$	0.62	$3.69 \cdot 10^{-6}$	$8.20 \cdot 10^{-7}$	4.50

Config	Req		Req(B4C)/ Req
	no B4C	B4C	
Cu-OOOO	8.77	2.15	4.08
		0.48	18.12
		0.67	13.19
CUCIIC	33.96	4.71	7.21

Table 2.17: Boron carbide acronyms to identify the different built boxes.

Acronym	Description
4t	rigid box built with 4 tiles
6t	rigid box built with 6 tiles (completely closed)
f	flexible box (completely closed)

A view on the impact using boron carbide absorber is shown in Table 2.16, where the fluences and integrated POT were added together for equivalent configurations to finally retrieve the fluence in $[cm^{-2}/POT]$. The most important results are the ratios between quantities measured without boron carbide and with its employment. Regarding the B4C setup, it refers to the different boron carbide box from Table 2.17. For the HEHeq the ratio should be approximately equal to 1 because the boron carbide should not shield the high-energy hadrons but only the thermal neutrons, therefore variations from this value need to be attributed to lack of repeatability or detector-to-detector response spread. Instead, for the thermal neutrons the ratio of 4.5 or more, in both the configurations, proof that the thermal neutrons are effectively reduced more than 4 times using the boron carbide. As a consequence of this, also the R-factor with B4C decreases: 4 times for Cu-COOOO and 7 times regarding Cu-CHC.

Since the boron carbide has been used with the purpose of reducing the thermal neutrons as much as possible, in order of having the fluence coefficients to solve the equations system and retrieve the two cross sections ($\sigma_{thn}, \sigma_{HEHeq}$), the higher is the difference between the R-factor with B4C and without it the better, because the uncertainty of the error decreases. This topic is further explored in 3.2. Note that in this section the R-factor have been retrieved using the same equations employed to obtain the cross sections but changing the role of coefficients and unknowns. First, the position for the tests (M0) has been characterized by means of the R-factors so then new memories (such as the ESA Monitor) can be tested to retrieve HEH and ThN cross section.

Further considerations and observations on the RADMON data, can be found on appendix 6.

2.5.2 Mixed-field radiation calculation and monitoring

Beside the BLMs analysis, an evaluation concerning the effective flux to be considered as input for the cross section calculation has been elaborated. In fact, from the knowledge of the effective proton on target, the fluence on each CHARM position can be retrieved either considering the FLUKA values, always given normalized in $[cm^{-2}/POT]$, or exploring those measured from the RadMon system, outlined in 2.5.1. Tables 2.18 and 2.19 show the different configuration during 2016 and 2017.

Week 2016	Target	Time [h]	POT mean [POT/h]	POTs with target	SEC1 POTs	% POT	BLM1 dose [Gy]	BLM2 dose [Gy]
W24	Cu_OOOO	136.0	8.76E+13	1.19E+16	1.22E+16	-2.4	558.4	300.9
W25	Cu_OOOO	120.8	8.71E+13	1.05E+16	1.21E+16	-13.1	548.8	302.7
W26	Cu_CIIC	132.5	8.69E+13	1.15E+16	1.19E+16	-3.2	651.4	21.6
W27	Cu_OOOO	137.0	8.63E+13	1.18E+16	1.28E+16	-7.4	596.0	321.7
W28	Cu_OOOO	139.3	9.25E+13	1.29E+16	1.39E+16	-7.3	698.9	377.9
W29	Cu_OOOO	127.5	9.66E+13	1.23E+16	1.30E+16	-5.2	662.8	364.0
W30a	Cu_CIOO	10.0	8.58E+13	8.58E+14	1.26E+15	-31.9	48.5	3.5
W30b	Cu_OOOO	108.0	9.22E+13	9.95E+15	1.09E+16	-9.0	532.1	287.5
W31	Cu_OOOO	134.8	9.10E+13	1.23E+16	1.28E+16	-4.4	656.4	356.6
W32	Cu_CIIC	105.8	8.47E+13	8.95E+15	9.03E+15	-0.9	528.2	17.5
W33	Cu_CIIC	111.8	8.41E+13	9.40E+15	1.38E+16	-31.9	557.2	18.3
W36a	Cu_OOOO	43.0	8.13E+13	3.50E+15	3.50E+15	0.0	1.2	0.5
W36b	Cu_CIIC	67.0	7.91E+13	5.30E+15	5.30E+15	0.0	2.0	0.3
W37	Cu_OOOO	90.5	8.56E+13	7.74E+15	8.95E+15	-13.5	400.1	207.2
W38	Cu_OOOO	132.5	6.79E+13	9.00E+15	9.19E+15	-2.1	480.3	243.0
W39	Cu_OOOO	136.3	8.93E+13	1.22E+16	1.23E+16	-1.1	682.9	352.7
W40a	Cu_CIIC	19.3	6.40E+13	1.23E+15	1.26E+15	-2.6	80.0	2.6
W40b	Cu_OOOO	116.0	1.04E+14	1.21E+16	1.27E+16	-4.5	723.8	370.1
W41	Cu_OOOO	123.3	1.05E+14	1.30E+16	1.31E+16	-0.9	768.0	399.6
W42	Cu_OOOO	124.0	1.03E+14	1.28E+16	1.31E+16	-2.6	677.4	354.7
W43	Cu_OOOO	120.5	1.03E+14	1.24E+16	1.29E+16	-3.4	616.1	316.9
W44	Cu_CIIC	122.0	1.13E+14	1.38E+16	1.39E+16	-1.0	734.7	24.6
W45	Cu_OOOO	109.0	9.53E+13	1.04E+16	1.04E+16	-0.4	513.7	263.6

Table 2.18: CHARM parameters 2016.

Week 2017	Target	Time [h]	POT mean [POT/h]	POTs with target	SEC1 POTs	% POT	BLM1 dose [Gy]	BLM2 dose [Gy]
W19	Cu_CIIC	3.6	1.02E+14	3.61E+14	3.82E+14	-5.4	21.4	0.7
W19	Cu_CIIC	5.2	1.00E+14	5.16E+14	5.16E+14	0.0	29.8	1.0
W19	Cu_CIIC	7.6	1.11E+14	8.41E+14	1.53E+15	-44.8	49.0	1.7
W19	Cu_OOOC	1.5	8.72E+13	1.34E+14	1.41E+14	-5.3	7.9	2.9
W19	Cu_OOOO	2.5	8.08E+13	2.01E+14	2.01E+14	0.0	11.5	6.4
W19	ALH_OOOO	3.8	8.21E+13	3.09E+14	3.10E+14	-0.1	4.2	1.4
W19	ALH_CIOO	3.7	7.21E+13	2.54E+14	2.63E+14	-3.5	3.8	0.1
W19	ALH_CIIC	8.2	9.51E+13	7.67E+14	7.80E+14	-1.6	11.5	0.3
W20	Cu_CIIC	5.3	1.02E+14	5.38E+14	9.38E+14	-42.6	32.6	1.1
W20	Cu_CIIC	8.4	6.67E+13	5.61E+14	8.51E+14	-34.1	34.2	1.1
W21	Cu_CIOO	3.3	9.28E+13	3.06E+14	3.06E+14	0.0	11.3	0.5
W21	Cu_OOOO	89.4	9.64E+13	8.61E+15	1.03E+16	-16.2	450.9	240.6
W22	Cu_OOOO	110.5	9.03E+13	9.96E+15	1.00E+16	-0.7	507.5	267.6
W23	Cu_OOOO	82.3	1.02E+14	8.41E+15	9.36E+15	-10.2	431.7	227.5

Table 2.19: CHARM parameters 2017.

- POT mean for the week [POT/h] is calculated taking the last value of the cumulative POT (or equivalently summing all the single POT) and dividing it by the run time, namely considering only the time range at which the BLMs recognized dose. This period of time is shown in hours in the column Time.
- POT with target are the effective POT arrived inside the irradiation room at CHARM in the corresponding week, when the target was in position. The condition of beam and target was checked through the respective TIMBER variables and BLMs levels. In particular, the spill counted from the SEC1 have been filtered by means of the BLM1 value, for excluding those that did not produce radiation. This integrated POT is that employed for other calculations as in order to retrieve the radiation fluences investing the memories placed on M0.
- SEC1 POT are those directly registered by the Secondary Emission Chamber without any filter.
- %POT is the difference between the POT measured from the SEC1 with respect to the integrated POT with the target.

$$\%POT = \frac{POT_{\text{with target}}}{POT_{SEC1}} \cdot 100 \quad (2.15)$$

It is to be noted that in some week this difference can reach even more than 40%. Obviously, this percentage may vary considering a different period-time in order to extract the data from TIMBER. The adopted approach was that of setting the time windows looking at when the BLMs detectors were measuring any non-zero value. The discrepancy is mainly owing to two factors:

1. target presence. If the target is removed from the beam and inlaid in his alcove the spill do not impact on it, and the mixed filed is not produced. The BLM1 recognize a very weak signal, about 1000 times lower with respect of the normal operation.
2. IRRAD influence. The upstream facility may interfere on the beam also if it is not always detectable from the BLMs, as explained in chapter 2.3.3.

Different instead the case in which the beam is lost in some collimator or due to PS operations. IN this situation, even the SEC1 do not measure signal.

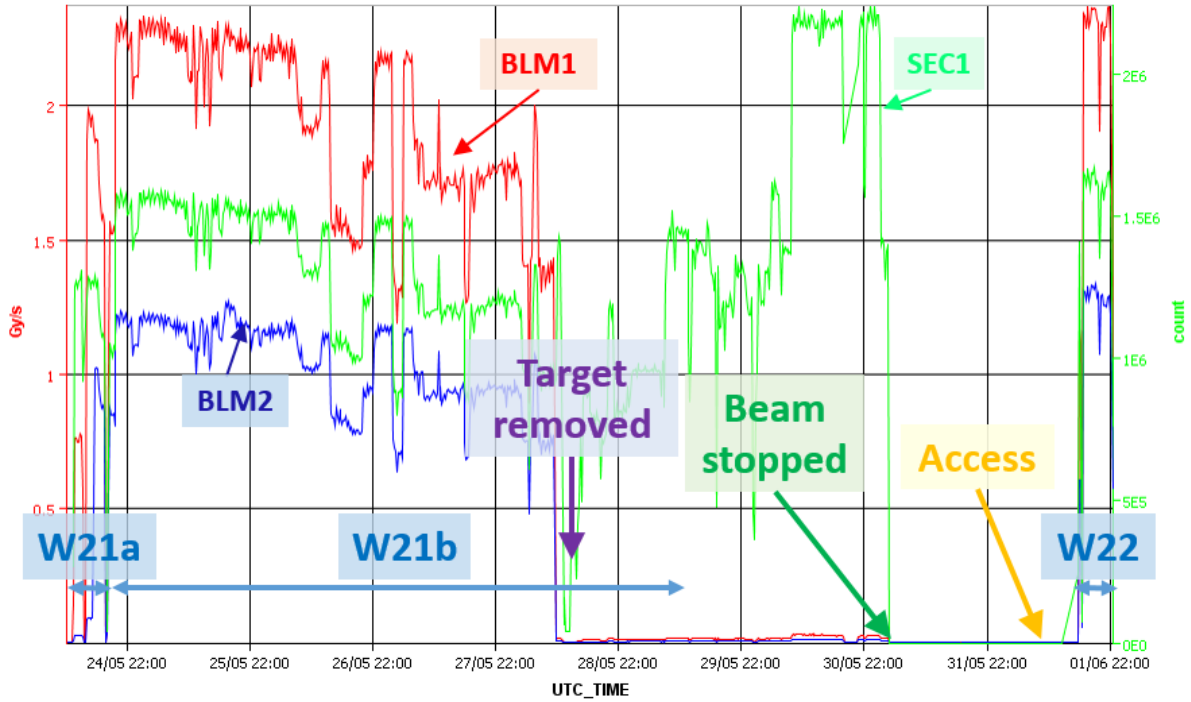


Figure 2.17: SEC1, BLM1, BLM2 values during W21 in 2017. It's quite evident that between the target removal and the beam stop, the SEC1 measured high intensity but the BLMs values recorded a signal close to zero.

A practical example to unfold this behaviour is outlined in Figure 2.17. The time period refers to W21 during 2017; W21a with CUCIOO (only few hours) and W21b with Cu-OOOO configuration. At some point the target was removed but the beam was still working and the SEC1 values were even higher than before. on this spot is clear the target

impact on the BLMs signals which showed values in proximity of zero. Only when the beam was interrupted for allowing the approaching access, the BLMs indicator dropped down to zero. Sometimes the target is simply changed, it takes about 15 minutes to complete this movement.

2.5.3 FLUKA simulations

FLUKA is a CERN developed tool for calculations of particle transport and interactions with matter [21]. It is based on the Monte Carlo method, a wide set of algorithms that through random sampling aim to find a numerical solution to a problem. FLUKA can simulate the interaction of protons, neutrons, pions, electrons, muons, photons with the matter and particularly significant for this work it can reproduce the HEH, thermal and intermediate energy neutron environments. However for the latter, FLUKA relies on the response of the Toshiba memory, the same installed on the RadMon. Several Toshiba cross section at different energies were measured, performing tests in standard facility and then implemented in FLUKA with a Weibull fit to cover the range between 0.2 and 20 MeV. It's in this way that FLUKA calculate the HEHeq fluence for instance. This aspect should be borne in mind when the cross section are retrieved confiding on the FLUKA HEHeq fluence. This approach assumes the two memories response (i.e cross section as a function of energy) being very similar within the intermediate energy neutron range. CHARM, the LHC tunnel and critical areas were designed exploring the radiation levels obtained from FLUKA simulations. One of the most important aspects for the FLUKA input is the geometry model, that has to be as accurate as possible in order to consider all the potential interactions among particles and matter. Nevertheless the number of primary particles required for the simulation is a trade-off between precision on the output result and time-consumption for the process. Being FLUKA a Monte Carlo tool, its algorithms achieve the results by thinking in terms of primary particle, which may be any kind of particle. Anyway in the CHARM context, a primary particle can be thought as a proton on target. The computational load can be split thorough many CPUs up to 120 arranged in a cluster. To give an idea, approximately one week of operation is required, to have a good statistic on the entire CHARM facility.

Focusing on M0 position, its general particle spectra was performed with more than 40 millions of primaries for both Cu-OOOO and Cu-CIIC configurations and shown in Figure 2.18a and 2.18b from [6].

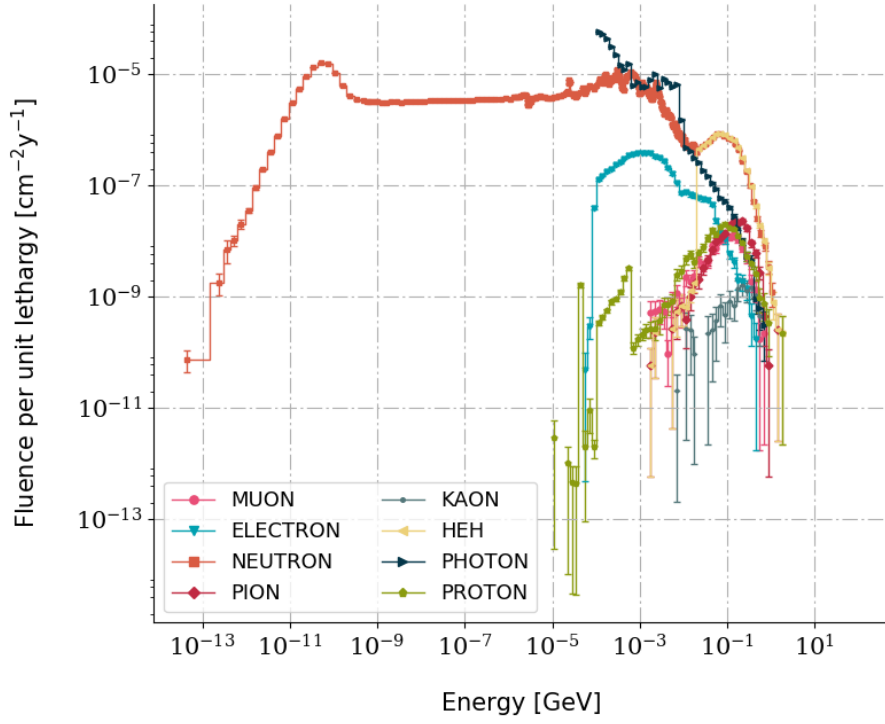
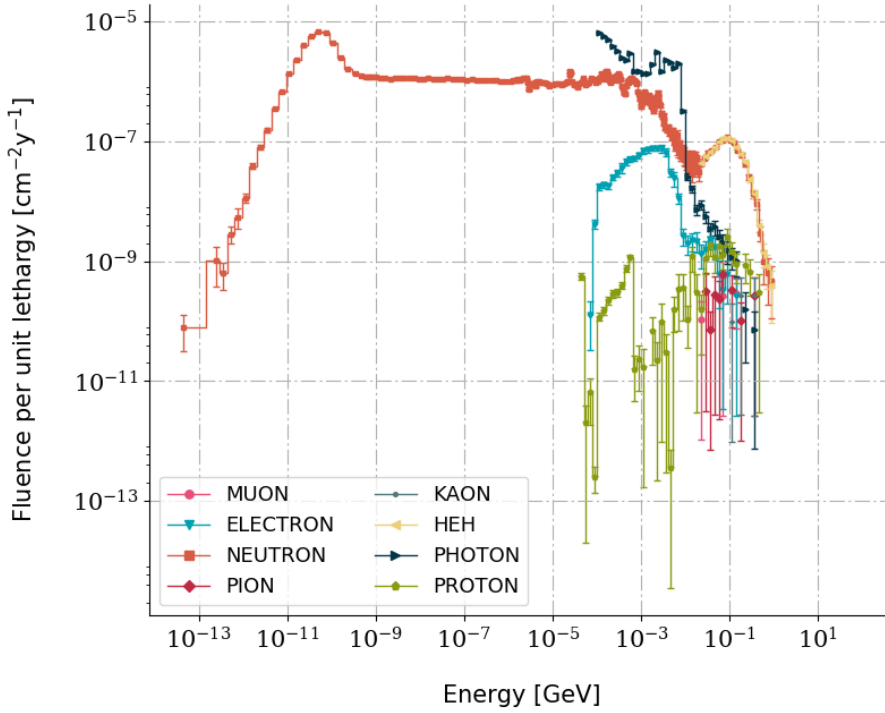
(a) *Cu-0000*.(b) *CU-CHC*.

Figure 2.18: M0 particle spectra.

These spectra are calculated considering an USRTRACK detector in FLUKA, over a sensitive volume of $20 \times 20 \times 20 \text{ cm}^3$. As can be noted the position is neutron-dominated: it is evident the thermal neutron peak around 25 meV, as well as the intermediate energy neutron contribution. Above 20 MeV The neutron trend overlaps that of the HEHeq; this is a noticeable aspect because it is the proof of the fact that at high-energy the particles contribution to the mixed field is yield by neutrons. Protons, and pions are negligible compared with the neutron fluxes (note that both axis on the graph are in logarithmic scale, the protons at 100 MeV for instance, are lower by two orders of magnitude compared with the neutrons). In this respect the neutron flux was selected as input for the subsequent simulation. Furthermore, for the same reason the output after the boron carbide for these minor particles is not a concern and therefore it will be not evaluate. The main difference among the two configurations is that with the full shielding the intensity fluences are lower compared with those retrieved without shielding, for what concern neutrons and HEHeq. Only pions, kaons and muons present a different spectra but we are not interested in, since their levels relative to HEHeq are very low. The neutron spectra has been therefore employed as data for the simulation by using the boron carbide, in order to see how the neutrons are absorbed from the material and in which energy range. The geometry model is that presented in Figure 2.19 with a view on the lateral side where the objects extend on the x direction.

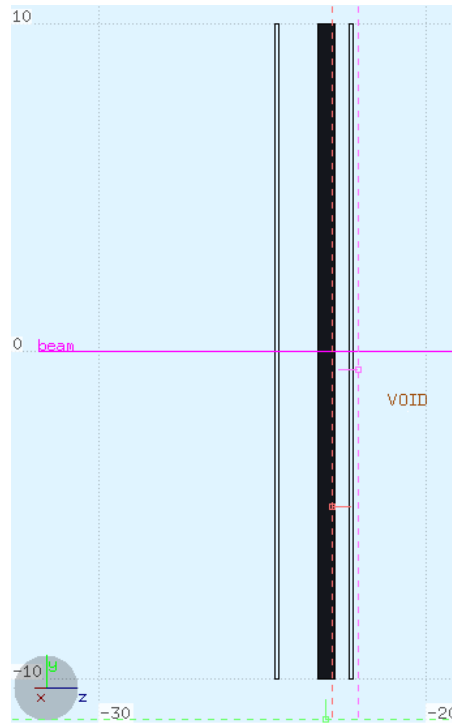


Figure 2.19: Boron carbide geometry in FLUKA with detectors.

Starting from the beam to the right, it is set to be $20 \times 20 \text{ cm}$ in wide and it contains the particles spectra from the previous simulation. It is to be noted that considering a single tile instead of the complete box as geometry is not reductive, because the simulation is performed as it is independent with respect to the CHARM facility. The data input is not the spectra over a volume (only in this case the 6 tiles box would be necessary) but rather the spectra over a surface. For one moment we forgot that it is related with the actual spectra over M0. For the same reason the distance between beam, tile and detectors is irrelevant. The beam crosses through the first detector used for the only purpose of checking that the spectra is the same of the input, then it crosses the boron carbide tile of $20 \times 20 \times 0.5 \text{ cm}$ and finally it reaches the second detector. The two detectors constituted by air, are only a mean for scoring the particles flux: their size has to be considered only for what concern the normalization factor of the plots but do not affect other variables. FLUKA returns a file with four columns: minimum energy, maximum energy, track length and statistical error, the latter strongly dependent from the number of primaries. The track length is the path crossed by a particle in the scoring volume and in the FLUKA output is expressed in $[\text{cm}/(pp \cdot \text{GeV})]$ with pp the primary particle. To obtain the real fluence, this result has to be divided by the sensitive volume of the detector.

$$\frac{d\Phi}{dE} = \frac{\sum_i l_i}{V_{\text{volume}}} \left[\frac{1}{pp \cdot \text{GeV} \cdot \text{cm}^2} \right] \quad (2.16)$$

Moreover this quantity is typically indicated through the lethargy, as in this way is possible to see the fluence peaks as function of the energy; otherwise one would see a decreasing trend. This purpose is achieved by multiplying the differential fluence by the mean value of energies:

$$\frac{d\Phi}{d\ln(E)} = \langle E \rangle \cdot \frac{d\Phi}{dE} \left[\frac{1}{pp \cdot \text{cm}^2} \right] \quad (2.17)$$

It is to be noted the fact that FLUKA always normalize by primary particles.

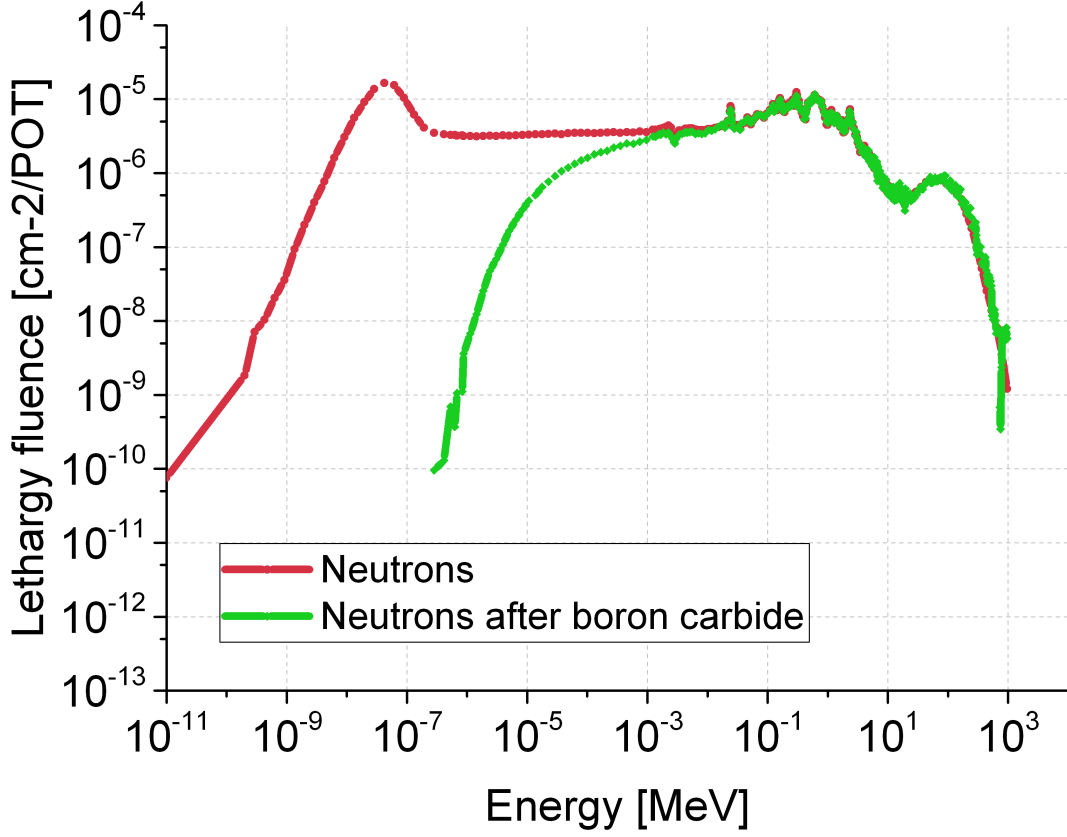


Figure 2.20: Neutron spectra before and after the employment of the boron carbide in M0 position with CU-OOOO configuration.

As shown in Figure 2.20, FLUKA simulations with the 5 mm thickness of boron carbide evidence that the neutron spectra is fully absorbed below 1 eV and partially cut until 0.01 MeV, while the high-energy flux is hardly affected. Therefore, this simple local shielding solution can be used to significantly alter the R-factor (thermal to high-energy hadron flux ratio) for a given experimental position.

2.6 Comparison with shielded areas in accelerator and atmospheric spectrum

2.6.1 Radiation environment in the LHC

The high-energy hadron fluence for the future High-Luminosity LHC accelerator (HL-LHC, an upgrade of the existing machine, to operate as of 2025) was calculated using the FLUKA code [8] and it can be seen in Figure 2.21 for the area in the vicinity of the Point 1 interactions, corresponding to the ATLAS experiment. As can be outlined, the alcove

named UJ16, despite being behind a significant amount of shielding (roughly 2 meters of concrete) with respect to the interaction point and beamline, is expected to have annual HEH levels of roughly 10^{10} cm^{-2} , comparable to annual fluxes above 20 MeV encountered in the trapped proton belts [9]. Whereas SEE failures in accelerator equipment are typically less critical than for space system, the significant amount of involved units and large radiation levels can seriously compromise the machine performance.

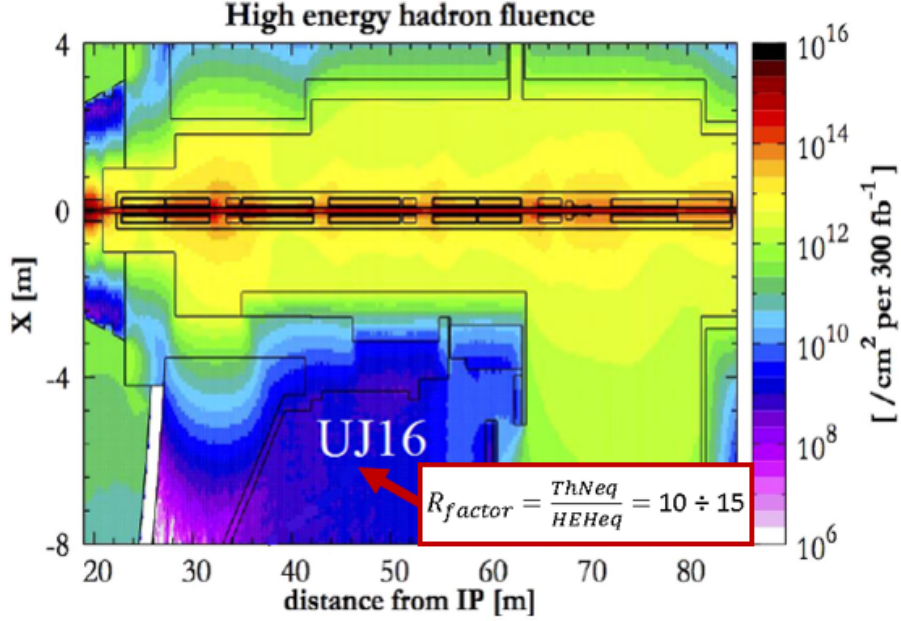


Figure 2.21: Simulated HEHeq fluence for the HL-LHC and the R-factor in the alcove as measured with the RadMon for the present LHC machine.

Furthermore, the neutron spectra at sea level shielded with 1 m of concrete has the similar behaviour of that at CHARM, especially for the thermal neutrons as can be seen in Figure 2.22. It is to be noted that CHARM applies an accelerator factor to the neutron flux, as 1 second of testing in the latter corresponds to 1 year of exposition at sea level ([19]).

In Figure 2.23 the CHARM neutron spectra in positions M0 (CHARM(A)) and R10 (CHARM(B)) is displayed for the configuration without shielding, in comparison to that of the JEDEC standard [16]. The latter is a reference neutron spectrum as a function of the energy measured in New York City outdoors at sea level. The CHARM flux is retrieved from the FLUKA simulations and normalized with the fluence of the JEDEC standard above 10 MeV, as follows:

$$\varphi(E) = \left(\frac{d\varphi}{dE} \right)^{FLUKA} \cdot \frac{\Phi_{(>10\text{MeV})}^{JEDEC}}{\Phi_{(>10\text{MeV})}^{CHARM}} = \left(\frac{d\varphi}{dE} \right)^{FLUKA} \cdot \frac{1}{A} \quad (2.18)$$

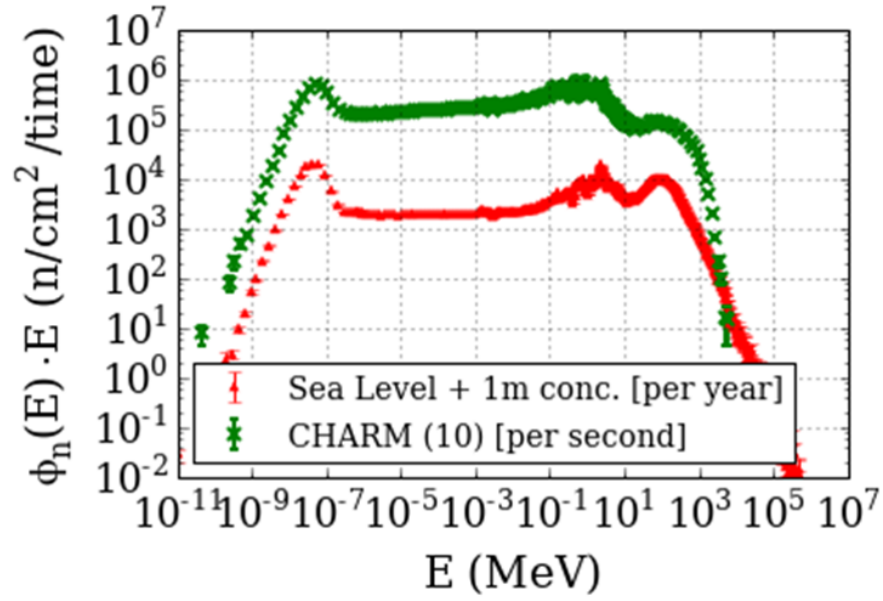


Figure 2.22: Neutron spectrum comparison between position 10 at CHARM and that present at sea level under one meter of concrete.

The factor A is the accelerator factor. Whereas the four spectra are compatible until $2 \cdot 10^2 \text{ MeV}$, for larger energies M0 reflects UJ and R10 follows the JEDEC spectra.

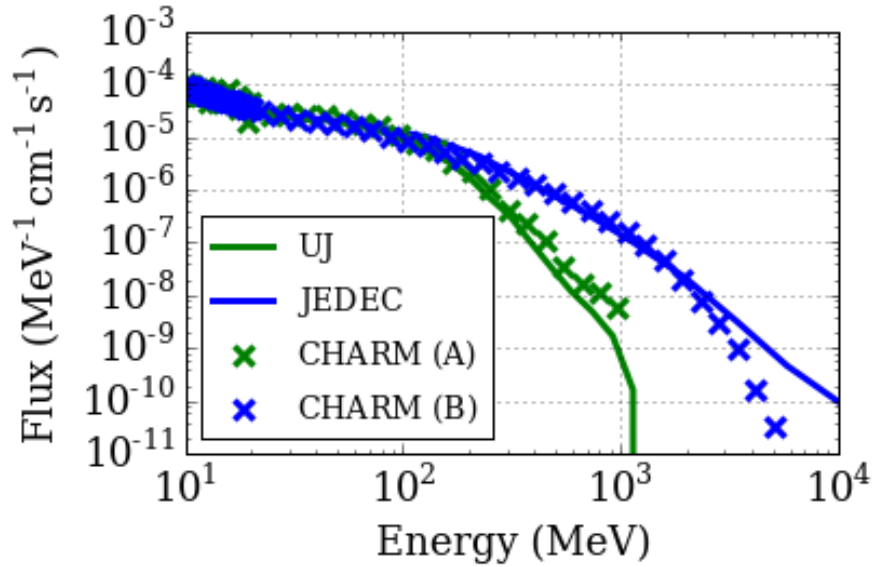


Figure 2.23: Neutron spectrum comparison between the position 10 at CHARM (A), M0 (B), the alcove UJ and the JEDEC standard.

Chapter 3

SEE test results at CHARM for thermal and high-energy neutrons

In this chapter, a general overview concerning the type of Single Event Effects studied in this work is outlined: Single Event Upset and Single Event Latch-up. Following it continues on the description of the equipment and setups employed to measure these effects on the memories. Then, the heart of the approach to derive both thermal and HEHeq cross sections thorough the differential measurements with the boron carbide box will be explored and finally, the SEE results obtained with this procedure at the CHARM facility will be shown.

3.1 Measured effects, components tests and experimental setups

3.1.1 SEU and SEL effects

A Single Event Effect (SEE) is a stochastic effect due to an ionizing particle that hits a sensitive volume in a device at the wrong time. It is not a cumulative effect but it can be either non-destructive, also called soft error like the SEU or destructive, where permanent physical damage is produced even if in some cases, as for SEL, the operation of the memory can be restored with a prompt power cycle. They are feared because these events may affect digital-analog logic, power components and therefore compromise the correct operation of the electronics.

Single Event Upset (SEU) consists in a bit flip of a memory cell, so that a logic 1 becomes a logic 0 or vice-versa, i.e data corruption. It is a soft error because the proper functioning

of the device can be restored with a power cycle or re-writing the memory cell.

In general these phenomena is generate on the reverse-biased p-n junctions when a charged particle strikes the latter as shown in Figure 3.1.

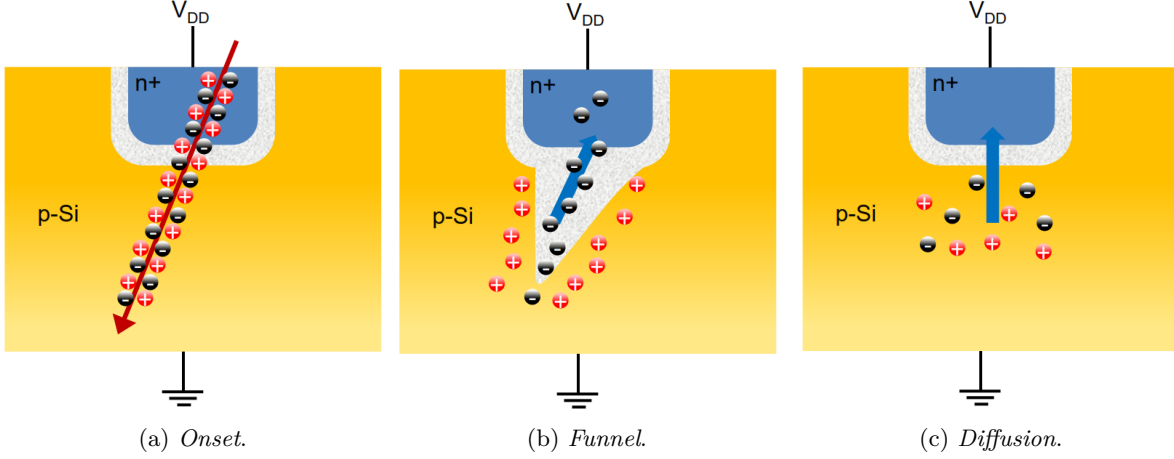


Figure 3.1: Charge for inducing SEL three phases generation (from [10]).

However in this study most of the upsets are produced by neutrons that are not charged particles but they can collide against the atoms in the sensitive volume and its surroundings (BEOL, active silicon), releasing a shower of charged particles (for instance by nuclear reaction). Therefore in both cases the impinging particle leaves an ionisation track composed of hole-electrons pairs (Onset phase). This production of charged particles deforms the depletion region and the corresponding electric field is extended downward in the substrate creating a funnel. Owing to the presence of high electric field for separating electrons-holes and since the collection volume increased due to the funnel, the charged particles are separated producing a drift current immediately collected (few ps). As the last process depletes the funnel, the residual particles still present in the substrate are not any more attracted from the voltage but they can move by diffusion. This third phase is slower (order of ns) and typically not as critical as the drift.

Let's focus on the repercussions that this extra charge may have on the SRAM. A typical cell of SRAM memory is composed by 6 MOSFET of which the two couple in the middle form two CMOS inverters (see Figure 3.2). In a first stage, the voltage on the drain to the rightmost MOSFET is positive and indicated with "1". The right n-MOS structure is explored in its physical structure on the picture and the latter is turned off because its gate has 0 voltage (b). The bit information of the SRAM memory is retain in V_Q and V_{NQ} . When the neutron impacts against the substrate, the collision generates charged particles as described before and the electrons are attracted on the node Q; his negative

charge tends to bring its voltage down. The node capacitance slows down the voltage variation and it could be able to stop the transient also thanks to the respective inverter p-MOS, which starts to turn-on and restore the lost charge. In this case when the voltage transient induced by the drift current is below the switching threshold, there is no cell flip (c). Otherwise, if the particles carried enough energy to produce many ionizing charges the cell may change status and this event is called SEU (d).

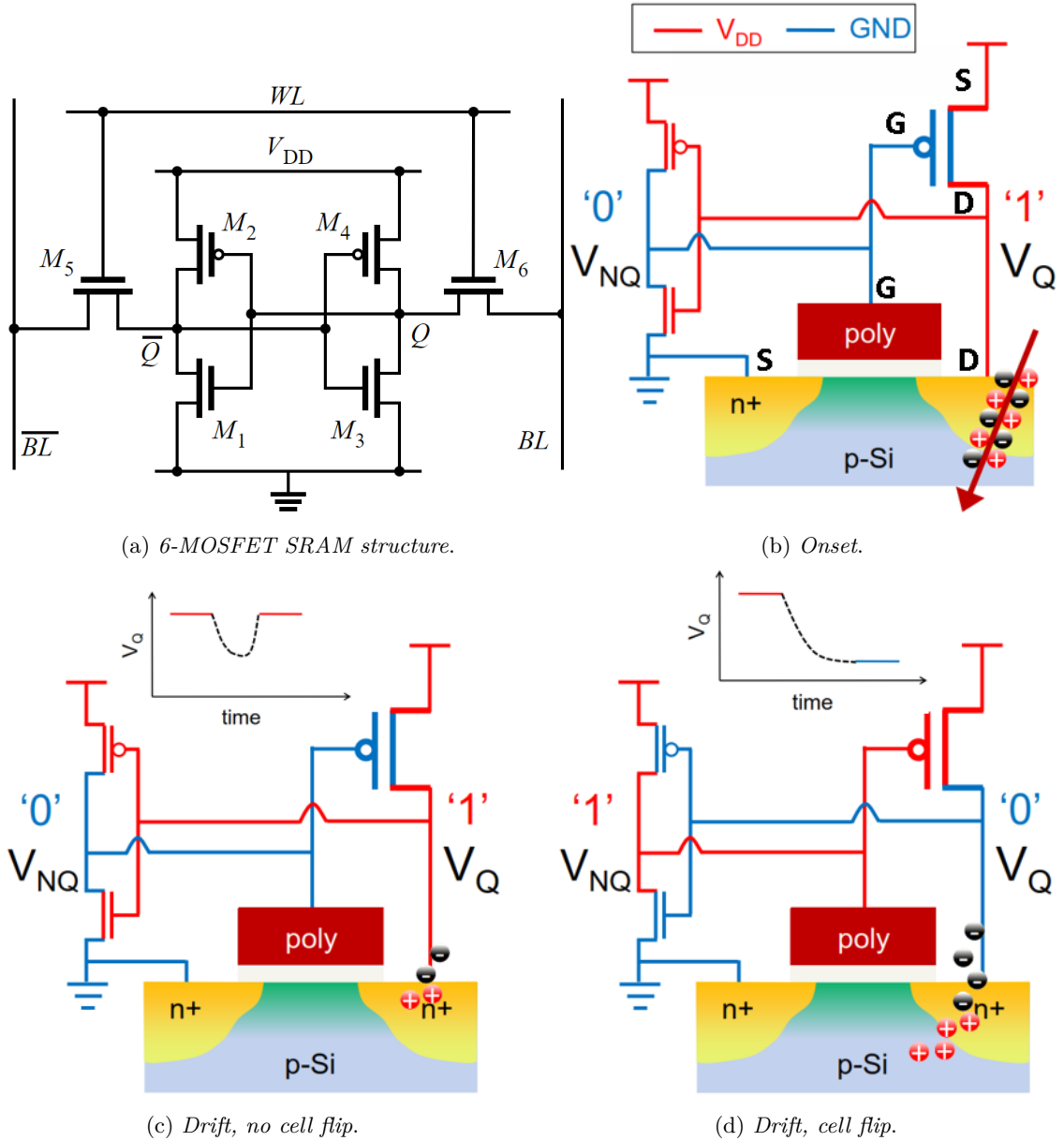


Figure 3.2: Single event Upset on a 6 MOSFET SRAM (from [10]).

As opposed to SEU, the Single Event Latch-up (SEL) is not a soft error but rather

a destructive event owing to the activation of two parasitic bipolar transistors in the MOSFET substrate. In the event that this current is not cut in a short time by a control circuit or an external power cycle, the component can be permanently injured. The working principle is exposed in Figure 3.3 which represents a CMOS inverter, as that constituted by M1 and M2 in Figure 3.2a. When the particle passes through the N-well, it induces ionizing charge with consequent current that flows through the well, the latter modelled as a resistance R_W . Therefore, there is a voltage drop on it and the parasitic transistor Q1 could turn-on when $V_{EB} > 0.7$ V. If that happens, the current supplied by Q1 produces a potential drop on the substrate resistance R_S and in the same way it can activate the transistor Q2. The current through R_W increases as it is recalled by Q2, so that Q1 is switched-on more and more, in a loop that leads a catastrophic damage due to the high current.

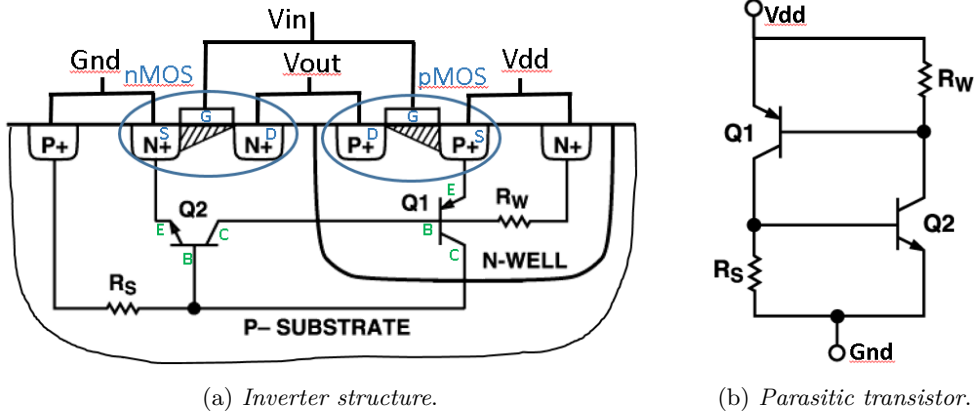


Figure 3.3: Single Even Latch-up principle (form [12]).

3.1.2 Tested components

During 2016 and 2017 different SRAM based memories were tested at the CHARM facility for three reasons:

1. to explore the possibility of retrieving the previously calibrated cross sections through the differential boron carbide measurements that was proven (see Chapter 2.5) of reproducing the LHC environment with a broad variety of R-factors. For all the memories, the HEHeq cross section was retrieved, and so was the thermal neutron cross section for the ESA Monitor.
2. to evaluate the thermal neutron impact over the memories retrieving the corresponding cross sections.
3. to benchmark the results with those obtained in standard mono-energetic facilities.

The complete list of tested memories with respective SEE measurement can be found in Table 3.1, so far focusing on well-known components regarding the HEH response. References and date codes are reported in more details below.

Table 3.1: Memories employed for SEU and SEL tests.

Memory	SEE	Part reference	Tech	Size
Esa Monitor	SEU	AT68166F	0.25 μm	16 Mbit
Esa Monitor	SEU	AT68166H-YM20-E	0.25 μm	16 Mbit
ISSI	SEL	IS61LV5128AL-10TLI	0.18 μm	4 Mbit
Brilliance	SEL	BS62LV1600EIP55	0.18 μm	16 Mbit
Lyontek	SEL	LY62W20488ML-55LL	0.18 μm	16 Mbit
Alliance	SEL	AS7C34098A-10TCN	0.20 μm	4 Mbit

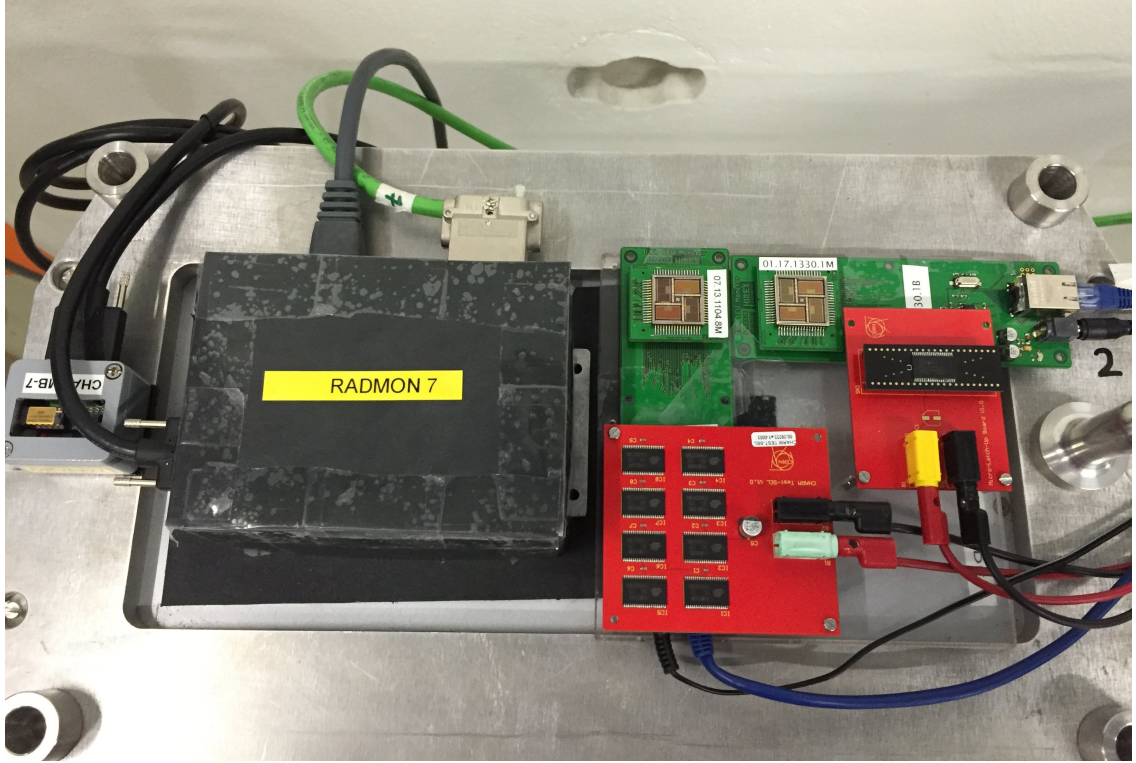


Figure 3.4: Radmon, ESA SEU Monitor, Brilliance 1x and Lyontek memories above M0 before the irradiation.

SEL: components and experimental setup

For the SEL tests, COTS memories of the same type were employed (sometimes with different date codes). The test boards were developed at CERN with two inputs ground and Vcc, housing 8x chips soldered on it except for the Brilliance 11254 that was formed

3.1. Measured effects, components tests and experimental setups

by a single chip 1x (see Table 3.2). No output signal (i.e. read/write) was present since the SEL detection is implemented through the measurement of the supplied current. They were tested inside and outside the boron carbide cube. Brilliance and Lyontek memories

Table 3.2: SEL memories details.

Memory	Part reference	Date code	Tech	Size	Nominal voltage [V]
ISSI	IS61LV5128AL-10TLI	1246, 1303, 1416	0.18 μm	512K x 8	$3.3 \pm 10\%$
Brilliance	BS62LV1600EIP55	12094, 11254	0.18 μm	2048K x 8	$2.4 \div 5.5$
Lyontek	LY62W20488ML-55LL	1251	0.18 μm	2048K x 8	$2.7 \div 5.5$
Alliance	AS7C34098A-10TCN	1339, 1205	0.20 μm	256k x 16	$-0.5 \div 5.0$

were equipped with 8x chips with the same date code, the ISSI memory had 3 different date codes installed on the same board whereas two date codes for the Alliance, as shown in Figure 3.5. In order to distinguish one board from the other (also with the same memories installed) there was a label with a different code that can be used to evaluate the board-to-board sensitivity spread.



Figure 3.5: Brilliance 8x and ISSI 8x memory boards (Lyontek has the same base board as well).

The boards were connected with a banana - BNC cable to a power supply: a KEYSIGHT E3648A. This device can be controlled with a computer by means of the GPIB-USB-HS controller using a LabVIEW software *PsControl* (Figure 3.7). This program can count the number of SEL that occur in the memories. It provide two output channels so we were able to test two different boards at a time. This program is able to count the number of SELs that occur in the memories, it also provides the peak current consumption during the SEL. There are three main input parameters to detect and reset a SEL as illustrated

in Figure 3.6:

- the current threshold (I-thres).
- the hold time (t-hold).
- the cut time or reset time (t-cut).

SEL detection is carried out reading the current consumption of the component. When the latter increases above the current threshold and it lasts for the hold-time, the voltage is set to 0V for the cut-time and finally the component is powered up again with the nominal voltage. In the analysis, as the memory can not suffer a SEL during the hold and reset time also if the particles fluence is still coming, the dead-time needs to be accounted for. With low SEL probabilities per spill (as was the case during our experiments), a SEL has a uniform probability of occurrence during the spill, therefore statistically only half of the protons on target (POT) carried by the spill which produce SEL, have to be considered to calculate the effective fluence on the memory. Usually one spill lasts 350ms and $t_{hold} + t_{cut}$ lasts about 1.5 seconds. As SEL are separated by 80 seconds, it is rather unlikely that SEL detection and reset time can overlap to the next latch-up.

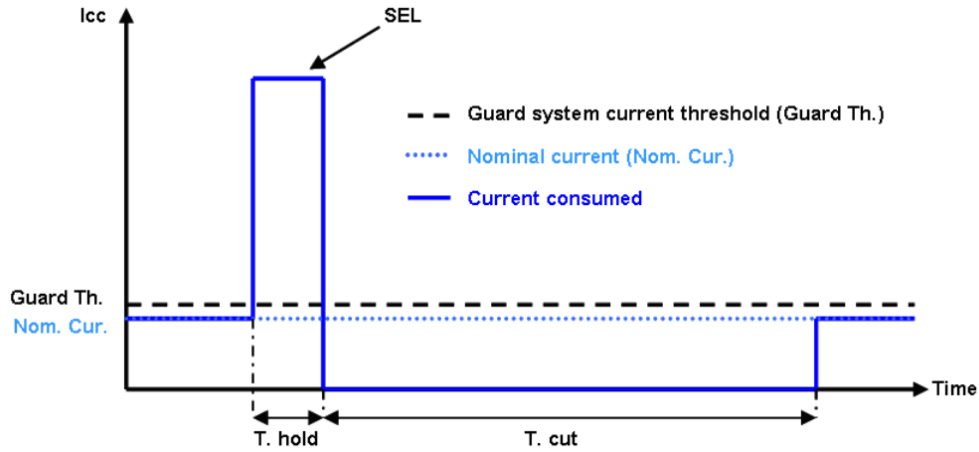


Figure 3.6: SEL cycle: detection and restore.

Table 3.3 shows the main settings set in the PS Control (LabVIEW software) for currents and voltages. Note that, especially for the ISSI memory board that absorbs about 300 mA, there is a voltage drop owing to the resistance of the BNC to BNC long cable that it's of about 0.097 ohm/meter, calculated making the difference between the two voltages (power supply and board voltage) and dividing it by the current and the cable length. Therefore, a voltage of 3.67V was applied to the power supply in order to

3.1. Measured effects, components tests and experimental setups

power the board to 3.3V. The other memories did not require the previous adjustment because their current consumption is very low and therefore the power dissipation on the cable is negligible.

Table 3.3: SEL parameters set on PS control software. The Voltage is that on the board, and it could be different from the power supply output voltage, due to the voltage drop on the cable.

Component	Voltage(V)	Inominal (A)	Ithres (A)	thold (s)	treset (s)
ISSI	3.3	0.265	0.3	0.89	0.6
Brilliance	3.3	0.01	0.02	0.89	0.6
Lyontek	3.3	0.005	0.02	0.89	0.6
Alliance	3.3	0.035	0.08	0.89	0.6

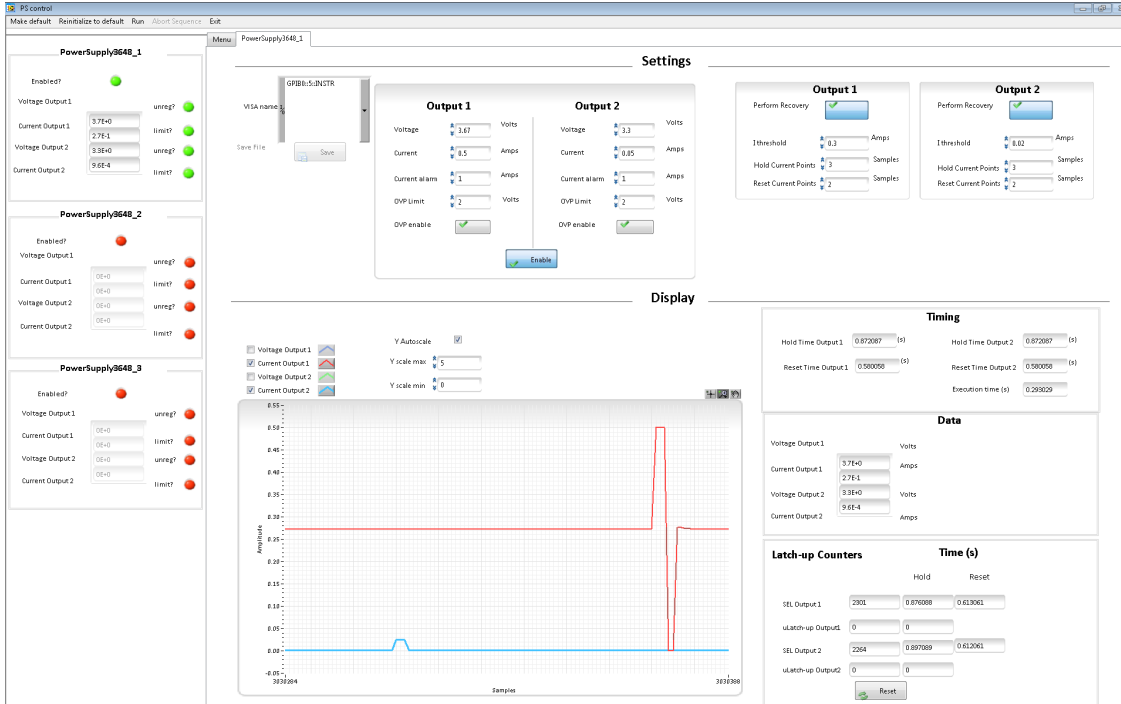


Figure 3.7: PS control software showing a SEL event, the program displays in real time current and voltage evolution for both the channels.

SEU: ESA Monitor and experimental setup

The ESA SEU Monitor is a system developed by HIREX containing a chip module of 16 Mbit SRAM designed for space applications. The later is a multi chip module, radiation hard tolerant and with Multiple Bit Upset immunity. Writing and reading are performed with a software provided by HIREX and through an Ethernet connection with

the board. The peripheral electronics (e.g. microcontroller, voltage regulator, communication) installed on the board together with the memory, are not robust to radiation as the monitor was initially designed for its use in collimated beam applications. Table 3.4 outlines the two memories employed in the tests. They are supposed to be quite similar since the part reference is basically the same but as will be shown their cross sections are slightly different. Moreover, the ESA Monitor board with date code 1104, deployed for the CHARM tests during 2016, has been showing a great capacity of enduring radiations compared with the new one 1330 employed during 2017.

Table 3.4: ESA SEU Monitor specifications.

Memory	Part reference	Date code	Tech	Size	Nominal voltage [V]
ESA Monitor	AT68166F	1104	$0.25\ \mu\text{m}$	4x512Kx8	3.3 ± 0.3
ESA Monitor	AT68166H-YM20-E	1330	$0.25\ \mu\text{m}$	4x512Kx8	3.3 ± 0.3

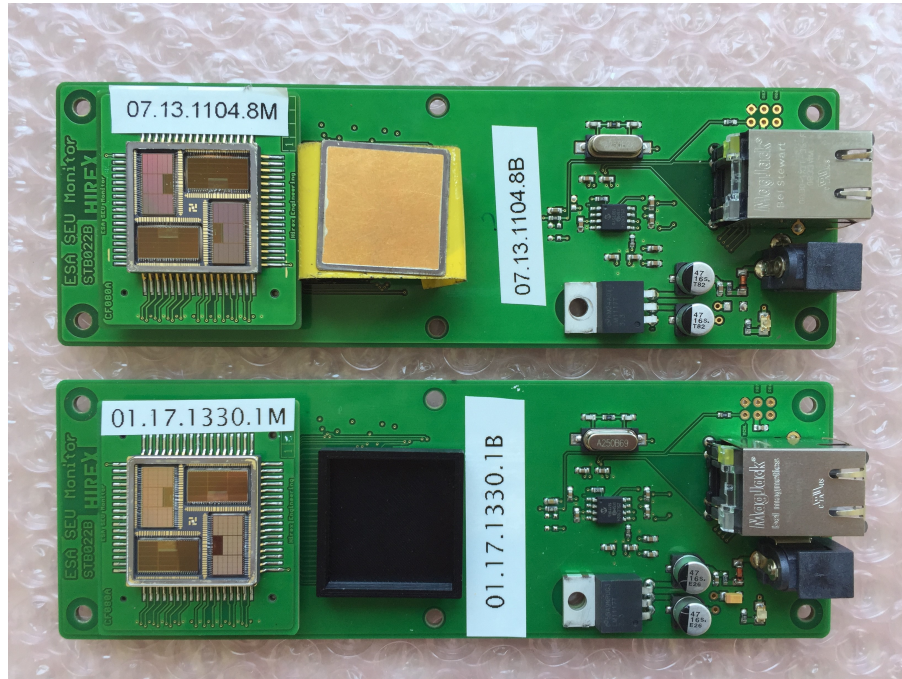


Figure 3.8: ESA SEU Monitor boards, on the left the de-capsulated memories with the respective lid to the right, the upper board is the AT68166F 1104 and the bottom one is the AT68166H 1330.

The memory is formed of 4 dies, which altogether cover an area of $19,8 \times 19,8\ \text{cm}^2$ (depicted in Figure 3.9). With the purpose of directly irradiating the chips, the active memory area can be opened and exposed without protections. The latter is a lid composed

by kovar, a nickel-cobalt alloy for the 1104 and plastic for the 1330, as can be seen in Figure 3.8. The software permits to write all the dies with a CHKBD pattern, namely the memory is written with consecutive 0 and 1.

At the end of the irradiation period (2016) or during it (2017), the memory is read to compare the binary data in each cell with the initial pattern and, when the reference pattern didn't match with the post-irradiation one, an SEU counter is incremented. It is to be noted that the memory was not written again after the reading; this aspect could decrease the sensitivity of the memory in terms of taking over the upsets because some bits are already flipped but, considering the memory size of 2^{24} bits, the probability of hitting the same flipped bit is regarded as negligible.

The number of errors in each die is displayed as well as their physical arrangement within the memory. The latter is a very useful tool to evaluate whether the flow of particles hit the memory homogeneously. Furthermore, the total number of upsets as well as their physical disposition inside the memory can be shown for each die. As mentioned, during the 2016 tests, the memory was supplied with its own power supply and read at the end of the irradiation, instead in 2017 we powered up the memory through the Agilent power supply from the control room, the same used for the latch-up tests and read-out automatically the memory every 15 minutes by means of a script. This effort was needed since, many times during 2016 we lost the data due to communication problems and, as will be further explained ahead the new 1330 memory suffers much more of SEL complications, which yields a wrong reading.

In order to perform the measurements with the boron carbide shielding, a proper "bunker" was built leaving only the cables to pass in, as shown in Figure 3.10. Even if not very evident in the picture, the ESA Monitor inside the box was completely shielded in all the sides, including the front.

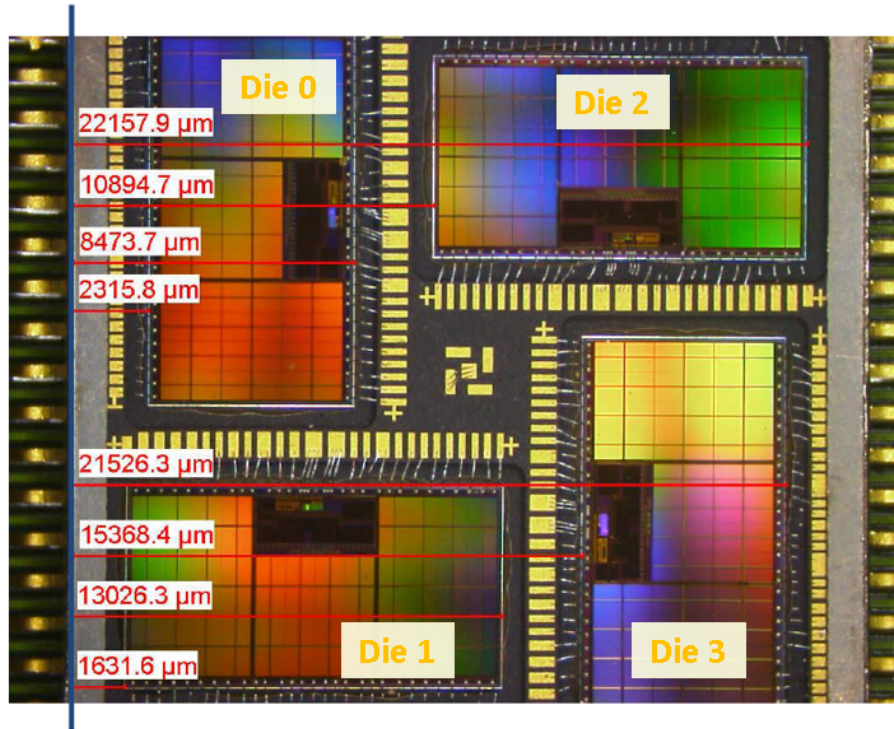


Figure 3.9: ESA SEU Monitor dimensions and disposition of the four dies from [11]. The memory orientation is in vertical with the power supply connector to the bottom.

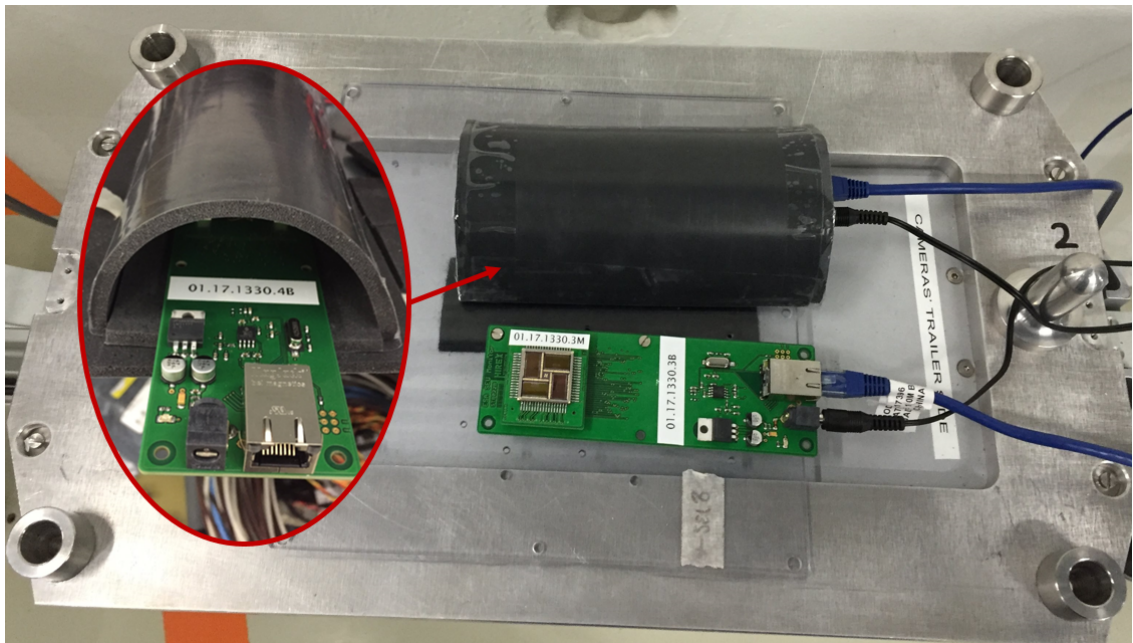


Figure 3.10: Two ESA Monitor above the Montrac in M0 position at CHARM, ready to be irradiated. Typical example of differential measurement with and without boron carbide.

3.2 Proposed mixed-field differential approach

To introduce the experimental procedure to unfold the thermal and high-energy hadron contributions to the SEE rate in the mixed-field environment we should distinguish the case regarding SEU and that for SEL.

The reference memory for this study is the ESA SEU Monitor, introduced above in section 3.1.2. Through two different measurements of the SEU number, carried out placing the memory inside the boron carbide box and accomplishing the same test with the memory outside the neutron shielding, two different values of upsets are obtained. This procedure can be performed, either testing two memories with same reference and date code for the same period of time, or by using only one memory in two different runs (with the same facility configuration). In this latter case, the irradiation time is not required to be the same because, as shown in the TIMBER analysis 2.5, it is always possible to retrieve the fluence in $[particles/cm^2]$ on the specific position at CHARM. In addition, this operation may be unfolded by obtaining the fluence from experimental data (RadMon, outlined in 2.5.1) or from FLUKA simulations that return the values normalized by proton on target (POT). Indeed, handling fluxes and fluences at the CHARM facility on which this approach relies on, the former are not so relevant as for instance in other facilities, where the fluence is derived multiplying flux by time. At CHARM, the flux in unit of time is somehow replaced by the fluence in unit of POT. To come back to the main point, the two SEU counts from the differential measurement, enclose the information concerning the sensitivity to thermal neutron and HEHeq, as described through the following system of equations:

$$\begin{cases} N_{SEU} = \sigma_{HEH} \cdot \Phi_{HEHeq} + \sigma_{thn} \cdot \Phi_{thn} \\ N_{SEU}^{B_4C} = \sigma_{HEH} \cdot \Phi_{HEHeq}^{B_4C} + \sigma_{thn} \cdot \Phi_{thn}^{B_4C} \end{cases} \quad (3.1)$$

Where B_4C is the chemical formula for indicating the boron carbide. System 3.1 looks like to that presented in the RadMon analysis but, in this latter, the cross sections were all four different and known terms. Now, the two cross sections σ_{HEHeq} and σ_{thn} are the unknowns, whereas the fluences are known variables thanks to the RadMon calibration, formerly carried out on M0. Fluences are obtained multiplying the CHARM POTs by the relative RadMon fluence in $[cm^{-2}/POT]$ and as discussed above, it should not come as a surprise the fact that these fluences can derive from different weeks. Cross-sections are represented in $[cm^2]$ and dividing these values by the respective bit number of the memory (for example 2^{24} in the case of the ESA Monitor, corresponding to 16 Mbit) in $[cm^2/bit]$. In the end, the second equation to solve the system is introduced by the boron carbide, otherwise it would be impossible to obtain the two cross sections. Moreover,

from the FLUKA simulation depicted in Figure 2.20 the HEHeq fluence are not affected by the boron carbide so that the second equation can be written as

$$\begin{cases} N_{SEU} = \sigma_{HEH} \cdot \Phi_{HEHeq} + \sigma_{thn} \cdot \Phi_{thn} \\ N_{SEU}^{BAC} = \sigma_{HEH} \cdot \Phi_{HEHeq} + \sigma_{thn} \cdot \Phi_{thn}^{BAC} \end{cases} \quad (3.2)$$

Note that, although theoretically $\Phi_{HEHeq} = \Phi_{HEHeq}^{BAC}$ the RadMon measurements showed a difference within 20 and 40% for Cu-OOOO and Cu-CIIC respectively. However assuming that 3.2 is verified as the simulations suggest, the system 3.2 can be solved as follows. Dividing both equations by Φ_{HEHeq} and, for simplicity of notation we indicate with ^B as superscript the terms regarding the boron carbide and with $\sigma^* = N/\Phi_{HEHeq}$ an experimental cross section because it takes into account all possible SEU contributions:

$$\begin{cases} \sigma^* = \sigma_{HEH} + \sigma_{thn} \cdot R_{eq} \\ \sigma_B^* = \sigma_{HEH} + \sigma_{thn} \cdot R_{eq}^B \end{cases} \quad (3.3)$$

Subtracting the second equation to the first one, the thermal neutron cross section is retrieved:

$$\sigma_{thn} = \frac{\sigma^* - \sigma_B^*}{R_{eq} - R_{eq}^B} \quad (3.4)$$

Since $R_{eq}^B = \Phi_{thn}^B/\Phi_{HEHeq}^B$, the numerator represents the thermal neutron fluence with the boron carbide shield and with a complete cover box, as proved from simulations and experimental RadMon data, that term is very close to zero and therefore the ratio tends to zero as the denominator is a positive quantity. To this regard R_{eq}^B is negligible compared with R_{eq} , so finally:

$$\sigma_{thn} = \frac{\sigma^* - \sigma_B^*}{R_{eq}} \quad (3.5)$$

Expression 3.5 is valid in general also performing the differential measurements in different weeks. Further expanding 3.5:

$$\sigma_{thn} = \frac{N - N_B}{\Phi_{thn}} \quad (3.6)$$

although in this case, since the information regarding the HEHeq fluences are lost, the relation could not be any more valid if the differential tests are carried out in different weeks, because the POT number may be different among the runs. This result says that with the only knowledge of the thermal neutrons fluence and through the differential measurement, the thermal neutron cross section can be derived, independently from the HEH fluence.

In the same way, after some passages:

$$\sigma_{HEH} = \frac{\sigma^*(R_{eq} - R_{eq}^B - 1) + \sigma_B^*}{R_{eq} - R_{eq}^B} \quad (3.7)$$

and again with the approximation that $R_{eq}^B \mapsto 0$:

$$\sigma_{HEH} = \frac{\sigma^*(R_{eq}^B - 1) + \sigma_B^*}{R_{eq}} = \frac{1}{\Phi_{HEHeq}} \left[N \left(1 - \frac{1}{R} \right) + \frac{N_B}{R} \right] \quad (3.8)$$

The HEH cross section is a bit more complex and it requires both fluences (contained in the R factor).

The last two forms for σ_{thn} and σ_{HEH} , require the hypothesis that the thermal fluence is completely absorbed by the boron carbide. The term can be neglected all the more the difference between R_{eq} and R_{eq}^B is higher. For this reason not every location at CHARM is equally suitable. Locations inside the irradiation chamber for instance, posses an R factor equivalent within a factor 3 (simulations) with the most common configuration Cu-OOOO. In these cases the hypothesis is not as strong as in position M0, where R_{eq} assumes a value of 12 from the FLUKA simulations and a value of 8.8 by experimental measurements. The best would be perform the differential measurements with the full shielding Cu-CIIC owing to the very high R-factor values which can be obtained (up to a measured factor of 33 regarding M0). Moreover, taking into account the relative hypothesis, the relative uncertainty concerning the thermal neutron cross section, from 3.6 is determined from only the thermal neutron fluence contribution.

Regarding the SEL analysis instead, the HEH SIMULATED fluence is employed (and not the HEHeq); in this way the intermediate energy neutrons are not considered because their contribution in the HEH cross section is negligible compared with that of high-energy hadrons. Moreover, HEHeq relies on the RadMon Toshiba cross section concerning SEU, therefore the response is different from that of SEL. In addition, the thermal neutron cross section is considered to be zero as thermal neutrons are typically regarded as being incapable of inducing SEL. This hypothesis was confirmed through the comparison of measurements with and without boron carbide, compatible with the experimental error and through the test (on the Brilliance) performed in a thermal neutron reactor in Grenoble (see Chapter 4.1). The following equation explains how the HEH latch-up cross sections are retrieved:

$$N_{SEL} = \sigma_{HEH} \cdot \Phi_{HEH} + \sigma_{thn} \cdot \Phi_{thn} \quad (3.9)$$

and dividing all the terms by Φ_{HEH} :

$$\sigma_{HEH}^* = \frac{N_{SEL}}{\Phi_{HEH}} = \sigma_{HEH} + \sigma_{thn} \cdot R \quad (3.10)$$

The measured HEH cross section carries the contributions of thermal neutrons and HEH fluences (inside the R-factor). Since the results with boron carbide absorber and without it is basically the same, we can assume that the thermal neutron cross section tends to zero. If the hypothesis is verified, the measured cross section σ_{HEH}^* at CHARM is equal to the standard cross section σ_{HEH} .

As described above and from what suggests the following results, this approach can be extended through its application to state-of-the-art components.

Uncertainty assessment

Equation 3.1 can be solved by applying the Cramer's method:

$$\sigma_{HEH} = \frac{N \cdot \Phi_{thn}^B - N^B \cdot \Phi_{thn}}{\Phi_{HEHeq} \cdot \Phi_{thn}^B - \Phi_{thn} \cdot \Phi_{HEHeq}^B} \quad (3.11)$$

$$\sigma_{thn} = -\frac{N \cdot \Phi_{HEHeq}^B - N^B \cdot \Phi_{HEHeq}}{\Phi_{HEHeq} \cdot \Phi_{thn}^B - \Phi_{thn} \cdot \Phi_{HEHeq}^B} \quad (3.12)$$

Both cross sections are function of four variables:

- $\sigma_{thn} = f(\Phi_{thn}^B, \Phi_{thn}, \Phi_{HEHeq}^B, \Phi_{HEHeq})$
- $\sigma_{HEHeq} = f(\Phi_{thn}^B, \Phi_{thn}, \Phi_{HEHeq}^B, \Phi_{HEHeq})$

By calling x_i the generic variable, it has associated the absolute uncertainty Δx_i . In other words $x_i \pm \Delta x_i$ and by employing the uncertainty propagation:

$$\Delta f = \sqrt{\sum_{i=1}^4 \left(\frac{df}{dx_i} \cdot \Delta x_i \right)^2} \quad (3.13)$$

In our case, Δx_i is given by the expected value of the variable, multiplied by the measurement relative error which for the fluences derives from the RadMon system and POT (SEC1) contributions. The uncertainty for the former is assumed to be 25% and for the SEC1 considering two standard deviation is 10.44% (from Table 2.2). Therefore:

$$\Delta x_i = \Phi_i \cdot \sqrt{0.25^2 + 0.1044^2} = \Phi_i \cdot 0.27 \quad (3.14)$$

Observation To reduce as much as possible the uncertainties referred to the cross sections, it can be noted that by deriving the cross sections as a function of the fluences (from 3.14) all the denominators contain the term $(\Phi_{HEHeq} \cdot \Phi_{thn}^B - \Phi_{thn} \cdot \Phi_{HEHeq}^B)^2$ to be made as large as possible. It can be developed as as function of the R-factor; by assuming negligible the differences over the HEH fluences using the boron carbide or not:

$$\begin{aligned}
 (\Phi_{HEHeq} \cdot \Phi_{thn}^B - \Phi_{thn} \cdot \Phi_{HEHeq}^B)^2 &= (\Phi_{HEHeq} \cdot (\Phi_{thn}^B - \Phi_{thn}))^2 = \\
 &= (\Phi_{HEHeq}^2 \cdot (R_{eq}^B - R_{eq}))^2 = \\
 &\approx \Phi_{HEHeq}^4 \cdot R_{eq}^2
 \end{aligned} \tag{3.15}$$

This proves that higher is the R-factor on the test position and lower is the uncertainty. Therefore the results obtained selecting the full shielding configuration at CHARM are supposed to be more accurate since the R-factor is the largest.

3.3 SEU results

The ESA SEU Monitor has been essential for experimentally verifying the differential approach. Therefore it was tested with different boron carbide cover and with two shielding configuration, full shielding and without it, which represents the two extremes of radiation environment. The other purpose of the ESA Monitor was checking the neutron homogeneity over M0 that is simultaneously performed with the tests. For the latter aspect, the results showed that the homogeneity was quite good for all the tests as displayed on the ESA software in Figure 3.11. Nevertheless, more than once the reading of these memories was not feasible due to lost of communication between software and board (a study about the cause of this abnormal behaviour can be found in the annex 6). Basically, these kind of problems can be classified as: micro-Latch-up events, single event functional interrupt (SEFI) or/and due to the power supply voltage.

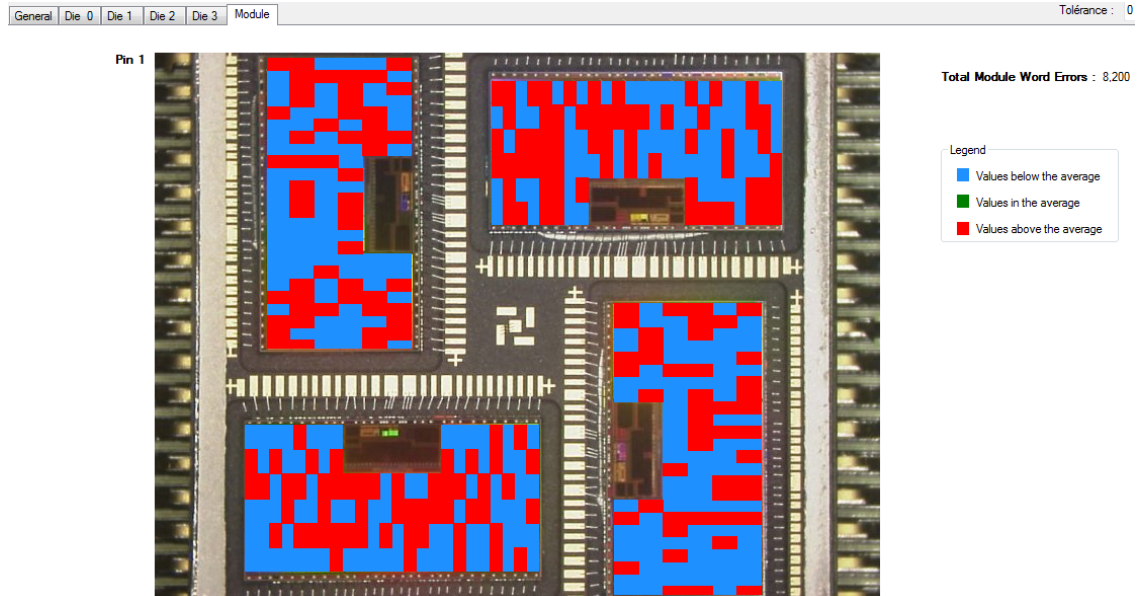


Figure 3.11: ESA SEU Monitor software interface. Beam homogeneity during W45 (2016): in red the SEUs are displayed and they are uniformly spread over the four dies.

Following in Table 3.5, the main measurements are reported for every test week in chronological order. The data refers to the ESA Monitor 1104 or 1330 with or without lid, always tested in M0 above the Montrac. Since three different type of boron carbide boxes were employed, they are indicated as in Table 2.17

In some rows the results in term of SEU, effective POT, time, are the sum of data regarding shorter runs.

- SEU are the number of events obtained considering all the 4 dies of it is composed

Table 3.5: ESA Monitor events, setup and CHARM parameters.

Week	Date code	Setup	Config	SEU	Effective POT	Time [h]	SEU/POT
W41	1104	-	CuOOOO	16506	$1.30 \cdot 10^{16}$	123	$1.27 \cdot 10^{-12}$
W43	1104	4t lid	CuOOOO	211	$3.93 \cdot 10^{14}$	7	$5.36 \cdot 10^{-13}$
W44	1104	4t lid	CuCIIC	1346	$1.38 \cdot 10^{16}$	122	$9.78 \cdot 10^{-14}$
W45	1104	4t lid	CuOOOO	8200	$1.04 \cdot 10^{16}$	109	$7.90 \cdot 10^{-13}$
W45	1104	lid	CuOOOO	39868	$1.04 \cdot 10^{16}$	109	$5.12 \cdot 10^{-12}$
W19	1330	lid	CuCIIC	112	$3.61 \cdot 10^{14}$	6	$3.10 \cdot 10^{-13}$
W19	1330	4t lid	CuCIIC	45	$3.61 \cdot 10^{14}$	6	$1.24 \cdot 10^{-13}$
W19-20	1330	-	CuCIIC	744	$2.45 \cdot 10^{15}$	29	$1.22 \cdot 10^{-12}$
W19-20	1330	f	CuCIIC	131	$1.61 \cdot 10^{15}$	21	$2.43 \cdot 10^{-13}$
W21b	1330	4t	CuOOOO	3220	$3.55 \cdot 10^{15}$	37	$9.06 \cdot 10^{-13}$
W21b	1104	4t	CuOOOO	5445	$7.32 \cdot 10^{15}$	84	$7.44 \cdot 10^{-13}$
W22	1330	-	CuOOOO	5650	$4.81 \cdot 10^{15}$	56	$1.17 \cdot 10^{-12}$
W22	1104	-	CuOOOO	5416	$7.70 \cdot 10^{15}$	85	$7.03 \cdot 10^{-13}$
W23	1330	6t	CuOOOO	2611	$3.47 \cdot 10^{15}$	42	$7.53 \cdot 10^{-13}$
W23	1330	f	CuOOOO	3546	$5.05 \cdot 10^{15}$	87	$7.02 \cdot 10^{-13}$
W24	1330	6t	CuOOOO	3271	$5.93 \cdot 10^{15}$	68	$5.52 \cdot 10^{-13}$

the memory. (From W45 without B4C, only for the ESA Monitor with date code 1104, the data are extracted from 3 dies and the result is given multiplying the SEU number by 3/4.

- Effective POT are the POT related to the SEU events. Therefore, this is the effective value having already ruled out the spills non impacting the target and those arrived when the memory was not active.
- SEU/POT is the ratio between SEU and the relative POT number considering all the 4 dies. This is an important value to Figure out possible memory anomalies: with same configurations and different runs this ratio is supposed to be the same. For instance, we can exclude a priori the two runs over W45, W22 highlighted in red, where for the first the SEU number is too high and for the last they are too low. These abnormal behaviours are considered as outliers and thus not further taken into account in the analysis.

As can be noted, there are different configurations and setup to take into account. The purpose is to retrieve both thn and HEHeq cross sections using the system 3.1 where the known terms are the upset number and the fluences. The latter could be calculated by FLUKA but, since the RadMon measurements highlighted a different value already over the simulated HEH cross section up to a factor 2 and as the thermal neutron fluence is

a complicated estimation (see Table 2.15), the fluences are obtained from the RadMon calibrations 2.16. However the simulations showed that the HEHeq are not affected using the boron carbide, hence the cross sections using the differential approach are calculated considering the case:

- $\Phi_{HEHeq} = \Phi_{HEHeq}^{B4C}$ where the former fluence is measured by the RadMon without boron carbide and reported in Table 3.6, in comparison with the FLUKA simulation values (further details in Table 2.15). The fact that the simulations present overestimations up to a factor 2.5 (CP-CIIC) is under investigation, and it could be related to the different intermediate-energy neutron response of the device.

Table 3.6: RadMon HEHeq reference fluence for the ESA Monitor calculations.

no B4C	CuOOOO	CuCIIC
HEHeq [cm^{-2}/POT]	$1.53 \cdot 10^{-6}$	$1.09 \cdot 10^{-7}$
HEHeq(sim) [cm^{-2}/POT]	$2.36 \cdot 10^{-6}$	$2.69 \cdot 10^{-7}$

The results are respectively outlined in Table 3.7. Each row represents a differential measurement extracted from Table 3.5. Therefore, the measurements required either two memories employed in the same week or one memory tested for at least two weeks (column "week").

Table 3.7: ESA Monitor HEHeq and thermal neutron cross sections retrieved by applying the differential approach. In bold the weeks of tests conducted during 2016.

Week	Date code	Setup	Config	HEHeq [cm^2/bit]	%HEH	Thn [cm^2/bit]	%Thn
41-43-45	1104	4t lid	CuOOOO	$2.54 \cdot 10^{-14}$	36.3	$2.76 \cdot 10^{-15}$	61.6
21-22	1330	4t	CuOOOO	$3.12 \cdot 10^{-14}$	35.3	$1.67 \cdot 10^{-15}$	108.7
21- 41	1104	4t	CuOOOO	$2.36 \cdot 10^{-14}$	36.7	$2.97 \cdot 10^{-15}$	56.1
22-23	1330	6t	CuOOOO	$2.88 \cdot 10^{-14}$	28.1	$1.94 \cdot 10^{-15}$	72.7
22-24	1330	6t	CuOOOO	$2.07 \cdot 10^{-14}$	28.1	$2.87 \cdot 10^{-15}$	43.0
22-23	1330	f	CuOOOO	$2.67 \cdot 10^{-14}$	28.2	$2.19 \cdot 10^{-15}$	62.2
19	1330	4t lid	CuCIIC	$3.83 \cdot 10^{-14}$	51.1	$3.86 \cdot 10^{-15}$	38.6
19-20	1330	f	CuCIIC	$9.33 \cdot 10^{-15}$	184.01	$4.64 \cdot 10^{-15}$	35.83

- HEHeq is retrieved multiplying the week's POT from Table 3.5 by the respective RadMon fluence (Table 3.6) and dividing them by the total ESA Monitor bit number.

- Thn instead, is calculated considering each thermal neutron fluence measured from the RadMon with the different boron carbide boxes from Table 2.16

Regarding the cross section results, they are quite compatible with each other except the cases in red. However, although these latter HEHeq cross sections deviate too much from the standard values, the thermal neutron cross section can be considered acceptable because they are independent from the HEHeq fluence. During W22-W24 for instance, a lower SEU/POT was measured (see Table 3.5). This fact is likely due to the combination of memory operation plus the HEH fluence contribution but did not affected the thermal neutron fluence and events generated by these, otherwise the thermal cross section would have been mismatched.

Considering negligible the differences between date code 1104 and 1330 and those introduced by the lid, a unique cross section value can be extracted for the two facility configurations averaging the values of Table 3.7 and applying the uncertainty propagation formula for what concern the relative error. They are presented in Table 3.8. It has to be noted that with the full shielding both HEHeq fluences are rather different each other, and the final value is calculated averaging them.

Table 3.8: ESA SEU Monitor, summary cross sections considering all the valid runs.

Config	HEHeq [cm^2/bit]	%HEH	Thn [cm^2/bit]	%Thn
CuOOOO	$2.60 \cdot 10^{-14}$	32.1	$2.40 \cdot 10^{-15}$	67.4
CuCIIC	$2.38 \cdot 10^{-14}$	117.6	$4.25 \cdot 10^{-15}$	37.2

3.4 SEL results

From W37 to W45 (2016) and from W19 to W24 (2017) four different type of memories were tested in M0 at the CHARM facility: Alliance, Brilliance, ISSI and Lyontek. Only the Alliance was placed in G0 position attached to the grid on the wall due to its low sensitivity. Although G0 has a lower R-factor compared with that of M0, its HEHeq fluence is higher more than a factor 2 as previously showed in 2.10, so that it was possible to obtain a reasonable statistic. All the other boards were placed in M0 position directly above the Montrac or inside the boron carbide cube always above this support. The results will be showed by referring to what type of boron carbide box was employed: 4 tiles cube, 6 tiles cube or flexible box. The experimental data are retrieved from the laptop(s) in the control room that was running PS Control written in LabVIEW. This

software as described above permits to set up voltage, maximum current and current threshold for the latch-up and each memory has its own parameters (see Table 3.3) and finally it saves in an output file at what time the SEL occurs.

Following, the complete table with the data for retrieving the final HEH cross sections. The results are grouped by memory type, listed in order of same operating conditions. Weeks regarding the tests during 2016 are written in bold. The test position was M0 at CHARM above the montrac for all the tests except for the Alliance witch was placed in G0. The column S means boron carbide setup (4t=4 tiles, 6t=6 tiles, f=flexible box) and the next one refers to the voltage applied on the board constituted by 8 chips except for the "Brilliance1x" that was composed of one single chip. The boards were powered to 3.3 V and in the case of Brilliance and Lyontek also to 5.5V. In the latter case the cross section increases because the higher electric fields inside the MOSFET structure helps parasitic transistors to turn on.

- POT with target, like in the TIMBER data tables they are the protons that collide against the target inside the chamber and produce a field of radiation over the memories.
- % POT is the difference between the effective POT (that generate SELs) and the integrated POT with target (see also the Effective HEH fluence explanation below). This values is necessarily proportional to the SEL number and note that this percentage is not the same of the mixed-field radiation calculation and monitoring in 2.5.2. The same percentage can be seen between the fluence with target and the effective HEH fluence as POT and fluence are directly proportional.
- HEH with target [cm^{-2}] is the HEH fluence obtained multiplied the total POT by the HEH flux [cm^{-2}/POT] remembering that this value changes with the shielding configuration and, for a better understanding the fluence column has the same color of the HEH configuration on the bottom.
- Effective HEH [cm^{-2}] is the HEH effective fluence.

When an SEL occurs, it is unknown the amount of POT that are produced from the spill because the latter lasts 350 ms and in this range of time, the latch-up may occur at the beginning or at the end of the spill time. Therefore, statistically half of the POT in this dead time have to be removed from the total POT.

$$\Phi_{HEH}^{eff}[cm^{-2}] = \Phi_{target} - \frac{POT_{mean}^{spill} \cdot \Phi_{HEH}}{2} \cdot N_{SEL} \quad (3.16)$$

Table 3.9: SEL test parameters with different boron carbide setup. *Alliance was tested in G0 position at CHARM, whereas all the other memories above M0.

Week	Config	Memory	S	[V]	POT/ spill	SEL	POT with target	POT %	SEL/ POT
W37-38-39	OOOO	Alliance*	-	3.3	$3.2 \cdot 10^{11}$	45	$2.36 \cdot 10^{16}$	0.0	$1.90 \cdot 10^{-15}$
W41	OOOO	ISSI	-	3.3	$4.1 \cdot 10^{11}$	2772	$1.29 \cdot 10^{16}$	-4.4	$2.15 \cdot 10^{-13}$
W23	OOOO	ISSI	-	3.3	$3.5 \cdot 10^{11}$	1962	$8.41 \cdot 10^{15}$	-4.1	$2.33 \cdot 10^{-13}$
W42	OOOO	ISSI	4t	3.3	$4.0 \cdot 10^{11}$	3005	$1.20 \cdot 10^{16}$	-5.0	$2.50 \cdot 10^{-13}$
W43	OOOO	ISSI	4t	3.3	$4.0 \cdot 10^{11}$	2215	$1.24 \cdot 10^{16}$	-3.6	$1.79 \cdot 10^{-13}$
W24	OOOO	ISSI	6t	3.3	$3.9 \cdot 10^{11}$	2479	$1.21 \cdot 10^{16}$	-4.0	$2.05 \cdot 10^{-13}$
W44	CIIC	ISSI	4t	3.3	$3.9 \cdot 10^{11}$	385	$1.37 \cdot 10^{16}$	-0.5	$2.81 \cdot 10^{-14}$
W44	CIIC	ISSI	-	3.3	$3.9 \cdot 10^{11}$	488	$1.37 \cdot 10^{16}$	-0.7	$3.56 \cdot 10^{-14}$
W41	OOOO	Brilliance	-	3.3	$4.1 \cdot 10^{11}$	3711	$1.29 \cdot 10^{16}$	-5.8	$2.87 \cdot 10^{-13}$
W23	OOOO	Brilliance	-	3.3	$3.0 \cdot 10^{11}$	1961	$7.11 \cdot 10^{15}$	-4.1	$2.76 \cdot 10^{-13}$
W23	OOOO	Brilliance	-	5.5	$5.5 \cdot 10^{10}$	424	$1.30 \cdot 10^{15}$	-0.9	$3.27 \cdot 10^{-13}$
W42	OOOO	Brilliance	4t	3.3	$4.0 \cdot 10^{11}$	3227	$1.20 \cdot 10^{16}$	-5.3	$2.69 \cdot 10^{-13}$
W45	OOOO	Brilliance	4t	3.3	$3.8 \cdot 10^{11}$	2597	$1.03 \cdot 10^{16}$	-4.7	$2.51 \cdot 10^{-13}$
W24	OOOO	Brilliance	6t	3.3	$2.0 \cdot 10^{11}$	1324	$6.19 \cdot 10^{15}$	-2.1	$2.14 \cdot 10^{-13}$
W24	OOOO	Brilliance	6t	5.5	$1.9 \cdot 10^{11}$	1557	$5.92 \cdot 10^{15}$	-2.5	$2.63 \cdot 10^{-13}$
W22	OOOO	Brilliance1x	-	3.3	$1.5 \cdot 10^{11}$	1026	$3.58 \cdot 10^{15}$	-2.1	$2.87 \cdot 10^{-13}$
W22	OOOO	Brilliance1x	-	5.5	$2.6 \cdot 10^{11}$	3855	$6.39 \cdot 10^{15}$	-7.9	$6.03 \cdot 10^{-13}$
W22	OOOO	Lyontek	-	3.3	$1.5 \cdot 10^{11}$	812	$3.58 \cdot 10^{15}$	-1.7	$2.27 \cdot 10^{-13}$
W22	OOOO	Lyontek	-	5.5	$2.6 \cdot 10^{11}$	2090	$6.39 \cdot 10^{15}$	-4.3	$3.27 \cdot 10^{-13}$
W43	OOOO	Lyontek	4t	3.3	$4.0 \cdot 10^{11}$	2264	$1.24 \cdot 10^{16}$	-3.6	$1.83 \cdot 10^{-13}$
W45	OOOO	Lyontek	4t	3.3	$3.8 \cdot 10^{11}$	2006	$1.03 \cdot 10^{16}$	-3.6	$1.94 \cdot 10^{-13}$
W43	OOOO	Lyontek	4t	5.5	$4.0 \cdot 10^{11}$	685	$1.24 \cdot 10^{16}$	-1.1	$5.53 \cdot 10^{-14}$
W21	OOOO	Lyontek	4t	5.5	$3.3 \cdot 10^{11}$	2618	$8.61 \cdot 10^{15}$	-5.0	$3.04 \cdot 10^{-13}$

Table 3.10: (continues from the previous table) SEL cross sections results.

Week	Memory	S	[V]	HEH with target [cm^{-2}]	HEH [cm^{-2}]	Effective HEH/POT [cm^{-2} /POT]	HEH [cm^2]
W37-38-39	Alliance*	-	3.3	$1.11 \cdot 10^{11}$	$1.11 \cdot 10^{11}$	$4.70 \cdot 10^{-6}$	$5.06 \cdot 10^{-11}$
W41	ISSI	-	3.3	$2.21 \cdot 10^{10}$	$2.12 \cdot 10^{10}$	$1.71 \cdot 10^{-6}$	$1.64 \cdot 10^{-8}$
W23	ISSI	-	3.3	$1.44 \cdot 10^{10}$	$1.38 \cdot 10^{10}$	$1.71 \cdot 10^{-6}$	$1.78 \cdot 10^{-8}$
W42	ISSI	4t	3.3	$2.05 \cdot 10^{10}$	$1.95 \cdot 10^{10}$	$1.71 \cdot 10^{-6}$	$1.92 \cdot 10^{-8}$
W43	ISSI	4t	3.3	$2.12 \cdot 10^{10}$	$2.12 \cdot 10^{10}$	$1.78 \cdot 10^{-6}$	$1.30 \cdot 10^{-8}$
W24	ISSI	6t	3.3	$2.07 \cdot 10^{10}$	$1.98 \cdot 10^{10}$	$1.70 \cdot 10^{-6}$	$1.57 \cdot 10^{-8}$
W44	ISSI	4t	3.3	$2.92 \cdot 10^9$	$2.92 \cdot 10^9$	$2.14 \cdot 10^{-7}$	$1.65 \cdot 10^{-8}$
W44	ISSI	-	3.3	$2.92 \cdot 10^9$	$2.92 \cdot 10^9$	$2.14 \cdot 10^{-7}$	$2.09 \cdot 10^{-8}$
W41	Brilliance	-	3.3	$2.21 \cdot 10^{10}$	$2.08 \cdot 10^{10}$	$1.71 \cdot 10^{-6}$	$2.23 \cdot 10^{-8}$
W23	Brilliance	-	3.3	$1.22 \cdot 10^{10}$	$1.17 \cdot 10^{10}$	$1.71 \cdot 10^{-6}$	$2.10 \cdot 10^{-8}$
W23	Brilliance	-	5.5	$2.22 \cdot 10^9$	$2.20 \cdot 10^9$	$1.71 \cdot 10^{-6}$	$2.40 \cdot 10^{-8}$
W42	Brilliance	4t	3.3	$2.05 \cdot 10^{10}$	$1.94 \cdot 10^{10}$	$1.71 \cdot 10^{-6}$	$2.07 \cdot 10^{-8}$
W45	Brilliance	4t	3.3	$1.77 \cdot 10^{10}$	$1.68 \cdot 10^{10}$	$1.70 \cdot 10^{-6}$	$1.94 \cdot 10^{-8}$
W24	Brilliance	6t	3.3	$1.06 \cdot 10^{10}$	$1.04 \cdot 10^{10}$	$1.71 \cdot 10^{-6}$	$1.60 \cdot 10^{-8}$
W24	Brilliance	6t	5.5	$1.01 \cdot 10^{10}$	$9.73 \cdot 10^9$	$1.68 \cdot 10^{-6}$	$2.00 \cdot 10^{-8}$
W22	Brilliance1x	-	3.3	$6.13 \cdot 10^9$	$6.00 \cdot 10^9$	$1.71 \cdot 10^{-6}$	$1.71 \cdot 10^{-7}$
W22	Brilliance1x	-	5.5	$1.09 \cdot 10^{10}$	$1.01 \cdot 10^{10}$	$1.71 \cdot 10^{-6}$	$3.83 \cdot 10^{-7}$
W22	Lyontek	-	3.3	$6.13 \cdot 10^9$	$6.03 \cdot 10^9$	$1.71 \cdot 10^{-6}$	$1.68 \cdot 10^{-8}$
W22	Lyontek	-	5.5	$1.09 \cdot 10^{10}$	$1.05 \cdot 10^{10}$	$1.71 \cdot 10^{-6}$	$2.49 \cdot 10^{-8}$
W43	Lyontek	4t	3.3	$2.12 \cdot 10^{10}$	$2.09 \cdot 10^{10}$	$1.75 \cdot 10^{-6}$	$1.35 \cdot 10^{-8}$
W45	Lyontek	4t	3.3	$1.77 \cdot 10^{10}$	$1.70 \cdot 10^{10}$	$1.70 \cdot 10^{-6}$	$1.48 \cdot 10^{-8}$
W43	Lyontek	4t	5.5	$2.12 \cdot 10^{10}$	$3.36 \cdot 10^8$	$2.74 \cdot 10^{-8}$	$2.55 \cdot 10^{-7}$
W21	Lyontek	4t	5.5	$1.48 \cdot 10^{10}$	$1.40 \cdot 10^{10}$	$1.71 \cdot 10^{-6}$	$2.33 \cdot 10^{-8}$

Where Φ_{HEH} is measured in $[cm^{-2}/POT]$ and it's a FLUKA simulated value. The POT mean of one spill are the protons carried by one spill and it was derived considering the POT average during all the week run albeit in some weeks, not all the POT in the fluence calculation were used (for instance due to the target not in position).

- HEH/POT $[cm^{-2}/POT]$ is the ratio between the previous fluence value of Φ_{HEH}^{eff} and the total number of effective POT.
- HEH cross section $[cm^2]$ is the ratio between the total number of SEL and the Φ_{HEH}^{eff} . As in one board are installed 8 chips, this result was divided by 8 for display the cross section per chip.

From the previous tables the data regarding the same memories exposed to the same operating conditions are merged, adding together SEL number and POT with target, as the week was a longer one and the results are presented in Table 3.11. The Lyontek data powered to 5.5 V on W43 is not considered reliable because the related ratio effective HEH/POT is anomalous, whereas that value is basically stable on the other runs (note that although the HEH fluence is that from simulation, this ratio is considering the effective HEH fluence, therefore it is not always a constant value).

From Table 3.11, the information concerning the cross section variability by using the boron carbide and changing the power voltage are extracted and respectively presented in Table 3.12 and 3.13.

First of all it is to be noted the fact that, for every memory type the cross section retrieved covering it with the boron carbide is somewhat lower with respect to that in normal conditions. In addition, these data refers to the cases where this effect is more evident, therefore with the 6 tiles or the flexible boron carbide box. This observation can be explained in two ways:

- the memory is slightly sensitive to the thermal neutrons
- a small amount of measured SEL is due to that part of spectra removed by the boron carbide that regards the intermediate energy neutrons.

Looking at the ratio between the two cross sections this reduction can be quantified:

- ISSI and Lyontek memory did not show to be sensitive to thermal neutrons within the component to component variability precisely because the reduction of cross section is not beyond 20%.

Table 3.11: SEL summary cross section results by varying the boron carbide setup and voltage.

Week	Config	Memory	S	[V]	HEH [cm^2]
W37-38-39	CuOOOO	Alliance*	-	3.3	$5.06 \cdot 10^{-11}$
W41-23	CuOOOO	ISSI	-	3.3	$1.69 \cdot 10^{-8}$
W42-43	CuOOOO	ISSI	4t	3.3	$1.63 \cdot 10^{-8}$
W24	CuOOOO	ISSI	6t	3.3	$1.57 \cdot 10^{-8}$
W44	CuCHC	ISSI	4t	3.3	$1.65 \cdot 10^{-8}$
W44	CuCHC	ISSI	-	3.3	$2.09 \cdot 10^{-8}$
W41-23	CuOOOO	Brilliance	-	3.3	$2.18 \cdot 10^{-8}$
W23	CuOOOO	Brilliance	-	5.5	$2.40 \cdot 10^{-8}$
W42-45	CuOOOO	Brilliance	4t	3.3	$2.00 \cdot 10^{-8}$
W24	CuOOOO	Brilliance	6t	3.3	$1.60 \cdot 10^{-8}$
W24	CuOOOO	Brilliance	6t	5.5	$2.00 \cdot 10^{-8}$
W22	CuOOOO	Brilliance1x	-	3.3	$1.71 \cdot 10^{-7}$
W22	CuOOOO	Brilliance1x	-	5.5	$3.83 \cdot 10^{-7}$
W22	CuOOOO	Lyontek	-	3.3	$1.68 \cdot 10^{-8}$
W22	CuOOOO	Lyontek	-	5.5	$2.49 \cdot 10^{-8}$
W43-45	CuOOOO	Lyontek	4t	3.3	$1.42 \cdot 10^{-8}$
W21	CuOOOO	Lyontek	4t	5.5	$2.33 \cdot 10^{-8}$

- Regarding the Brilliance instead, the ratio is higher up to 36.7% of difference. The conclusion is that Brilliance memory might be slightly sensitive to thermal neutrons, but it could still be statistically compatible since at 5.5 V the difference is within 20%.

The voltage sensitivity in Table 3.13, outlines that higher the voltage and higher the cross sections especially for the single Brilliance1x where the sensitivity increased more than a factor 2.

Table 3.12: SEL cross sections difference by employing the boron carbide.

Memory	Voltage [V]	$\sigma_{HEH}[cm^2]$		$\frac{\sigma_{HEH}}{\sigma_{HEH}(B4C)}$	%
		no B4C	B4C		
ISSI	3.3	$1.69 \cdot 10^{-8}$	$1.57 \cdot 10^{-8}$	1.08	-7.9
Brilliance	3.3	$2.18 \cdot 10^{-8}$	$1.60 \cdot 10^{-8}$	1.37	-36.7
Brilliance	5.5	$2.40 \cdot 10^{-8}$	$2.00 \cdot 10^{-8}$	1.20	-20.2
Lyontek	3.3	$1.68 \cdot 10^{-8}$	$1.42 \cdot 10^{-8}$	1.18	-18.4
Lyontek	5.5	$2.49 \cdot 10^{-8}$	$2.33 \cdot 10^{-8}$	1.07	-6.9

Table 3.13: SEL cross sections sensitivity by changing the voltage.

Memory	$\sigma_{HEH}[cm^2]$		$\sigma_{5.5}/\sigma_{3.3}$
	3.3 [V]	5.5 [V]	
Brilliance1x	$1.71 \cdot 10^{-7}$	$3.83 \cdot 10^{-7}$	2.24
Brilliance	$2.18 \cdot 10^{-8}$	$2.40 \cdot 10^{-8}$	1.10
Lyontek	$1.68 \cdot 10^{-8}$	$2.49 \cdot 10^{-8}$	1.48

3.4.1 Events and fluence

As regards all the performed tests on memories, the latch-up number increased proportionally with the relative fluence with no saturation as shown in Figure 3.12. An abnormal behaviour was observed only during W42 on the Brilliance covered by boron carbide. Until a certain fluence the slope was unique but after that point the angular coefficient changed decreasing of about 4% (Figure 3.13), perhaps due to the activation of another mechanism. Redoing the experiment during W45 with the same identical parameters of the memory and facility there were only one slops similar to that of Figure 3.12.

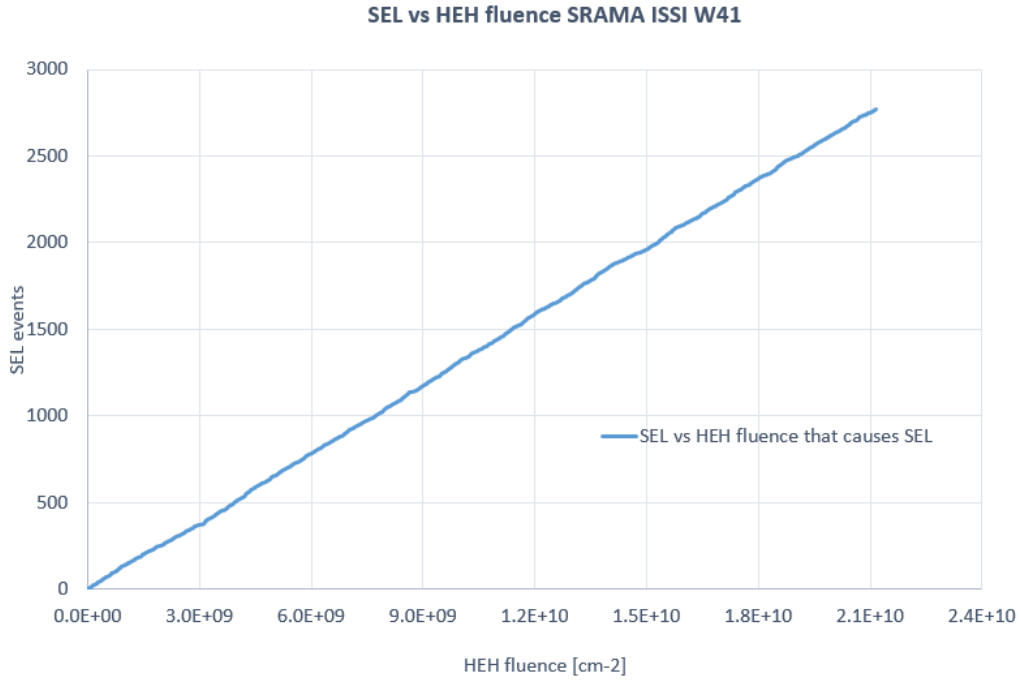


Figure 3.12: Latch-up events as a function of the HEH fluence.

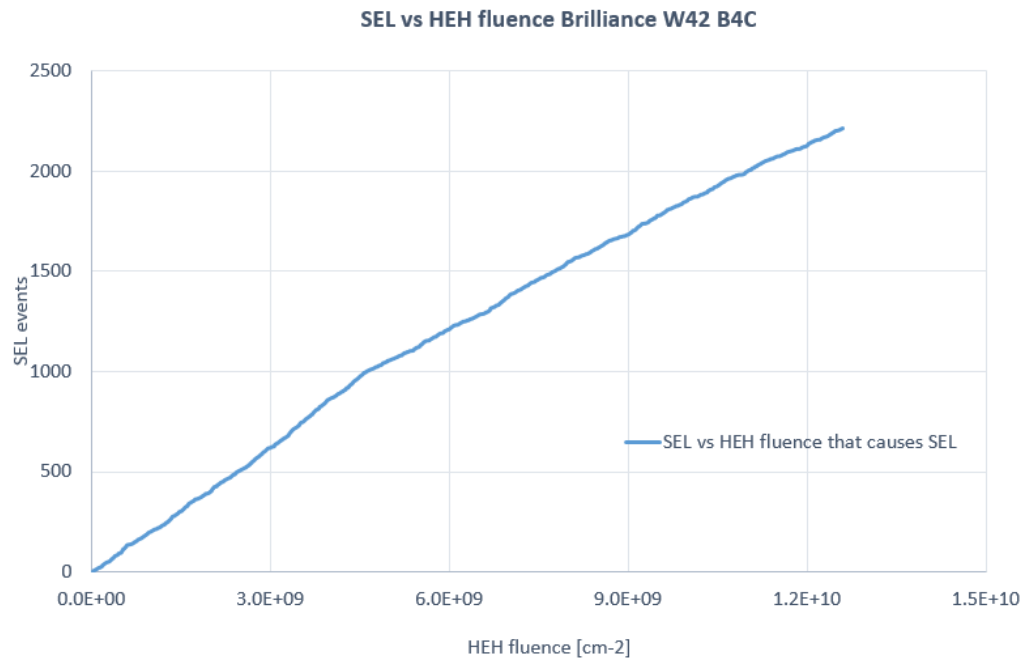


Figure 3.13: SEL vs HEH fluence of the Brilliance memory in W42, Cu-O000 configuration.

Chapter 4

Radiation neutron tests in other facilities

The memories studied in the neutron-dominated position at CHARM were tested also during a test campaign conducted in Grenoble (France) in two facilities: ILL a thermal neutron reactor and LPSC a 14 MeV neutron source machine. The campaign aimed to verify the compatibility of results obtained at CHARM against those of mono-energetic facilities. The facilities description (further details can be found in [13]), test setup and results are presented in this chapter. Moreover, an americium-beryllium (Am-Be) neutron source was employed at CERN with the purpose of assessing the possibility of performing SEU tests. For the latter a preliminary phase of calibration was carried out to continue with a SEU test on a Cypress memory.

The results are gathered on the basis of the facility and the type of Single Event Effect (Upset or Latch-up). For both SEL and SEU experiments, when less than 50 event were counted, the upper limit of the cross section was calculated using a Poisson distribution with 95% of confidence level, as reported in [14]. These values are shown in Table 4.1.

N	95% Limits	
	lower	upper
0	0.0	3.7
1	0.1	5.6
2	0.2	7.2
3	0.6	8.8
4	1.0	10.2
5	1.6	11.7
6	2.2	13.1
7	2.8	14.4
8	3.4	15.8
9	4.0	17.1
10	4.7	18.4
11	5.4	19.7
12	6.2	21.0
13	6.9	22.3
14	7.7	23.5
15	8.4	24.8
16	9.4	26.0

N	95% Limits	
	lower	upper
17	9.9	27.2
18	10.7	28.4
19	11.5	29.6
20	12.2	30.8
21	13.0	32.0
22	13.8	33.2
23	14.6	34.4
24	15.4	35.6
25	16.2	36.8
26	17.0	38.0
27	17.8	39.2
28	18.6	40.4
29	19.4	41.6
30	20.2	42.8
31	21.0	44.0
32	21.8	45.1
33	22.7	46.3

N	95% Limits	
	lower	upper
34	23.5	47.5
35	24.3	48.7
36	25.1	49.8
37	26.0	51.0
38	26.8	52.2
39	27.7	53.3
40	28.6	54.5
41	29.4	55.6
42	30.3	56.8
43	31.1	57.9
44	32.0	59.0
45	32.8	60.2
46	33.6	61.3
47	34.5	62.5
48	35.3	63.6
49	36.1	64.8
50	37.0	65.9

Table 4.1: Poisson distribution margin limits with 95% of confidence margin.

The cross section are normalized per bit or chip for SEU and SEL respectively:

$$\sigma = \frac{N_{SEU}}{\Phi \cdot n_{\text{bit or chip}}} \left[\frac{\text{cm}^2}{\text{bit or chip}} \right] \quad (4.1)$$

4.0.1 Tested memories and experimental setup

Table 4.2 shows the memory boards employed during the tests, as well as the respective test facility and measured events.

Table 4.2: Tested SRAM memory at ILL,LPSC and The Americium-Beryllium (AmBe) source. The Brilliance and Lyontek memories have been tested at 3.3 and 5.5 V. Except for the Brilliance1x, the other SEL memories refer to a board equipped with 8 memories.

Memory	SEE	Facility	Date code	Part reference	Tech	Size Mbit
ESA M.	SEU	LPSC-AmBe	1104	AT68166F	0.25 μm	16
		LPSC-ILL-AmBe	1330	AT68166H-YM20-E		
Cypress	SEU	ILL-AmBe	1437	CY62157EV30LL-45ZSXI	90 nm	8
		LPSC-ILL-AmBe	1443			
ISSI	SEL	LPSC	1246-1303	IS61LV5128AL-10TLI	0.18 μm	4
Brilliance	SEL	LPSC-ILL	12094	BS62LV1600EIP55	0.18 μm	16
Brilliance1x	SEL	LPSC	11254		0.18 μm	16
Lyontek	SEL	LPSC	1251	LY62W20488ML-55LL	0.18 μm	16

Memory descriptions and test setup were already explained in 3.1.2 for most of them, except what concern the Cypress that is explained below.

Cypress Memory Two boards mounting a Cypress memory were tested all three facilities to evaluate the SEU sensitivity (Figure 4.1). The reading of the memory was performed with a serial data communication by means of a USB-Ethernet-USB cable and the Docklight software for the communication with the laptop: this software allows to read the memory in real-time every second as can be seen in Figure 4.2, where the hexadecimal values are the upsets referred to each second. The output data are the SEU number (in this case expressed in hexadecimal format) occurred in 1 second in the memory, so that every second the memory was read and the SEU counter resets. The final SEU number is obtained summing all the events.

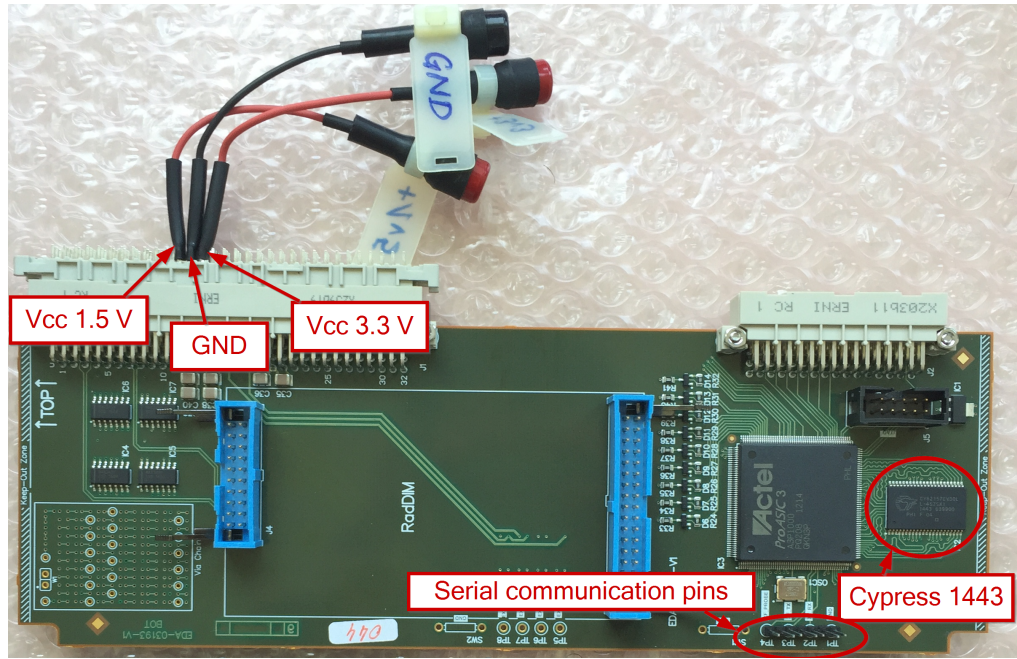


Figure 4.1: SRAM Cypress CY62157EV30LL-45ZSXI board.

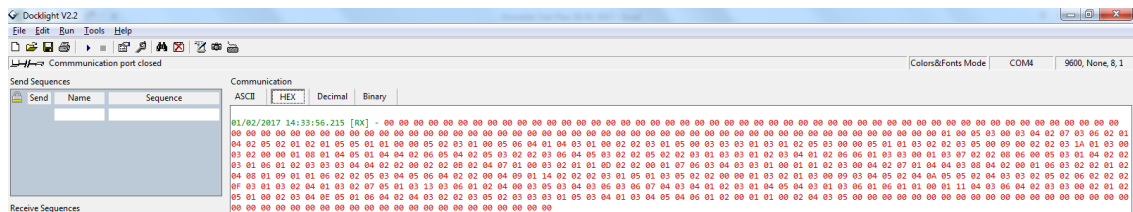


Figure 4.2: Docklight software for the memory reading. The transmission of the data is conducted by means of a serial data communication.

4.0.2 Flux and homogeneity cross-calibration with the ESA Monitor

Before conducting the tests, an accurate cross-calibration of the facilities was performed to assess the homogeneity (and centering of the beam as regards LPSC and ILL). The general formula to retrieve the flux is the follows:

$$\varphi = \frac{N_{SEU}}{\Delta t \cdot \sigma_{ref} \cdot n_{bit}} \left[\frac{n}{cm^2 s} \right] \quad (4.2)$$

4.1 Thermal neutrons: ILL

The Institut Laue Langevin (ILL), is consisting of a nuclear reactor with a total thermal power of 58 MW. The fuel element is highly enriched uranium, cooled and moderated with heavy water (D₂O) to produce the most intense neutron flux in the world, namely $1.5 \cdot 10^{15} \text{ cm}^{-2} \cdot \text{s}^{-1}$. Neutrons are produced in the reactor from the fission reactions of the Uranium nuclei: prompt neutrons have a very high-energy corresponding 20,000 km/s. They are slowed down to thermal energy (2.2 km/s) by the heavy water in order to be able to produce new fissions and to maintain the reaction chain self-consistent as well as to provide thermal neutrons beams to all the experiments.

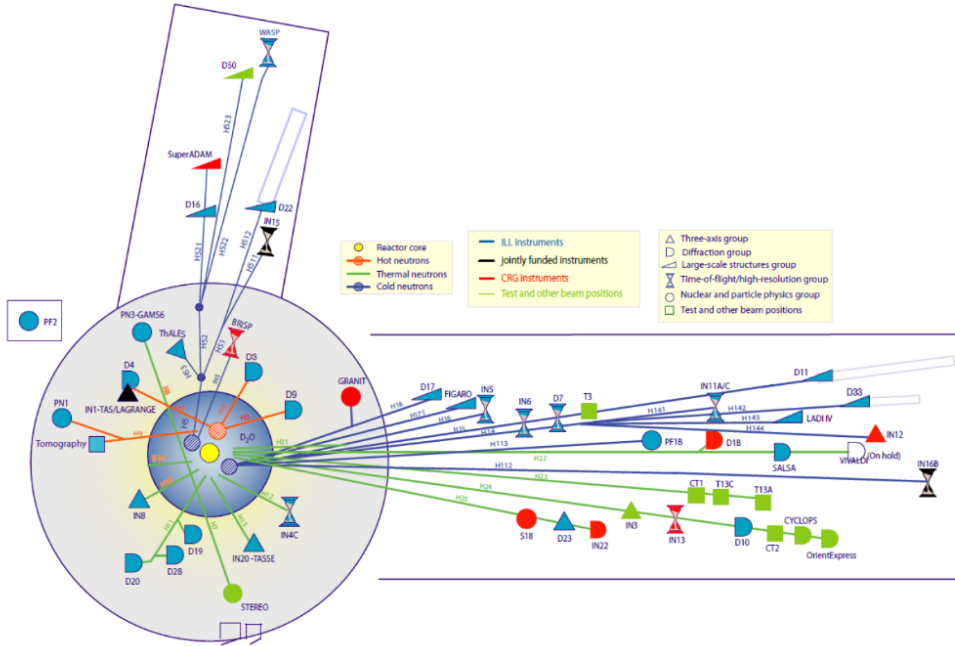


Figure 4.3: Experimental areas available at ILL.

The neutrons are then extracted through 20 channels extended by neutron guides providing neutron beam over more than 40 experimental areas (Figure 4.3). One of these area is the D50 instrument, where we performed our tests. The neutrons available on D50

are produced by the ILL horizontal cold source (thermal neutrons moderated by liquid deuterium at 20 °K) and transmitted along a 100 m long neutron-guide. The captured flux (i.e. equivalent flux of 25 meV neutron) delivered on D50 is adjustable from 0 to $1.0 \cdot 10^{10} \text{ cm}^{-2} \cdot \text{s}^{-1}$. The neutron spot size may be easily adapted for local irradiation (1 mm²) to global irradiation of homogeneous square section of about 5000 mm² by means of motorised borated carbon (B4C) slits. The typical neutron spectrum available at D50 is reported in Figure 4.4.

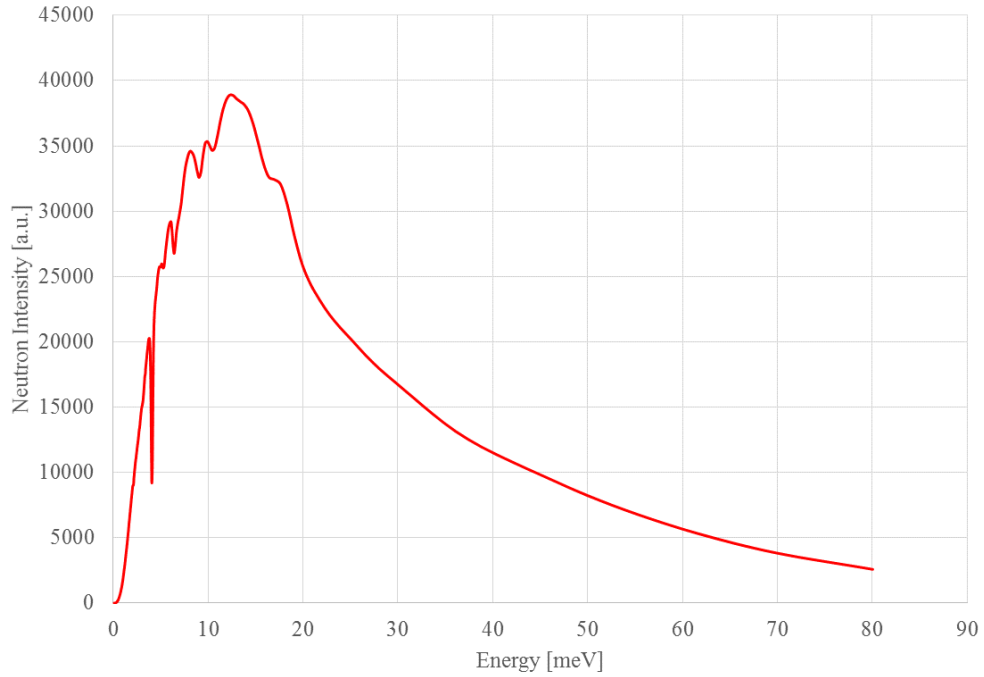


Figure 4.4: ILL-D50 neutron spectrum.

The neutron flux is controlled with dedicated ^3He detector and it is periodically appraised by the activation of 5 gold foils with a diameter of 10 mm. For the tests, the reference value of $1.37 \cdot 10^8 \text{ cm}^{-2} \cdot \text{s}^{-1}$ was used referred to the center of one gold foil as shown below.

ILL calibration

Similarly to LPSC, the same ESA Monitor type was used at ILL D50 instrument for the calibration and homogeneity check before testing other memories. We mounted the ESA Monitor on a dedicated support which was moved in the left-right direction through the system described in Figure 4.5.

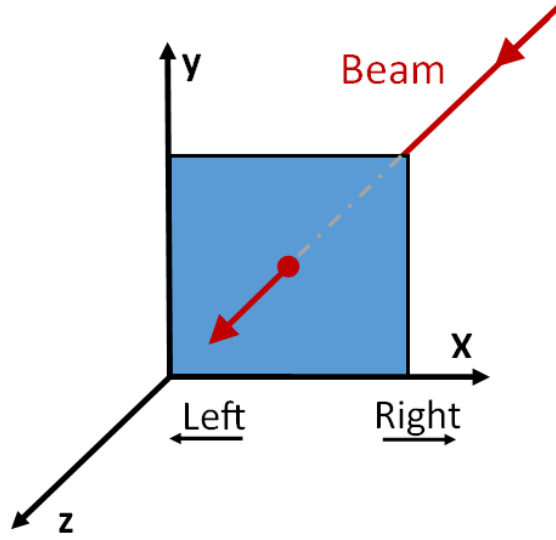


Figure 4.5: Axis system reference (ILL).

For all the tests the AT68166H-YM20-E reference memory was employed without the plastic lid. The measurements were performed in 11 positions by moving the support to the left, right, up and down; the distance between the memory and the neutron nozzle was fixed. Every run lasted 'Test time' and the thermal neutrons flux was that provided from the facility as described before. Table 4.3 reports the SEU results at different distances from the center. Since the ESA Monitor has a different area (a square of 20 x 20 mm) with respect to that of the foil calibration (a circle of 10 mm diameter), for geometric considerations the flux that crosses the ESA Monitor surface is considered to be the same quantity that passes through all the five foils. Therefore it is calculated as the arithmetic mean of the five calibration fluxes and it is equal to $1.28 \cdot 10^8 \text{ cm}^{-2} \cdot \text{s}^{-1}$. To compute the fluxes in all the other positions, the reference flux was scaled with the SEU number and measurement time of the test 1.

$$\varphi_i = 1.28E8 \cdot \frac{SEU_i}{SEU_{ref}} \cdot \frac{\Delta t_{ref}}{\Delta t_i} \quad \left[\frac{n}{\text{cm}^2 \cdot \text{s}} \right] \quad (4.3)$$

Fluxes and cross section are calculated in table 4.3.

In the test number 1 the ESA Monitor active area was placed with respect to the reference system of the facility (see Figure 4.5), with the beam centered on the middle of the 4 dies. As shown in Figure 4.6, the beam was quite inhomogeneous given that the dies 2 and 3 recorded much more upset with respect to the dies 0 and 1.

Table 4.3: ESA SEU Monitor AT68166H-YM20-E 1330 with no lid measurements in different positions. c = center and left or right are referred as if the observer is seeing the upcoming beam in front of him (Figure 4.5).

Test	Position [mm]	Test time [s]	(E.M.) Flux 1 [n/cm ² /s]	SEU	σ_1 [cm ² /bit]
1	c	300	$1.28 \cdot 10^8$	2907	$4.51 \cdot 10^{-15}$
2	c + 3 mm left	300	$1.26 \cdot 10^8$	2858	
3	c + 3 mm left	300	$1.24 \cdot 10^8$	2808	
4	c + 13 mm left	180	$1.22 \cdot 10^8$	1666	
5	c + 23 mm left	180	$1.02 \cdot 10^8$	1392	
6	c + 33 mm left	180	$4.35 \cdot 10^7$	593	
7	c + 43 mm left	181	$5.91 \cdot 10^6$	81	
8	c + 7 mm right	180	$1.21 \cdot 10^8$	1645	
9	c + 17 mm right	180	$1.07 \cdot 10^8$	1460	
10	c + 27 mm right	180	$6.88 \cdot 10^7$	937	
11	c + 21 mm up	181	$1.23 \cdot 10^8$	1687	
12	c + 21 mm down	186	$5.62 \cdot 10^7$	792	

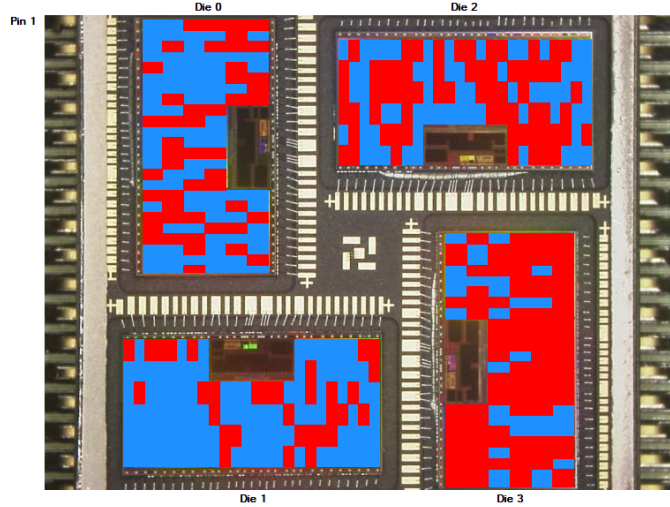


Figure 4.6: ESA Monitor events for the centered run: in red are indicated the SEU.

All the other measurements were done considering the center at 3 mm toward the left (from the test 2 to the test 10). The ratio between the SEU of die3 and those of the die0 is expected to be close to 1 for a perfect homogeneity and as shown in Table 4.4, the position at 23 mm to the left from the center comes closest to the SEU symmetry on the dies. A quick overview of the left shifts (test number 4, 5, 6, 7) is reported in Figure 4.7 where the best homogeneity was found for the test 5 at 23 mm toward the left, and after this position the memory started to exit from the beam area.

Table 4.4: ESA Monitor SEU of each die.

Test	Position [mm]	die0	die1	die2	die3	die3/die0	die2/die1
1	c	637	538	707	1025	1.61	1.31
2	c + 3 mm left	624	613	696	925	1.48	1.14
3	c + 3 mm left	625	569	691	923	1.48	1.21
4	c + 13 mm left	359	380	374	553	1.54	0.98
5	c + 23 mm left	352	296	314	430	1.22	1.06

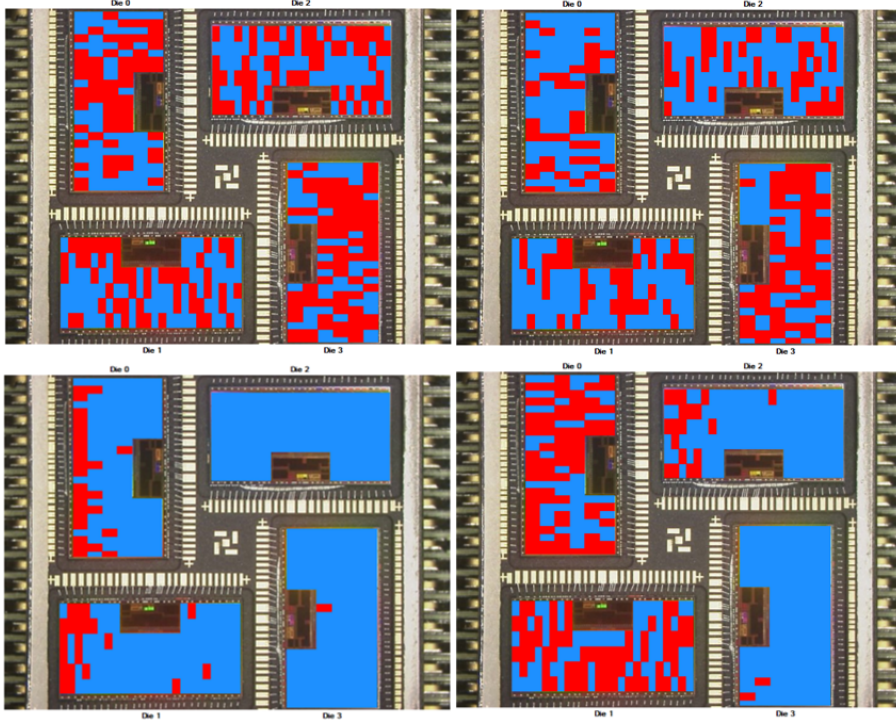


Figure 4.7: ESA Monitor events; the following distance refers to the left shift of the memory: at 13 mm on the top-left, 23 mm on the top-right, 43 mm on the bottom-left, 53 mm on the bottom-right picture. Respectively the tests number 4,5,6,7.

A possible explanation of this observation could be that the real beam center was shifted toward the left and therefore to the right of the picture in Figure 4.6 for the horizontal axis. The 2 cm shift between the beam nozzle and the memory support, amounts to a beam offset within 2-3 degrees toward the left. Regarding the ESA Monitor, the equation $N_{SEU} = \sigma \cdot \Phi$ is valid either if the memory have been irradiated with a homogeneous flux or the total fluence, retrieved from an inhomogeneous flux, it is known. Since the reference flux provided by the facility covers only the center C for the ESA Monitor measurements and, as explained before, the mean flux for this position can be

obtained averaging the 5 given fluxes, the ESA Monitor thermal neutron cross section results $4.51 \cdot 10^{-15} \text{ cm}^2/\text{bit}$.

The previous reference value was measured in Orphée for the same technology and reference memory but for a different date code (1104): the cross section value is $3.3 \cdot 10^{-15} \text{ cm}^2/\text{bit}$.

In Figure 4.8 the ESA Monitor flux calibration are compared with that of the facility displayed to the top-right of the same figure. The beam center C has been considered the center + 3 mm to the left. The fluxes expressed in $\text{neutron}/\text{cm}^2/\text{s}$ are calculated from equation 4.2 considering the ESA Monitor cross section value of:

- Test 2¹, $\sigma = 4.51 \cdot 10^{-15} \text{ cm}^2/\text{bit}$

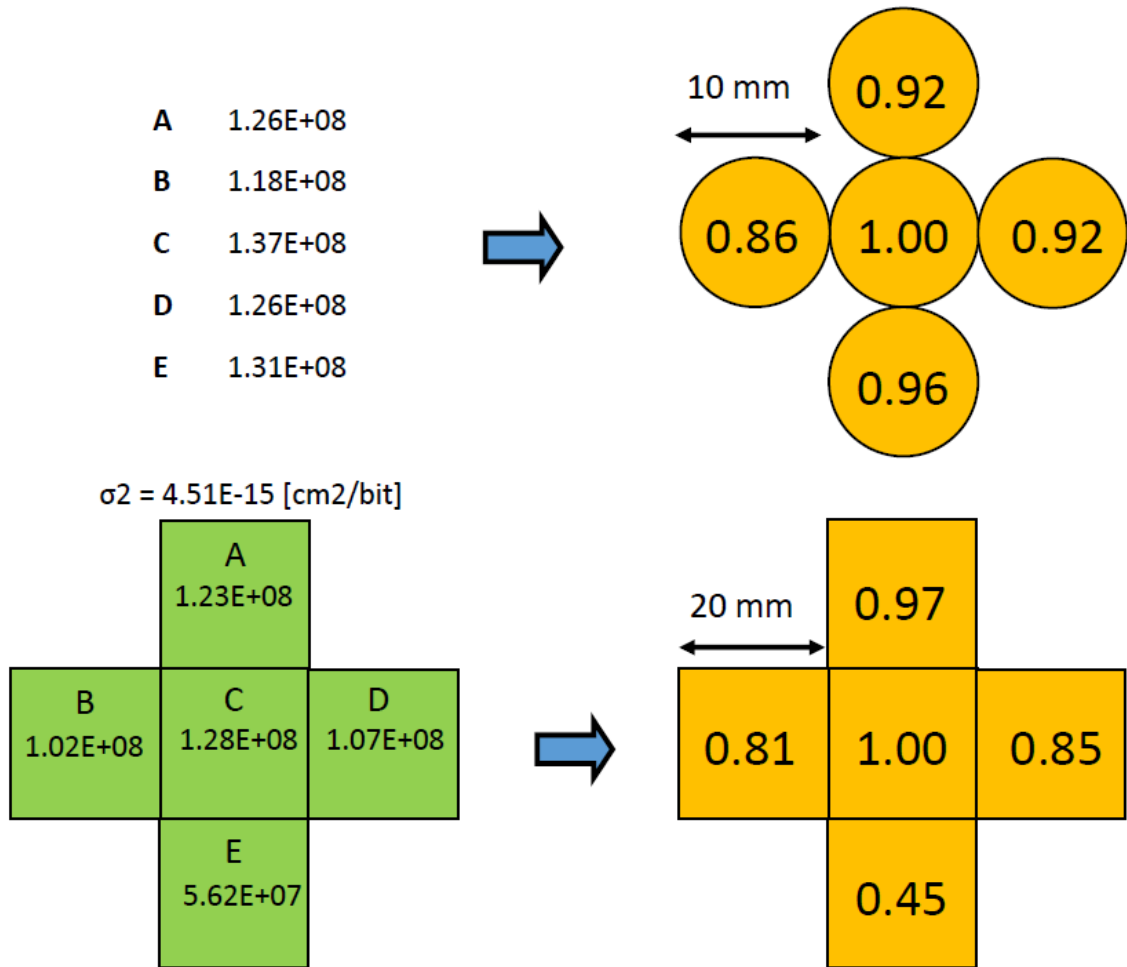


Figure 4.8: To the left, the ESA Monitor flux calibration [$\text{n}/\text{cm}^2/\text{s}$] (in green) with below the corresponding normalized values with respect to the center C, in comparison with the golden foil calibration of the ILL facility to the right.

¹Note that this is the value at 3 mm to the left from the facility center. It has been used for symmetric reason of the measurements.

Each square represents the total ESA Monitor active area, 20 x 20 mm. On the green area, C is the center (test 2), A and E the up and down measurements (test 11 and 12), B and D the left and right ones (test 5 and 9). By normalizing all the different tests by the central value C, we obtain the values reported in the yellow squares, which allow a direct comparison with the facility calibration. It is important to underline that the active areas are different: indeed the activation foils used in the facility calibration are 10 mm in diameter so that the comparison is only qualitative. With the ESA Monitor dimensions, the beam intensity to the bottom is half with respect to the center whereas on the other side the intensity decreasing is lower and almost unchanged on the top.

Overlaying the normalized ESA Monitor and gold-foil flux calibration, the covered area is reported in Figure 4.9.

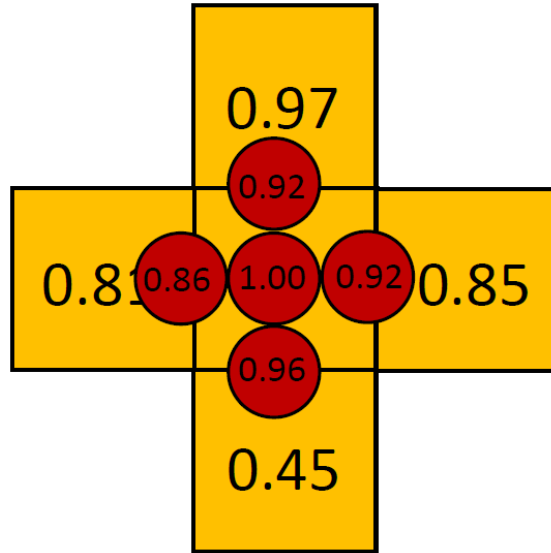


Figure 4.9: ESA Monitor (in yellow) and gold foil (in red) flux calibration.

In conclusion, the center 'c' of the beam provides the maximum mean intensity but from the ESA Monitor measurement is not very homogeneous over an area of 20 x 20 mm. By moving 23 mm toward left of the center 'c', the flux appears homogeneous but with half of intensity with respect to the center. The intensity decreasing is symmetric in the horizontal axis whereas differs of a factor two in that vertical.

4.1.1 ILL results

According to [14] the cross sections relative errors are calculated taking into account the Poisson distribution where the standard deviation is the square root of the events. In

particular:

1. If $N_{SEE} > 50$, $\sigma_{error} = \pm\sqrt{N_{SEE}}$
2. If $N_{SEE} < 50$, the upper limit instead of the SEE number was used from Table 4.1, and the error is retrieved making the difference between the upper and lower cross section, assessed with the same table.

Whereas for $N > 50$ the σ_{error} can be positive or negative around the cross section value, for $N < 50$ the relative error can be only negative. Note that in Table 4.5, the associated flux to the ESA Monitor is retrieved averaging the fluxes from the 5 activation foils, whereas for what concern the Cypress memory the flux is that measured on the single foil placed to the center because the area of the latter is smaller compared with that of the ESA Monitor.

Table 4.5: SEU tested SRAM memories at ILL, B means that 5 mm of boron carbide was covering the memory.

Memory	Date code	Setup	Time [s]	Flux [n/cm ² /s]	Fluence [n/cm ²]	SEU	σ [cm ² /bit]	% σ error
ESA M.	1330	no lid	180	$1.28 \cdot 10^8$	$2.47 \cdot 10^{10}$	1392	$4.51 \cdot 10^{-15}$	± 2.68
Cypress	1437	center	1205	$1.37 \cdot 10^8$	$1.65 \cdot 10^{11}$	618	$4.46 \cdot 10^{-16}$	± 4.02
Cypress	1443	center	1200	$1.37 \cdot 10^8$	$1.64 \cdot 10^{11}$	523	$3.79 \cdot 10^{-16}$	± 4.37
Cypress	1443	center	1200	$1.37 \cdot 10^8$	$1.64 \cdot 10^{11}$	521	$3.78 \cdot 10^{-16}$	± 4.38
Cypress	1443	center, B	300	$1.37 \cdot 10^8$	$4.11 \cdot 10^{10}$	3	$2.55 \cdot 10^{-17}$	$- 93.2$

Table 4.6: SEL tested SRAM memory at ILL.

Memory	Volt [V]	Time [s]	Flux [n/cm ² /s]	Fluence [n/cm ²]	SEL	σ [cm ² /chip]
Brilliance x8	5.5V	1200	$1.37 \cdot 10^8$	$1.64 \cdot 10^{11}$	0	$< 2.81 \cdot 10^{-12}$

4.2 14 MeV neutrons: LPSC

The "Laboratoire de Physique subatomique et de Cosmologie" (LPSC) relies on an accelerator-based neutron source GENEPI2 (GEnerator of NEutrons Pulsed and Intense) used to irradiate integrated circuits from different technologies. GENEPI2 is an electrostatic accelerator able to produce neutrons through the interaction of an accelerator deuteron beam (d) onto a fixed target made of tritium (T) or deuterium (D), depending on the

required neutron energy. In our interest the tritium was employed as it provides a neutron energy of 14.2 MeV. To generate the deuteron beam, a duoplasmatron source is used and by pulsing the ionizing plasma, ions are produced in the form of short and intense bunches. This beam is accelerated and focused and it impinges against a target (25 mm in diameter) made of a titanium layer loaded with tritium (TiT) or deuterium (TiD) deposited on a high purity copper disk. The activity of a fresh tritium decreases with beam operation because of tritium release caused by beam impact and target heating. Consequently, the target is air-cooled. Typically, a target can be used for a few years before depletion in the present operational conditions of GENEPI2. Neutrons are emitted from the target in the whole experimental room and the device under test (DUT) is placed directly facing the target.

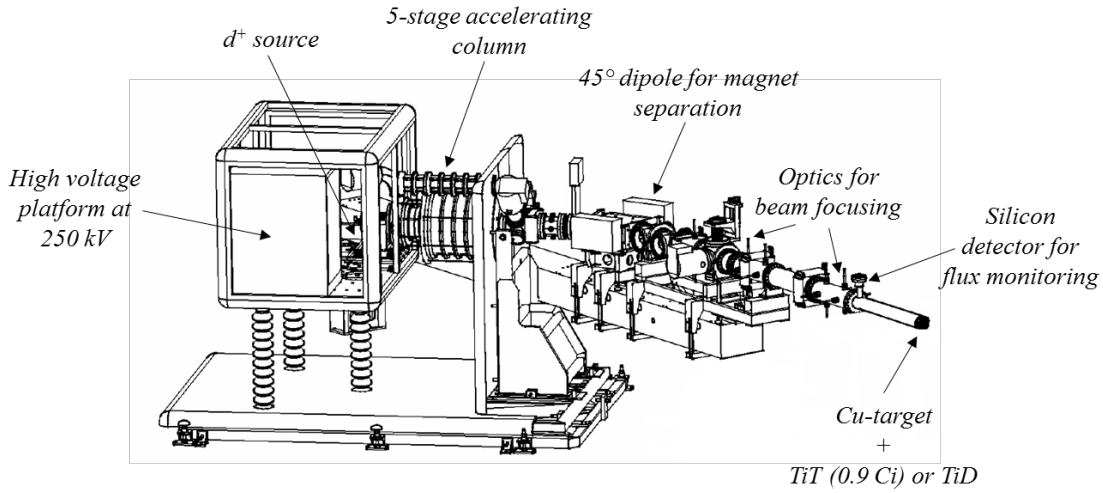


Figure 4.10: Layout of the GENEPI2 accelerator providing neutron beams at 14.2 MeV.

Monitoring The neutron flux produced by GENEPI2 is assessed and monitored through different systems. The neutron flux can be preliminary monitored through the real-time monitoring of the deuteron beam current impinging on the target: indeed, the neutron flux is proportional to the letter. The beam current is logged into a log file every second. To obtain a more accurate assessment of the neutron flux the activation technique was used with aluminium foils. it allows to evaluate the target ageing and its corresponding neutron flux reduction. Finally, the flux homogeneity was cross-validate through a board provided of a matrix of 75 SRAM 4-Mbit CY7C1041D memories and the results are reported in figure

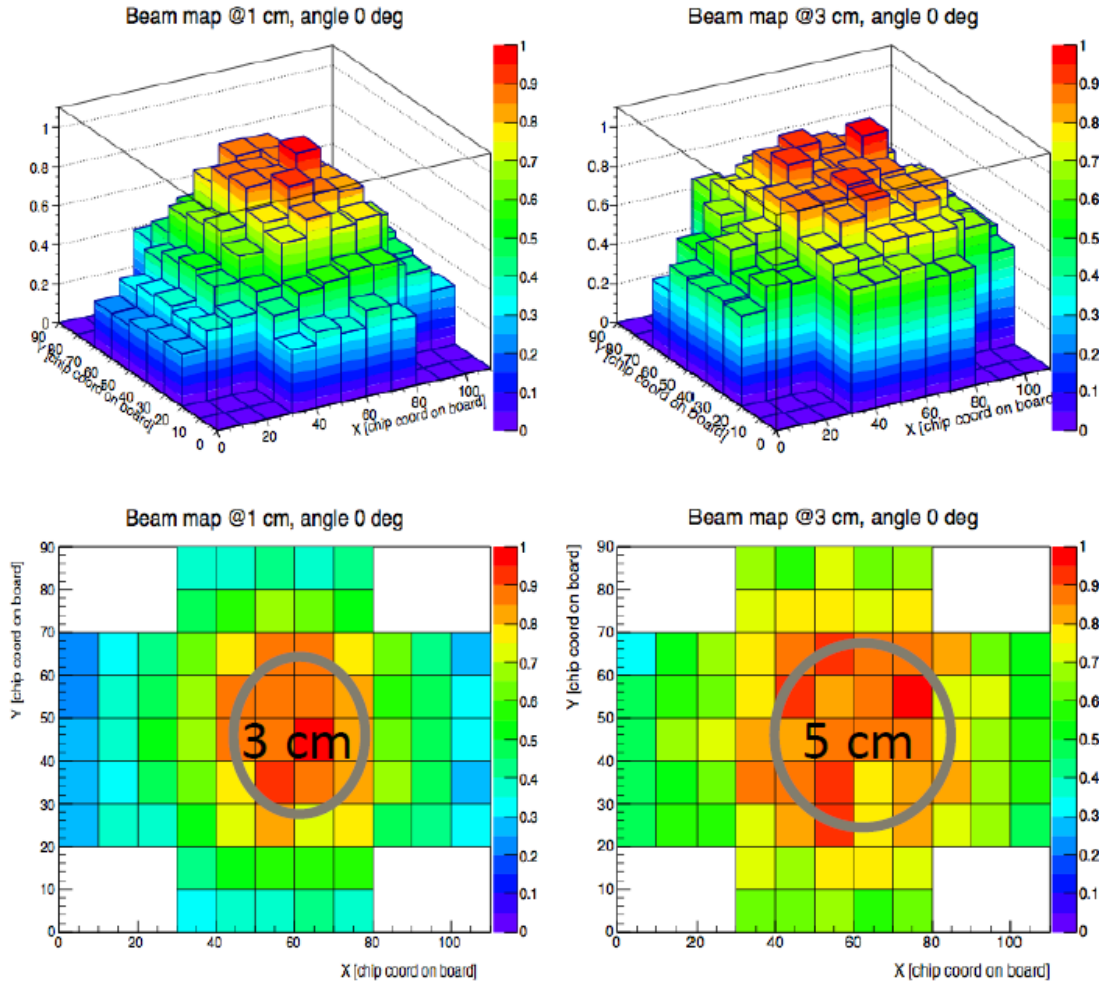


Figure 4.11: Flux homogeneity assessment at GENEPI2: the neutron flux resulted homogenous within an area of 3 cm and 5 cm, in diameter, at a distance of 1 cm and 3 cm from the target respectively.

At the time of the CERN test campaign, the facility provided a reference neutron flux, used in the following data analysis of $3.20 \cdot 10^7 \text{ cm}^{-2} \text{ s}^{-1}$ at 34 mm and $120 \mu\text{A}$.

LPSC calibration

Using the experimental setup described above, the ESA Monitor 1 with reference AT68166H-YM20-E and date code 1330 was irradiated for different irradiation times and at different distances as summarized in Table 4.8. The distance is relative to the center of the target source so that the outer surface is placed 24 mm onwards. For example, placing the memory at 25 mm is equivalent to say that the memory was at 1 mm from the outer surface of the machine. The distances were manually set with the aid of a ruler. The reference cross

section (highlighted in yellow) is calculated from equation 4.1 with the fluence value:

$$\Phi = \Delta t \cdot \varphi_{ref} \cdot \frac{I}{I_{ref}} \cdot \left(\frac{d_{ref}}{d_i} \right)^2 \quad \left[\frac{n}{cm^2} \right] \quad (4.4)$$

where Δt is the test time, $\varphi_{ref} = 3.2 \cdot 10^7 [cm^{-2}s^{-1}]$ is the reference flux at 34 mm provided by the facility as well as the reference current $I_{ref} = 120\mu A$ and I the average measured current during the test. In this case, there is no dependence with the distance because the fluence is that of reference at 34 mm. The cross section uncertainty was computed by a quadratic uncertainty propagation, i.e. considering three uncertainty contributes: the test time (0.3%), the average current (9%) and the reference flux uncertainty (4%).

Table 4.7: ESA SEU Monitor reference cross section.

Date code	Current [uA]	Distance [mm]	Test time [s]	Fluence [n/cm ²]	SEU	[cm ² /bit]	% error
1330	145	34	331	$1.28 \cdot 10^{10}$	5363	$2.49 \cdot 10^{-14}$	9.5

Considering the previous cross section $\sigma_{ref} = 2.49 \cdot 10^{-14} [cm^2/bit]$ (Table 4.7) as reference, since the flux provided by the facility refers to this position, the ESA Monitor measured fluxes are retrieved from Equation 4.2, with $nbit = 2^{24}$ the overall bit number of the 4 ESA Monitor dies. As the flux is inversely proportional to the square of the distance between the reference point and the other, the theoretical flux was calculated for a comparison with that of the ESA Monitor with $\varphi_{ref}^{EM} = 3.88 \cdot 10^7$:

$$\varphi(d_i) = \varphi_{ref}^{EM} \cdot \left(\frac{d_{ref}}{d_i} \right)^2 \quad \left[\frac{n}{cm^2s} \right] \quad (4.5)$$

$$\varphi_{ref}^{EM} = 3.88 \cdot 10^7$$

From the values of Table 4.8 it is possible to compare the measured neutron flux profile as a function of the distance with the neutrons flux provided by the facility (Figure 4.12): the two curves resulted in an excellent agreement within the 8%. The only point with a 15% of mismatch is that at 24 mm from the source center (only 1 mm from the source output) where small uncertainty in the positioning can lead to significant uncertainty in the flux assessment. Due to the manual positioning of the memory and the objective difficulty in assessing a proper uncertainty value this aspect was not included in the total uncertainty calculation.

Table 4.8: ESA SEU Monitor (E.M.) results (AT68166H-YM20-E reference board without the lid). Highlighted in yellow, the reference cross section for calculating the flux at different distance.

Date code	Current [uA]	Distance [mm]	Test time [s]	SEU	E.M. flux [cm^{-2}/s]	Theo flux [cm^{-2}/s]	% flux
1330	139	25	152	3872	$6.10 \cdot 10^7$	$7.17 \cdot 10^7$	15
1330	145	34	331	5363	$3.88 \cdot 10^7$	$3.88 \cdot 10^7$	0
1330	143	44	420	4260	$2.43 \cdot 10^7$	$2.32 \cdot 10^7$	-4.8
1330	136	54	300	1981	$1.58 \cdot 10^7$	$1.54 \cdot 10^7$	-2.8
1330	138	74	608	2244	$8.83 \cdot 10^6$	$8.19 \cdot 10^6$	-7.9

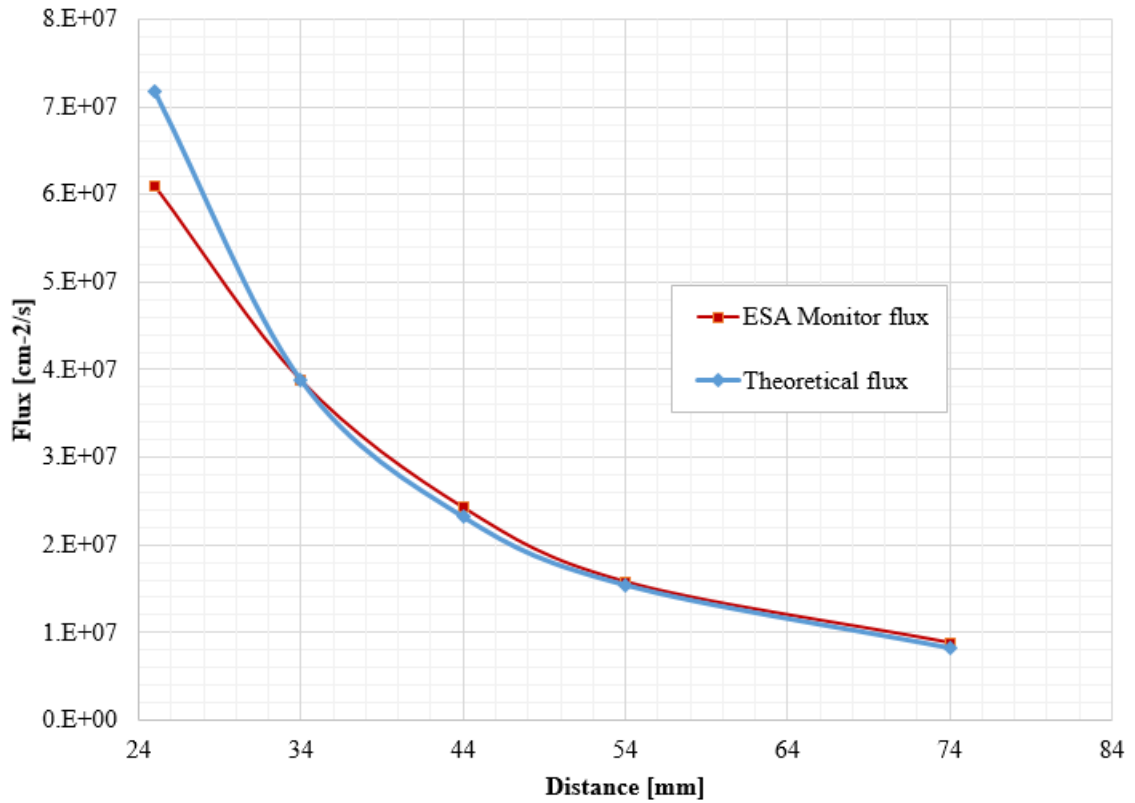


Figure 4.12: ESA Monitor flux vs distance from the center of the source, compared with that is inversely proportional to the square of the distance.

The beam homogeneity was checked using the ESA Monitor software as shown in Figure 4.13. Considering that the active area of the memory is 20 x 20 mm (from the start of the die0 to the end of the die2), looking at the SEU counts (red) it's clear that they are uniformly distributed in all the surface of the dies. Hence the LPSC 14 MeV beam is homogeneous. The homogeneity evaluation was performed at all the distances (not reported in this report) in which the tests were conducted: as for the 34 mm, an

overall good homogeneity was found.

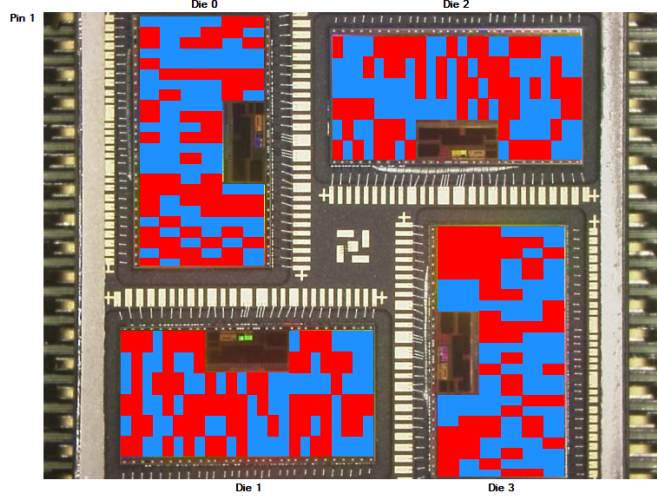


Figure 4.13: ESA SEU Monitor software showing the beam homogeneity at 34 mm, in red the occurred SEU.

4.2.1 LPSC results

The fluence values are retrieved from equation 4.4, where Δ_i is the test time, $\Phi_{ref} = 2.2E7[n/(cm^2s)]$ the reference flux, I_i the measured current and $I_{ref} = 120\mu A$ the reference current provided by the facility. The cross section errors are retrieved as in the LPSC calibration section, as well as the uncertainty (deducted from flux, time and current uncertainties).

Table 4.9: SEU tested SRAM memories at LPSC 14 MeV neutrons. The memory reference can be retrieved from the date code and Table 4.2, the ESA Monitor was without lid and 180° means that the board was turned of 180 degree.

Memory	Date code	S	Current [uA]	Distance [mm]	Time [s]	Fluence [n/cm ²]	SEU	σ [cm ² /bit]	% σ error
ESA M.	1104		134	34	300	$1.07 \cdot 10^{10}$	4349	$2.43 \cdot 10^{-14}$	12.3
ESA M.	1104	180°	127	44	150	$3.04 \cdot 10^9$	480	$9.42 \cdot 10^{-15}$	15.6
ESA M.	1330		145	34	331	$1.28 \cdot 10^{10}$	5363	$2.49 \cdot 10^{-14}$	9.5
Cypress	1443	-	130	54	392	$5.38 \cdot 10^9$	3072	$6.81 \cdot 10^{-14}$	13
Cypress	1443	180°	123	54	360	$4.70 \cdot 10^9$	1145	$2.91 \cdot 10^{-14}$	14

Noteworthy is the fact that whereas the Brilliance 8x powered with 3.3V recorded two-third of SEUs compared with those of the same memory but supplied with 5.5V, the Brilliance 1x recorded zero events at low voltage 3.3V and 50 at 5.5V. This could be associated to the fact that they have two different date code, respectively 12094 (8x) and

Table 4.10: SEL tested SRAM memories at LPSC 14 MeV neutrons.

Memory	Volt [V]	Current [uA]	Distance [mm]	Time [s]	Fluence [n/cm ²]	SEL	σ [cm ² /chip]
Brilliance x1	5.5	124	54	1800	$2.36 \cdot 10^{10}$	50	$2.11 \cdot 10^{-9} \pm 16.5\%$
Brilliance x1	3.3	123	54	1380	$1.79 \cdot 10^{10}$	0	$< 2.06 \cdot 10^{-10}$
ISSI x8	3.3	148	44	1216	$2.91 \cdot 10^{10}$	1	$< 2.41 \cdot 10^{-11}$
Lyontek x8	5.5	137	44	1200	$2.92 \cdot 10^{10}$	10	$< 7.88 \cdot 10^{-11}$
Lyontek x8	3.3	133	44	1200	$2.83 \cdot 10^{10}$	5	$< 5.16 \cdot 10^{-11}$
Brilliance x8	5.5	150	44	1200	$2.62 \cdot 10^{10}$	33	$< 2.21 \cdot 10^{-10}$
Brilliance x8	3.3	153	44	1200	$2.55 \cdot 10^{10}$	22	$< 1.63 \cdot 10^{-10}$

11254 (1x) and the behaviour as a function of the voltage is very different.

Moreover, the cross sections are reduced by a factor 2-3 when the memories are rotated of 180 degree and irradiated on the back part. It's owing to the presence of oxygen in the Back End of Line (BEOL) that interacts with neutrons and it generates secondary particles. Instead, rotating the board, the neutrons pass basically through silicon and silicon oxides producing elastic interactions (i.e other particles different from those primaries are not generated) [23], [24].

4.3 Am-Be neutron source and spectrum

With the aim of evaluating the possible employment of the Americium-Beryllium facility located at CERN for the screening of components, the calibration of the source through the ESA Monitor and FLUKA simulations was carried out and the first SEU results was obtained using the Cypress memory, the same tested in Grenoble (see Chapter 4.0.1).

Neutrons are generated after the absorption of alpha particles, emitted from the americium, by the beryllium. The activity of the employed source is of 888 GBq with a neutron energy up to 10 MeV. The facility is composed by the irradiation room showed in Figure 4.14. The source lies inside a storage at the bottom of the room and when turned on, by means of compressed air, it raises up inside the aluminum pipe (see Figure 4.14) reaching the exposure position, with its center at 35.6 cm above the little table. In this way, since the source remains at the middle of the entire room, the irradiation is isotropic and the neutron flux results of $5.03 \cdot 10^7$ [n/s] $\pm 5\%$ ([18], [17]).



Figure 4.14: Am-Be irradiation room to the left and source exposure position to the right.

FLUKA simulations vs the ESA Monitor calibration

The original source geometry (from [18]) is shown in Figure 4.15 with the addition of different detectors placed at different distances from the source (z axis and y axis), in order to evaluate the neutron flux in these regions. The detector size is small enough (0.1x1x1cm) to resemble the typical sensitive area dimensions of SRAM memories. The source center, in the FLUKA geometry, is located at (x,y,z)=(-10,120,-50) cm and com-

posed by a cylinder 7,62 cm long and with a diameter of 2.54 cm. However, in the following result tables the distances are relative to the table base (y) and the center of the source (x,z), expressed in cm.

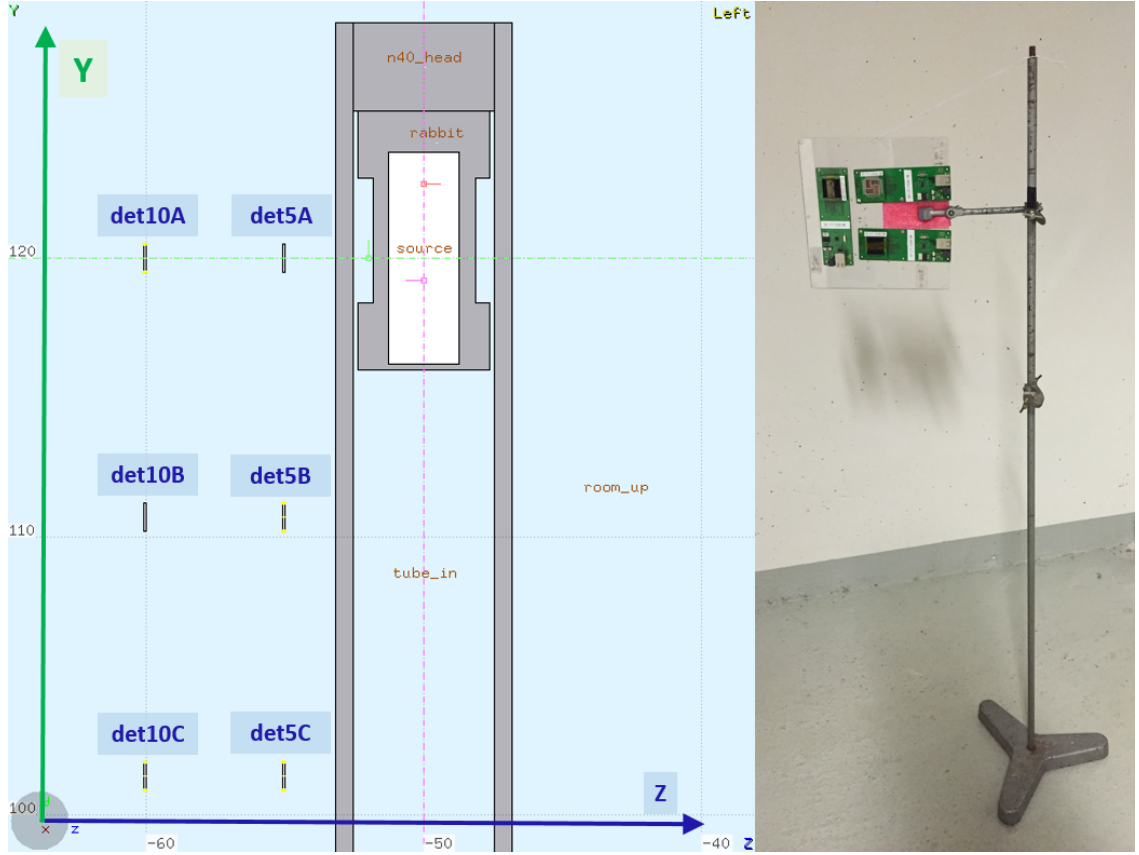


Figure 4.15: To the left, the FLUKA geometry and detectors (det10D and det5B are behind det10A and det5A). To the right, the support used to sustain the ESA Monitors and devices during the irradiation.

Regarding the FLUKA scoring, neutrons and HEHeq have been calculated. The spectrum of the source (neutrons) is plotted in Figure 4.16. At 10 cm from the source center the neutron flux is reduced (det10A neutrons) of a factor 40 for the energy of 1 MeV, compared to the source spectrum. As can be expected, also the HEHeq fluxes, computed through FLUKA relying on the Toshiba response, decrease of about the same factor, with increasing the distance and high with respect to the source center. They are shown in Table 4.11 comparing the fluxes with those retrieved manually considering the ESA Monitor Weibull response function.

Table 4.11: HEHeq fluxes at 5 cm and 10 cm of distance (z axis) from the center of the source (det5A, det10A in Figure 4.15), retrieved from FLUKA (Toshiba response) and by applying the ESA Monitor Weibull response to the neutron spectrum.

	Response	5 cm	10 cm
HEHeq	Toshiba (FLUKA)	$1.84 \cdot 10^4$	$5.05 \cdot 10^3$
$[n/cm^2/s]$	ESA M. (manual)	$9.32 \cdot 10^3$	$2.61 \cdot 10^3$

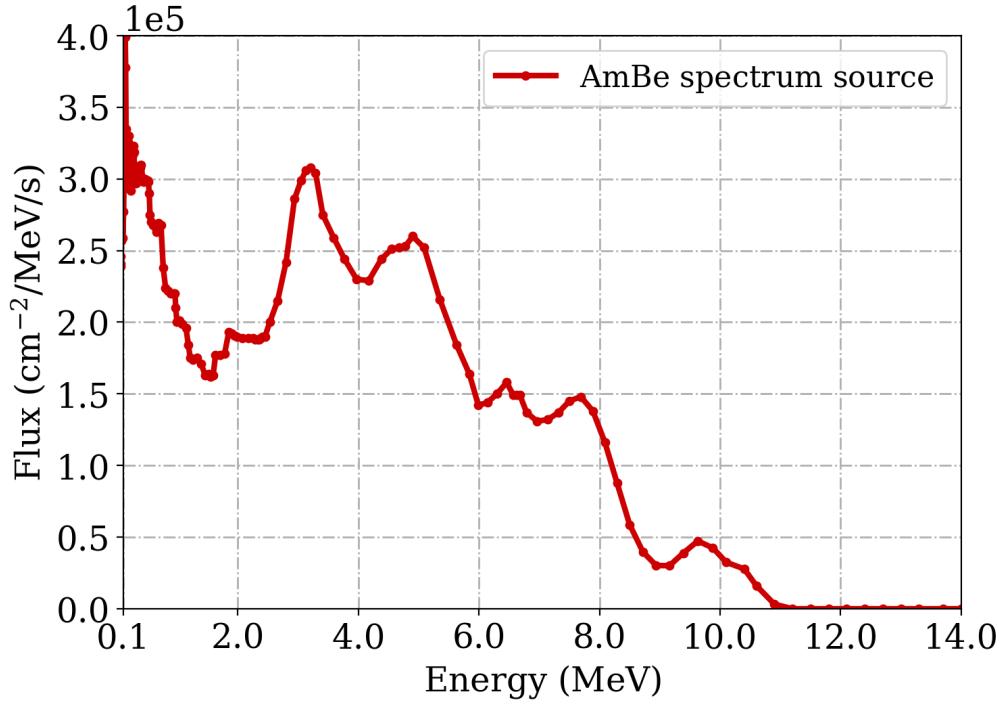


Figure 4.16: Neutron spectra as a function of the energy of the source.

The flux was benchmarked with the ESA Monitor (1330) without the lid in 8 different positions, as outlined in Table 4.13. The cross sections values are retrieved dividing the upset number by the HEHeq fluence calculated through FLUKA. The percentage refers to the difference between the measured cross section and the reference value of $2.63 \cdot 10^{-14} \text{ cm}^2/\text{bit}$. Since the HEHeq given from the simulations relies on the Toshiba response, by using the ESA Monitor Weibull parameters in Table 4.12 from [19], the HEHeq(ESA) was manually derived by multiplying each flux value $[n/cm^2/s]$ for every energy interval, by the Weibull function also energy-dependent (see Table 4.11). The results comparison is reported in Table 4.14 for the position at the center of the source along the y axis and with two different distances (z axis): the cross sections retrieved with this approach are much more compatible, within 15%, with that measured at 230 MeV (PSI).

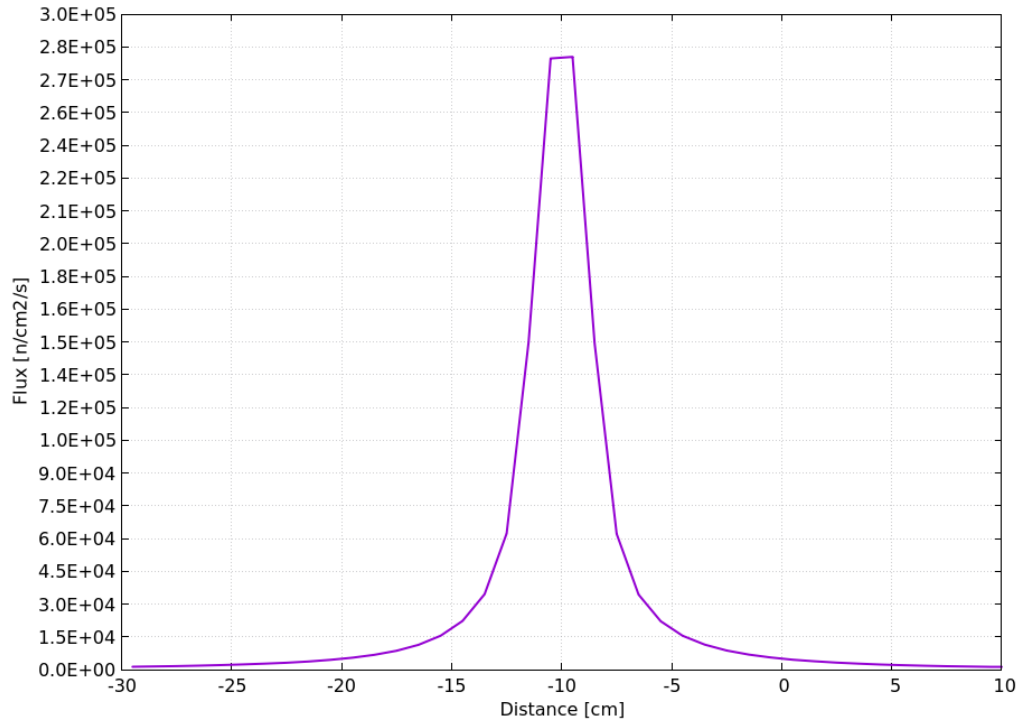


Figure 4.17: Flux intensity along the x axis (as well as along z) as a function of the distance. The source center is located at -10 cm in the simulation.

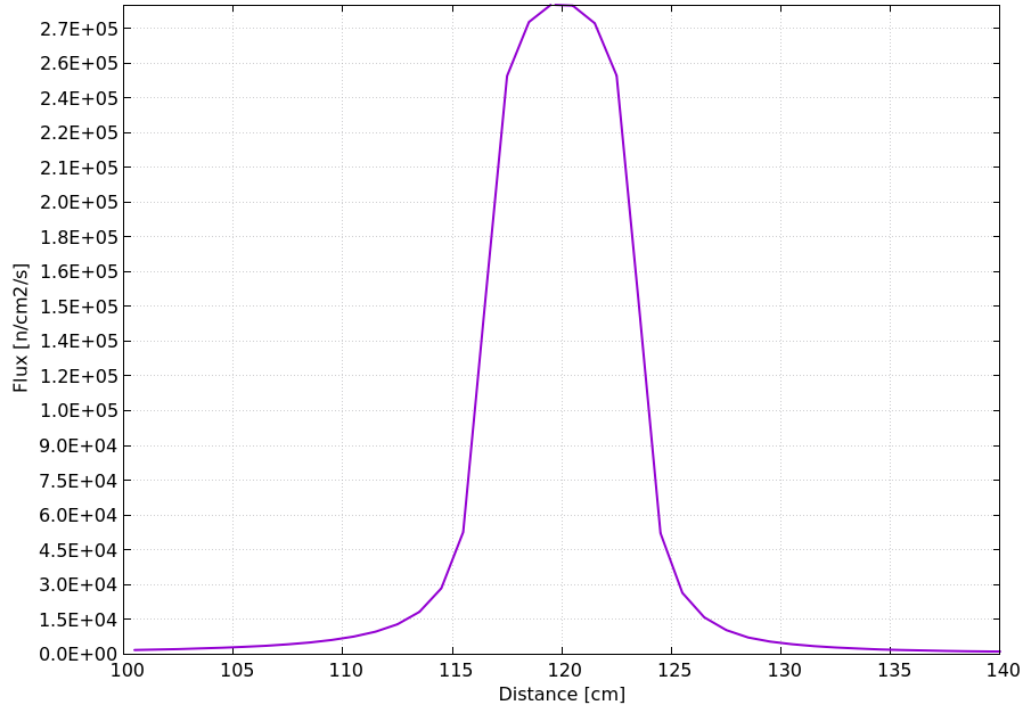


Figure 4.18: Flux intensity along the vertical y axis as a function of the distance. The source center is located at 120 cm from the floor in the simulation.

Table 4.12: Weibull parameters: Toshiba and ESA Monitor.

Memory	W [MeV cm^2 /mg]	s
Toshiba	9.25	3.02
ESA Monitor	11.6	3.14

Table 4.13: ESA Monitor measured cross sections retrieved using the HEHeq fluence from the simulations in comparison with $2.63 \cdot 10^{-14} \text{ cm}^2/\text{bit}$, the calibrated cross section at 230 MeV.

Detector	Position			Time [h]	SEU	XS [cm^2/bit]	%	HEHeq(sim) [cm^{-2}]
	z	y	x					
det5A	5	35.6	0	61.8	856	$1.25 \cdot 10^{-14}$	-110.5	$4.08 \cdot 10^9$
det10A	10	35.6	0	61.4	301	$1.61 \cdot 10^{-14}$	-63.6	$1.12 \cdot 10^9$
det5D	5	35.6	6.7	61.8	471	$1.79 \cdot 10^{-14}$	-46.9	$1.57 \cdot 10^9$
det10D	10	35.6	6.7	61.4	245	$1.88 \cdot 10^{-14}$	-39.6	$7.75 \cdot 10^8$
det5B	5	26.3	0	61.8	257	$1.53 \cdot 10^{-14}$	-71.9	$1.00 \cdot 10^9$
det10B	10	26.3	0	61.4	182	$1.80 \cdot 10^{-14}$	-46.1	$6.03 \cdot 10^8$
det5C	5	16.5	0	61.8	55	$1.19 \cdot 10^{-14}$	-121.7	$2.76 \cdot 10^8$
det10C	10	16.5	0	61.4	60	$1.56 \cdot 10^{-14}$	-68.5	$2.29 \cdot 10^8$

Table 4.14: cross sections differences using either the Toshiba or the ESA Monitor response to calculate the HEHeq fluence.

Weibull	Detector	z [cm]	SEU	HEHeq(sim) [cm^{-2}]	XS [cm^2/bit]	%
Toshiba	det5A	5	856	$4.08 \cdot 10^9$	$1.25 \cdot 10^{-14}$	-110.5
ESA	det5A	5	856	$2.07 \cdot 10^9$	$2.46 \cdot 10^{-14}$	-6.9
Toshiba	det5A	10	301	$1.12 \cdot 10^9$	$1.61 \cdot 10^{-14}$	-63.6
ESA	det5A	10	301	$5.78 \cdot 10^8$	$3.10 \cdot 10^{-14}$	15.3

Cypress SEU tests

Two Cypress memories with different date code were tested at 5 cm from the source in the center position. the results are shown in Table 4.15.

Table 4.15: Cypress cross section by using the Am-Be source.

Detector	Memory	Date code	Position [cm]			Time [h]	SEU	HEHeq(sim) [cm^{-2}]	XS [cm^2/bit]
			z	y	x				
det5A	Cypress	1443	0	35.6	5	52.7	1754	$3.48 \cdot 10^9$	$3.00 \cdot 10^{-14}$
det5A	Cypress	1437	0	35.6	5	9.2	292	$6.11 \cdot 10^8$	$2.85 \cdot 10^{-14}$

Chapter 5

SEE results: standard test approach versus CHARM

This chapter summarizes the main cross sections results of the memories tested at CHARM against those tested in the other facilities object of this work. Furthermore the comparison is presented also regarding measurements carried out in standard mono-energetic facilities from previous tests for the same components([25]).

SEU cross sections results

Table 5.1: ESA Monitor thermal neutron and High energy hadron cross sections results obtained in different facilities.

Memory	Date code	Facility	Energy	HEH [cm^2/bit]	thn [cm^2/bit]
ESA M.	1104	CHARM(O)	mixed-field	$2.45 \cdot 10^{-14}$	$2.87 \cdot 10^{-15}$
ESA M.	1330	CHARM(C)	mixed-field	$2.38 \cdot 10^{-14}$	$4.25 \cdot 10^{-15}$
ESA M.	1104	LPSC	14 MeV	$2.43 \cdot 10^{-14}$	-
ESA M.	1104	PSI	230 MeV	$2.63 \cdot 10^{-14}$	-
ESA M.	1330	CHARM(O)	mixed-field	$2.67 \cdot 10^{-14}$	$2.36 \cdot 10^{-15}$
ESA M.	1330	LPSC	14 MeV	$2.49 \cdot 10^{-14}$	-
ESA M.	1330	ILL	thermal	-	$4.51 \cdot 10^{-15}$
ESA M.	-	Orphee	thermal	-	$3.30 \cdot 10^{-14}$
ESA M.	1330	AmBe	<10 MeV	$3.10 \cdot 10^{-14}$	-

The ESA SEU Monitor cross sections are shown in Table 5.1. Regarding CHARM, the results rely on the date code 1104 or 1330, in M0 position for Cu-O000 (O) and Cu-CHC (C) configurations and they are extrapolated from Table 3.7. As can be seen the high-energy cross sections are not affected among the two date codes and they are perfectly

compatible between those measured in mono-energetic facilities at different high energies (within the experimental error). For instance CHARM compared with PSI are consistent within 7%. The HEH cross section from CHARM (C) is the average between two values with a very large spread, thus though it gives a coherent result it is just a coincidence and therefore written in red. The agreement is also valid for the thermal neutron cross section within a factor 2; if we consider as reference the cross section retrieved at ILL, the measurement with the full shielding at CHARM come closest with respect to the results without shielding. Impressive is also the excellent agreement obtained by using the Am-Be source (which has a maximum energy of 10 MeV) weighting the neutron fluence with the ESA Monitor Weibull fit.

Table 5.2: Cypress cross section results obtained in different facilities.

Memory	Date code	Facility	Energy	HEH [cm^2/bit]	thn [cm^2/bit]
Cypress	-	CHARM	mixed-field	$2.35 \cdot 10^{-13}$	-
Cypress	1443	LPSC	14 MeV	$6.81 \cdot 10^{-14}$	-
Cypress	1437	ILL	thermal	-	$4.46 \cdot 10^{-16}$
Cypress	1443	ILL	thermal	-	$3.79 \cdot 10^{-16}$
Cypress	1443	AmBe	10 MeV	$3.00 \cdot 10^{-14}$	-
Cypress	1437	AmBe	10 MeV	$2.85 \cdot 10^{-14}$	-
Cypress	-	PSI	200 MeV	$2.13 \cdot 10^{-13}$	-

Moreover, as far as the Cypress memory is concerned (SEU) the high-energy cross section retrieved from CHARM is compatible with that of PSI and lowering the energy to 14 MeV, the relative cross section decreases of a factor 3.5. However the cross section at 14 MeV (LPSC) is in agreement with that derived in the Am-Be source within a factor 3. The measurements performed at CHARM refers to the position 10 with no shielding Cu-OOOO and together with that of PSI are reported in [27].

SEU radiation hardness assurance: As shown, the agreement by using facilities with a wide range of energies, from less than 10 MeV of the Americium-Beryllium up to 230 MeV of PSI, yields the same results within the experimental uncertainty. This is unfolded from the fact that the memory cross section follows the response curve implemented with the Weibull fit. In other words the convolution as a function of the energy of the particle fluence and the memory cross section is representative of the number of SEU counts for a broad range of environments: $N_{SEU} = \int_0^{+\infty} \sigma(E) \cdot \Phi(E) dE$. Indirectly, through experimental observations it is proven that the HEHeq fluence retrieved with the specific Weibull fit is applicable to different particle energy spectra. This is a validation

about the correctness of the response function. This aspect enables the SEU screening of SRAM memories in sources such as the Am-Be and 14 MeV described above, generally more cost efficient than high-energy cyclotron proton testing. For example, the Am-Be source reproduces the same response of the high energy mono-energetic beams in terms of measured SEU.

SEL cross sections results

Table 5.3: SEL cross section results obtained in different facilities. Some results are the upper limit since the event statistic was below 10 events. CHARM results refer to M0 position except for Alliance* which was in G0.

Memory	Facility	Energy	[V]	σ [cm ²]
Alliance*	CHARM	mixed-field	3.3	$5.06 \cdot 10^{-11}$
Alliance*	PSI	230 MeV	3.3	$3.40 \cdot 10^{-10}$
ISSI	CHARM	mixed-field	3.3	$1.69 \cdot 10^{-8}$
ISSI	PSI	230 MeV	3.3	$2.30 \cdot 10^{-8}$
ISSI	LPSC	14 MeV	3.3	$< 2.41 \cdot 10^{-11}$
Brilliance	CHARM	mixed-field	3.3	$2.18 \cdot 10^{-8}$
Brilliance	CHARM	mixed-field	5.5	$2.40 \cdot 10^{-8}$
Brilliance	RCNP	300 MeV	3.3	$3.15 \cdot 10^{-8}$
Brilliance	LPSC	14 MeV	3.3	$< 1.63 \cdot 10^{-10}$
Brilliance	LPSC	14 MeV	5.5	$< 2.21 \cdot 10^{-10}$
Brilliance	ILL	thermal	5.5	$< 2.81 \cdot 10^{-12}$
Brilliance1x	CHARM	mixed-field	3.3	$1.71 \cdot 10^{-7}$
Brilliance1x	CHARM	mixed-field	5.5	$3.83 \cdot 10^{-7}$
Brilliance1x	LPSC	14 MeV	3.3	$< 2.06 \cdot 10^{-10}$
Brilliance1x	LPSC	14 MeV	5.5	$2.11 \cdot 10^{-9}$
Lyontek	CHARM	mixed-field	3.3	$1.68 \cdot 10^{-8}$
Lyontek	CHARM	mixed-field	5.5	$2.49 \cdot 10^{-8}$
Lyontek	PSI	230 MeV	5.0	$4.60 \cdot 10^{-8}$
Lyontek	LPSC	14 MeV	3.3	$< 5.16 \cdot 10^{-11}$
Lyontek	LPSC	14 MeV	5.5	$< 7.88 \cdot 10^{-11}$

The cross sections regarding ISSI, Brilliance and Lyontek is shown in Table 5.3 and they are compatible between facilities within a factor 3 considering the high energy fields (not for 14 MeV). Some of the represented values are the upper limit of the cross section because wither the measured events were zero or no events were recorded; therefore it is not surprising if the Lyontek cross section at 5.5V (LPSC) is lower than that powered at 3.3V. The Alliance memory is the only exception, the CHARM value is roughly a

factor 7 smaller than the 230 MeV value due to the strong energy dependence of tungsten inside the composition of the memory ([26]). Whereas the results are compatible between CHARM and high energy beam facilities, regarding the tests carried out at 14 MeV the cross section is even two order of magnitude lower compared with the former.

SEL radiation hardness assurance: It has been demonstrated that at the CHARM facility and those of high energy fluxes, the cross sections are compatible because the most of the mixed field at CHARM is composed by high energy particles, i.e high particle fluence that satisfies the relation $N_{SEL} = \int_0^{+\infty} \sigma(E) \cdot \Phi(E) dE$. Instead, by using the 14 MeV beam it is not representative of higher energies because its cross section is too low to assure the validity of the previous expression. Therefore, for SEL the 14 MeV screening approach proposed above does not apply as the risk of significantly underestimating the high-energy cross section is large.

Chapter 6

Conclusions and Outlook

The thermal neutron and high-energy hadron cross sections are the key findings for the SEE qualification of components for high-energy accelerator applications, as the relative contribution of the thermal and high-energy hadron fluxes largely varies within the accelerator, thus knowing the individual responses is essential in order to estimate the operation SEE rate.

As the accelerator environment presents a very broad range of ratios among thermal and HEH fluences, this work shows the possibility of retrieving different R-factors ranging between values compatible with zero and 34, by changing CHARM shielding in combination with the local use of boron carbide. This aspect is the starting point for reproducing the LHC areas subjected to high levels of ionizing radiation which house electronic systems based on COTS components.

Beside the measurements carried out with the RadMon system to assess the thermal and HEHeq fluences, the FLUKA simulation results concerning the HEH fluence were in good agreement with those retrieved from the RadMon system. However, with regards to the employment of the CHARM facility using the full shielding configuration, the agreement was expected to be more satisfactory and this will be a topic of further investigation. As to what regards the thermal neutron fluence, as expected the agreement with the simulations is less satisfactory due to its very large dependence on the specific material composition and the impossibility of describing it at the required accuracy level.

By combining the fact that the number of SEEs can be retrieved through the sum of the products of the HEH and thermal neutron fluences and cross sections and the boron carbide property of absorbing the thermal neutrons, the thermal neutron fluence

is significantly reduced while maintaining the HEH fluence almost unaltered. This leads to the differential approach through the boron carbide deployment with the purpose of retrieving the HEH and thermal neutron cross sections. It was successfully applied to the neutron-dominated location at CHARM proving that it can be used to characterize the SEE response of memories that will be installed in areas with a large R-factor representative of the LHC accelerator shielded locations. The procedure is a novel approach at CHARM which will enable the systematic evaluation of the sensitivity of state-of-the-art components to thermal neutrons.

At the CHARM facility SEU and SEL memories tests were conducted in order to validate the differential approach. Its results were compared with tests on the same memories but in different facilities and for most memories the CHARM cross section values are within a factor 3 with respect to those measured at other facilities. The only exception was observed with the Alliance memory where the CHARM value is roughly a factor 7 smaller than the 200 MeV value but this fact is attributed to the strong energy dependence of the SEL cross section of the component and the relatively soft spectrum used at the respective CHARM location. Aside from that, the HEH and thermal neutron cross sections retrieved at CHARM for the ESA Monitor are both in agreement within a factor 2 with those measured in high energy beams, 14 MeV neutrons and even the Americium-Beryllium source which provides a maximum energy of 10 MeV. The same agreement is observed for the Cypress memory where the CHARM cross section satisfies that of PSI and within a factor of 4 is compatible with a 14 MeV neutron source. This result therefore enables the use of the more accessible and cost-efficient Am-Be and 14 MeV neutron environments as a means of screening the SEU sensitivity of components before performing tests in high-energy proton or mixed-field environments.

Moreover, whereas 14 MeV neutrons are capable of reproducing the 200 MeV and CHARM cross section within 20% for the ESA Monitor and a factor 3 for the Cypress, for SEL, 14 MeV cross sections are over an order of magnitude lower. Therefore the procedure was successful in the case of SEU but clearly underestimated the sensitivity for SEL, as supported by the different sensitive volumes and LET cross sections involved. Furthermore, regarding the memories tested for SEL, the results show they are not sensitive to thermal neutrons, as opposed to those for SEU.

In conclusion, CHARM showed to be a potential tool for testing memories to retrieve both thermal neutron and HEH cross sections through the differential approach. This

approach can lead to a significant reduction of the overhead involved in qualifying both sensitivities independently in dedicated facilities and will be employed to accomplish measurements on the state of art components to be installed in critical LHC areas. In addition, the simulations and calibrations of the Am-Be neutron source established the unexpected capability of providing the high energy SEU cross section when considering a generalized response for neutrons in the 0.2-20 MeV range.

Appendix

BLM analysis and observations

NOTE: to extract data from TIMBER every 15 minutes (or with any other time-scale) as the BLMs values are represented in [Gy/s], it would be normal to retrieve them applying the average (AVG) as opposed to the SUM operation for the counts because each spill carries energy which is converted into POT which is a cumulative effect. More spill arrive and more the devices at CHARM are radiated, differently from the BLMs that measure every few seconds the amount of received dose in one second. However this second to which the BLM value relates is not the S.I. standard second but rather it refers to 655,36 ms for hardware constraint in elaborating the signal. The correct dose in [Gy/s] with the S.I. units, can be retrieved with the following formula:

$$Total_{dose}[Gy/s] = \sum_{i=1}^n x_i \cdot 655,36 \cdot 10^{-3} \quad (6.1)$$

where x_i are the raw samples of arbitrary period time extracted from TIMBER with the SUM option, n is the last BLM value. On the contrary instead with the AVG time-scale TIMBER extracts the BLMs data making the average as the values are related to 1 second and not to 655,36 ms. The solution is employing the 6.4 formula but in case of owning a large amount of data retrieved with the AVG time-scale, as in the case of the 2016 tables, hereafter is unfolded how to obtain the correct value in [Gy/s]. The results making the AVG every 15 minutes as regards the BLMs values is compute from TIMBER as

$$BLM_{AVG}^{dose}[t_1, t_2] = \frac{\text{single BLMs values in } [t_1, t_2]}{\text{number of BLMs values in } [t_1, t_2]} \quad (6.2)$$

Where $[t_1, t_2]$ are the 15 minutes timeslot but it's valid for a generic $[t_1, t_2]$ interval. It must be considered that this last result relies on the non-standard unit of time. By having all the BLMs averages values every 15 minutes the objective is to calculate the week total dose. For this aim one should know exactly the number of BLMs recorded values in every specific slot of 15 minutes time and weight them with its average. For instance with only

two 15 min BLM AVG samples the result would be

$$Total\ dose\ from\ BLM_{AVG} = \frac{AVG_1 \cdot \#val_1 + AVG_2 \cdot \#val_2}{\#val_1 + \#val_2} [Gy/s] \quad (6.3)$$

Since the number of recorder BLMs values ($\#val_1, \#val_2, \dots$) is not known a priori, a correction factor is needed to obtain the real dose in [Gy/s]. Knowing the mean number of recorded BLM values per second, that for W25 selected as reference are 0.607198082 rec/s (determined taking all the BLM values in the operation week from TIMBER with no option time-scale and dividing them by the elapsed seconds of the week. This ratio is quite constant over all the weeks), multiplying the latter by 15*60 seconds, the number of BLM recorded values in 15 minutes is retrieved and equal to 546,47827. By doing so, the real [Gy/s] dose can be derived multiplying every 15 minutes AVG values by the number of BLMs recorded values (thus indirectly retrieving $\sum_{i=1}^n x_i$) and finally by 655,36 ms, like in the first total dose formula 6.4. This process yields the final formula:

$$Total_{dose\ 15min}[Gy/s] = BLM_{AVG}^{dose}[15min] \cdot 546,47 \cdot 0,65536 \quad (6.4)$$

Summing all these 15 min values, the total dose for the considered week is retrieved.

A typical behaviour of one week is illustrated in Figure 6.1, 6.2 and 6.3 related to the week 25. The shielding configuration was Cu-OOOO. They outline a typical run week at the CHARM facility.

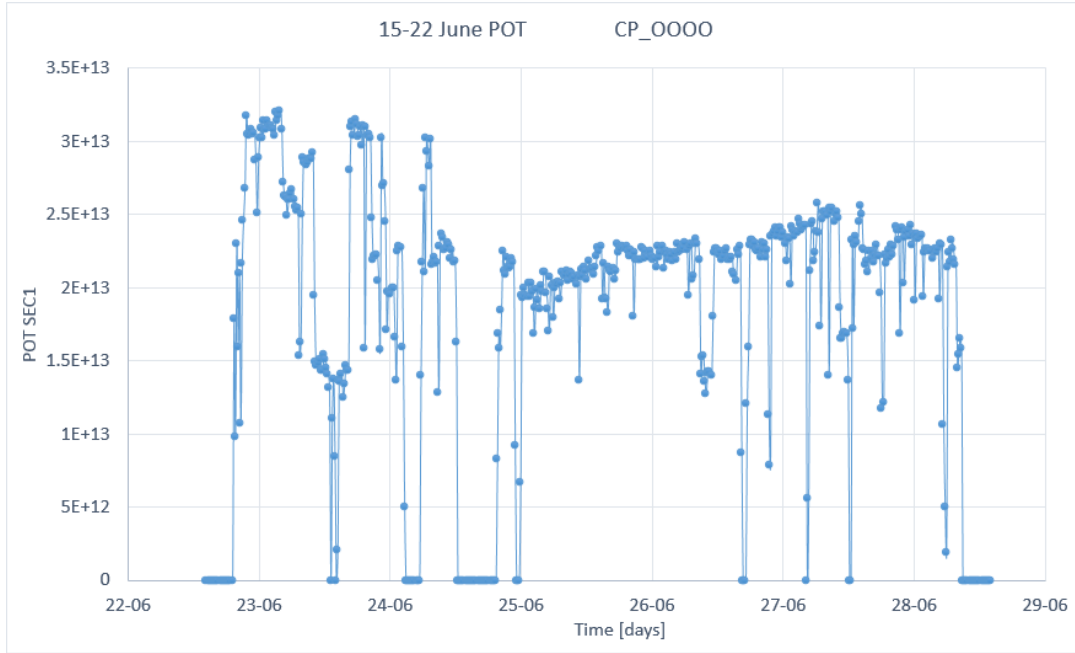


Figure 6.1: POT trend of SEC1 for W25. Note that during the run, occasionally the SEC1 measured zero counts and this may be due to losses at PS; also the intensity was not constant.

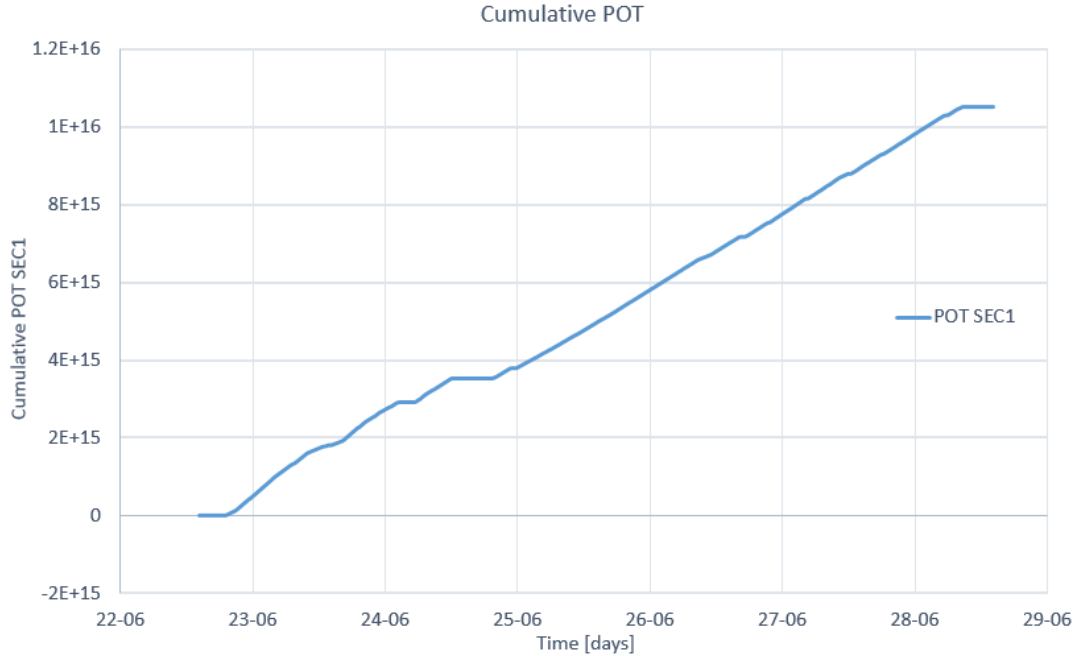


Figure 6.2: integrated POT in time. They are almost proportional to the time when there are not losses at PS and the target is in position. Almost all of these stationary traits like that between 24-06 and 25-06 are due to beam losses at PS so that there are no spill entering at the irradiation chamber.

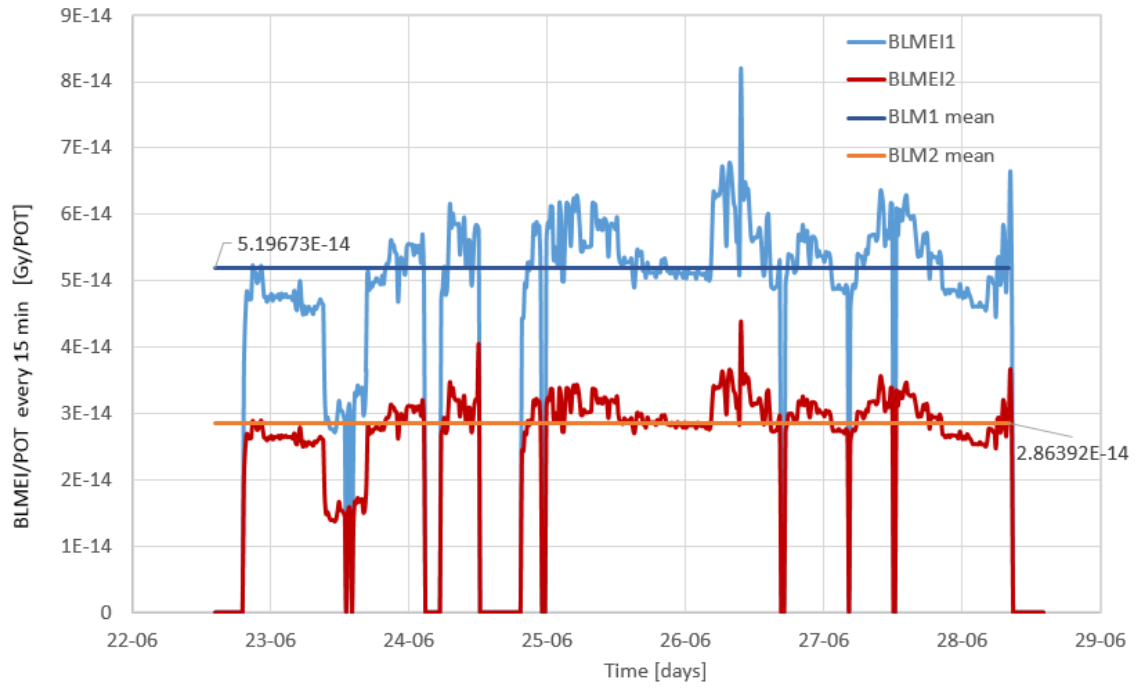


Figure 6.3: ratio between BLM values and effective POT at CHARM, for both BLM1 and BLM2. BLM1 is that closer to the beam, BLM2 is behind the shielding. They have the same trend but different dose intensity [Gy]. What it's used for the knowledge of the selected target is the average of the two detectors normalized with the POT intensity.

Week	Target	Integrated POTs with target	Time [h]	BLM1 average [Gy/s]	BLM2 average [Gy/s]	BLM1 dose [Gy]	BLM2 dose [Gy]
W24	Cu_OOOO	1.19E+16	136	1.8E-03	9.6E-04	558.4	300.9
W25	Cu_OOOO	1.05E+16	120.75	1.5E-03	8.3E-04	548.8	302.7
W26	Cu_CIIC	1.15E+16	132.5	2.0E-03	6.6E-05	651.4	21.6
W27	Cu_OOOO	1.18E+16	137	1.8E-03	9.7E-04	596.0	321.7
W28	Cu_OOOO	1.29E+16	139.25	2.1E-03	1.1E-03	698.9	377.9
W29	Cu_OOOO	1.23E+16	127.5	2.2E-03	1.2E-03	662.8	364.0
W30a	Cu_CIOO	8.58E+14	10	1.6E-03	1.1E-04	48.5	3.5
W30b	Cu_OOOO	9.95E+15	108	1.9E-03	1.0E-03	532.1	287.5
W31	Cu_OOOO	1.23E+16	134.75	2.0E-03	1.1E-03	656.4	356.6
W32	Cu_CIIC	8.95E+15	105.75	1.7E-03	5.7E-05	528.2	17.5
W33	Cu_CIIC	9.40E+15	111.75	1.3E-03	4.3E-05	557.2	18.3
W36a	Cu_OOOO	3.50E+15	43	1.1E-05	4.6E-06	1.2	0.5
W36b	CU_CIIC	5.30E+15	67	1.2E-05	1.9E-06	2.0	0.3
W37	Cu_OOOO	7.74E+15	90.5	1.6E-03	8.2E-04	400.1	207.2
W38	Cu_OOOO	9.00E+15	132.5	1.4E-03	7.1E-04	480.3	243.0
W39	Cu_OOOO	1.22E+16	136.25	2.1E-03	1.1E-03	682.9	352.7
W40a	Cu_CIIC	1.23E+15	19.25	1.5E-03	4.9E-05	80.0	2.6
W40b	CU_OOOO	1.21E+16	116	2.6E-03	1.3E-03	723.8	370.1
W41	CU_OOOO	1.30E+16	123.25	2.5E-03	1.3E-03	768.0	399.6
W42	CU_OOOO	1.28E+16	124	2.2E-03	1.2E-03	677.4	354.7
W43	CU_OOOO	1.24E+16	120.5	2.2E-03	1.1E-03	616.1	316.9
W44	CU_OOOO	1.38E+16	122	2.6E-03	8.8E-05	734.7	24.6
W45	CU_OOOO	1.04E+16	109	2.1E-03	1.1E-03	513.7	263.6

Table 6.1: BLMs values (first part) - 2016

- The time period is retrieved in UTC time (and not Local time) starting the acquisition before the first spill of the run and ending it after the last one.
- The target configurations are retrieved from a variable in TIMBER and checked in the logbook a web-page on the CHARM status.
- Integrated POTs with target are the total POT arrived inside CHARM in the corresponding week when the target was in position, considering the BLM1 detector. They are computed by summing the single POT when the BLM1 dose rate is not lower than ten times its mean value in [Gy/s]. This threshold has been implemented

to discriminate those spills that do not impact against the target; the nominal BLM1 values varies according to the shielding and target and is displayed in the BLM average column. The threshold is not zero because very low values of BLMs may be present in the event the target is not in position.

- BLM1 average [Gy/s] is the arithmetic mean of all the values measured from the BLM1.
- BLM1 dose [Gy] is the integrated dose in time, measured from the BLM1. It's calculated by adding all the BLM1 values and multiplying them by a correction of 358,14 as explained before (655,36 ms to 1 second conversion factor).
- Total BLM/POT average: the underlying BLM1 and BLM2 columns are related to the ratio between the BLMs and relative POTs. The BLM/POT ratio was calculated every 15 minutes where both the values rely to the same 15 min range time
- BLM1/BLM2 is the final result of the previous data. It shows the opportunity of figuring out which type of shielding configuration was laying inside the chamber, the aim of this analysis. As can be seen from tables, same target configurations lead to similar ratio within an uncertainty, assessed in the next columns.
- BLM/POT standard deviation computes the sample standard deviation always excluding those BLMs values that do not concern the impact of spills on the target.

$$stdv = \sqrt{\frac{\sum_{i=1}^n (x_i - \bar{x})^2}{n}} \quad (6.5)$$

where x_i are all the sample values, n the sample size, \bar{x} the expected value on the samples. In addition, the percentage of deviation with respect to the BLM/POT value is showed alongside.

- Max value is the greatest value assumed during the run from the BLM/POT.

Week	Total BLM/POT average [Gy/POT]		BLM1/ BLM2	BLM/POT standard deviation				Max value [Gy/POT]	
	BLM1	BLM2		BLM1	BLM1 % avg	BLM2	BLM2 % avg	BLM1	BLM2
W24	4.68E-14	2.52E-14	1.85	3.49E-15	7.5	2.04E-15	8.1	6.24E-14	3.29E-14
W25	5.20E-14	2.86E-14	1.81	7.35E-15	14.2	4.24E-15	14.8	8.18E-14	4.37E-14
W26	5.49E-14	1.82E-15	30.19	5.26E-15	9.6	1.71E-16	9.4	1.10E-13	2.00E+00
W27	4.85E-14	2.62E-14	1.85	4.34E-15	9.0	2.32E-15	8.9	6.23E-14	3.32E-14
W28	5.14E-14	2.78E-14	1.85	4.38E-15	8.5	2.47E-15	8.9	6.56E-14	3.56E-14
W29	5.37E-14	2.96E-14	1.82	5.19E-15	9.7	2.74E-15	9.3	6.88E-14	3.81E-14
W30a	5.64E-14	4.08E-15	13.82	4.20E-15	7.5	3.03E-16	7.4	6.47E-14	4.68E-15
W30b	5.36E-14	2.91E-14	1.84	4.24E-15	7.9	2.31E-15	7.9	6.69E-14	3.62E-14
W31	5.36E-14	2.92E-14	1.84	4.57E-15	8.5	2.34E-15	8.0	6.82E-14	3.71E-14
W32	5.88E-14	1.95E-15	30.20	4.64E-15	7.9	1.43E-16	7.3	7.33E-14	2.38E-15
W33	5.92E-14	1.95E-15	30.36	5.12E-15	8.7	1.71E-16	8.7	7.65E-14	2.68E-15
W36a	3.52E-16	1.46E-16	2.41	3.29E-17	9.4	1.51E-17	10.3	5.36E-16	2.56E-16
W36b	3.73E-16	1.01E-16	3.68	4.96E-17	13.3	7.68E-18	7.6	5.45E-16	1.01E-16
W37	5.16E-14	2.67E-14	1.93	6.28E-15	12.2	3.47E-15	13.0	6.07E-14	3.14E-14
W38	5.31E-14	2.67E-14	1.99	8.33E-15	15.7	5.50E-15	20.6	7.39E-14	3.81E-14
W39	5.63E-14	2.90E-14	1.94	6.17E-15	11.0	3.36E-15	11.6	9.64E-14	5.01E-14
W40a	6.50E-14	2.11E-15	30.76	3.10E-15	4.8	9.74E-17	4.6	7.34E-14	2.38E-15
W40b	5.99E-14	3.05E-14	1.96	4.03E-15	6.7	2.79E-15	9.1	7.60E-14	3.88E-14
W41	5.91E-14	3.07E-14	1.92	5.05E-15	8.5	2.70E-15	8.8	8.14E-14	4.23E-14
W42	5.31E-14	2.77E-14	1.91	3.85E-15	7.3	2.31E-15	8.3	6.96E-14	3.62E-14
W43	4.98E-14	2.56E-14	1.95	5.60E-15	11.2	3.23E-15	12.6	7.82E-14	4.07E-14
W44	5.40E-14	1.81E-15	29.92	5.24E-15	9.7	1.73E-16	9.6	7.88E-14	2.61E-15
W45	4.96E-14	2.55E-14	1.95	3.70E-15	7.5	1.92E-15	7.5	6.36E-14	3.28E-14

Table 6.2: BLMs values (second part) - 2016

Week 2017	Target	Integrated POTs with target	Time [h]	BLM1 average [Gy/s]	BLM2 average [Gy/s]	BLM1 dose [Gy]	BLM2 dose [Gy]	BLM1/BLM2
W44	Cu_CIIC	1.38E+16	122	1.4E+00	4.8E-02	731.0	24.4	29.9
W45	Cu_OOOO	1.04E+16	109	2.1E-03	1.1E-03	513.7	263.6	1.9
W45	Cu_OOOO	1.04E+16	109	1.1E+00	5.9E-01	510.7	262.1	1.9
W19	Cu_CIIC	3.61E+14	3.55	9.0E-02	3.1E-03	21.4	0.7	29.3
W19	Cu_CIIC	5.16E+14	5.15	7.2E-02	2.4E-03	29.8	1.0	29.5
W19	Cu_CIIC	8.41E+14	7.6	5.7E-02	2.0E-03	49.0	1.7	29.0
W19	Cu_OOOC	1.34E+14	1.53333	4.1E-02	1.5E-02	7.9	2.9	2.7
W19	Cu_OOOO	2.01E+14	2.48333	5.32E-02	2.9E-02	11.5	6.4	1.8
W19	ALH_OOOO	3.09E+14	3.76667	1.85E-02	6.4E-03	4.2	1.4	2.9
W19	ALH_CIOO	2.54E+14	3.65	1.71E-02	6.6E-04	3.8	0.1	25.9
W19	ALH_CIIC	7.67E+14	8.2	1.52E-02	4.2E-04	11.5	0.3	35.9
W20	Cu_CIIC	5.38E+14	5.28333	5.72E-02	1.94E-03	32.6	1.1	29.5
W20	Cu_CIIC	5.61E+14	8.41667	2.48E-02	8.33E-04	34.2	1.1	29.8
W21	Cu_CIOO	3.06E+14	3.3	7.51E-02	3.32E-03	11.3	0.5	22.6
W21	Cu_OOOO	8.61E+15	89.35	1.96E-01	1.04E-01	450.9	240.6	1.9
W22	Cu_OOOO	9.96E+15	110.45	2.11E-01	1.12E-01	507.5	267.6	1.9
W23	Cu_OOOO	8.41E+15	82.3	2.08E-01	1.10E-01	431.7	227.5	1.9

(a) BLMs values (first part) - 2017.

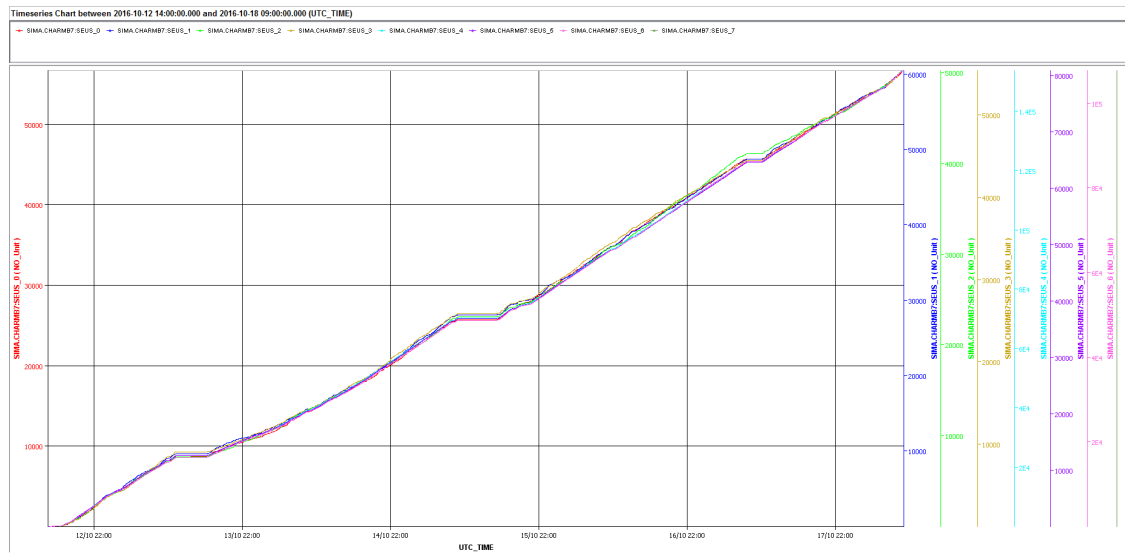
Week 2017	Total BLM/POT average [Gy/POT]		BLM1/BLM2	BLM/POT standard deviation				Max value [Gy/POT]	
	BLM1	BLM2		BLM1	BLM1 % avg	BLM2	BLM2 % avg	BLM1	BLM2
W44	5.31E-14	1.77E-15	29.91	5.39E-16	1.0	2.57E-17	1.4	5.51E-14	2.11E-15
W45	4.96E-14	2.55E-14	1.95	3.70E-15	7.5	1.92E-15	7.5	6.36E-14	3.28E-14
W45	4.91E-14	2.52E-14	1.95	1.73E-15	3.5	9.15E-16	3.6	5.59E-14	2.88E-14
W19	5.98E-14	2.04E-15	29.29	8.84E-15	14.8	2.71E-16	13.3	8.72E-14	2.97E-15
W19	5.85E-14	2.00E-15	29.34	9.58E-15	16.4	3.10E-16	15.5	8.93E-14	3.03E-15
W19	5.86E-14	2.00E-15	29.33	9.33E-15	15.9	3.02E-16	15.1	8.93E-14	3.03E-15
W19	5.89E-14	2.16E-14	2.73	2.47E-16	0.4	2.82E-15	13.0	5.93E-14	3.20E-14
W19	5.8E-14	3.2E-14	1.81	1.11E-14	19.1	6.15E-15	19.1	1.15E-13	6.35E-14
W19	1.4E-14	4.7E-15	2.91	2.02E-15	14.7	7.93E-16	16.8	2.13E-14	7.33E-15
W19	1.5E-14	5.7E-16	25.86	2.87E-15	19.4	1.10E-16	19.2	3E-14	1.17E-15
W19	1.5E-14	4.1E-16	36.05	2.97E-15	20.0	8.14E-17	19.7	4.34E-14	1.2E-15
W20	6.1E-14	2E-15	29.91	9.8E-15	15.9	3.3E-16	15.9	1.2E-13	4.03E-15
W20	6.2E-14	2.1E-15	30.22	1.3E-14	21.1	4.3E-16	20.9	1.27E-13	4.24E-15
W21	3.7E-14	1.6E-15	22.73	1.7E-14	46.0	9.1E-16	55.8	6.04E-14	2.85E-15
W21	5.2E-14	2.8E-14	1.8718	1.7E-15	3.3	1E-15	3.7	6.06E-14	3.29E-14
W22	5.1E-14	2.7E-14	1.9022	4.3E-15	8.4	2.5E-15	9.4	6.07E-14	3.4E-14
W23	5.1E-14	2.7E-14	1.8973	2E-15	3.9	1.1E-15	4.1	6.21E-14	3.28E-14

(b) BLMs/POT values (second part) - 2017.

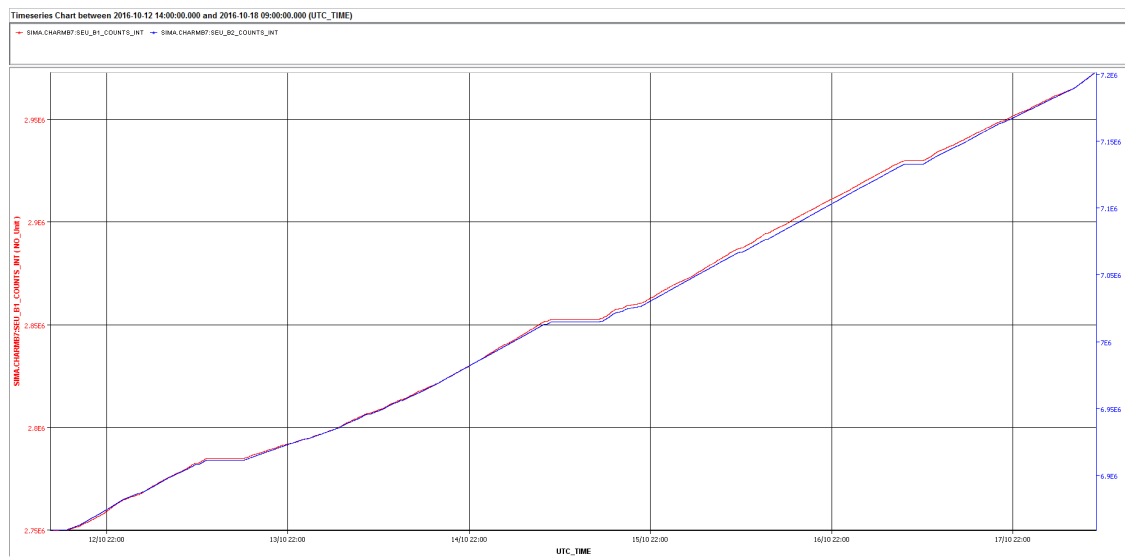
Table 6.3: BLM analysis during 2017.

RadMon: Toshiba and Cypress memories observations

For every week, from TIMBER can be plotted the SEU vs time trend for both Cypress and Toshiba memories of the RadMon (figures below). They can be plotted for each single memory (4 Cypress and 4 Toshiba as in Figure 20, Figure 22) or the cumulative value of the two memories (Figure 21, Figure 23) where for every instant of time the SEU values of the four memory of the same type are added together. The plots are shown with different scale to see if the curves follow the same behaviour. Usually they appear as in Figure 20 or Figure 21 but for W44 the RadMon 7 recorded an abrupt trend for the Cypress memory number 0, between 23:00 of 06/11/16 and the following day (Figure 22, Figure 23) also if the final behaviour is compatible with the others. The problem related to this unusual behaviour seems start immediately on 02/11/16, but as only the initial and final value have been used to extract the total number of SEU occurred and in these two times the memory SEU $_ 0$ seemed to work well, the NSEU is supposed to be correct. Also, note that this problem happened in the only week when Cu-CIIC configuration was used.

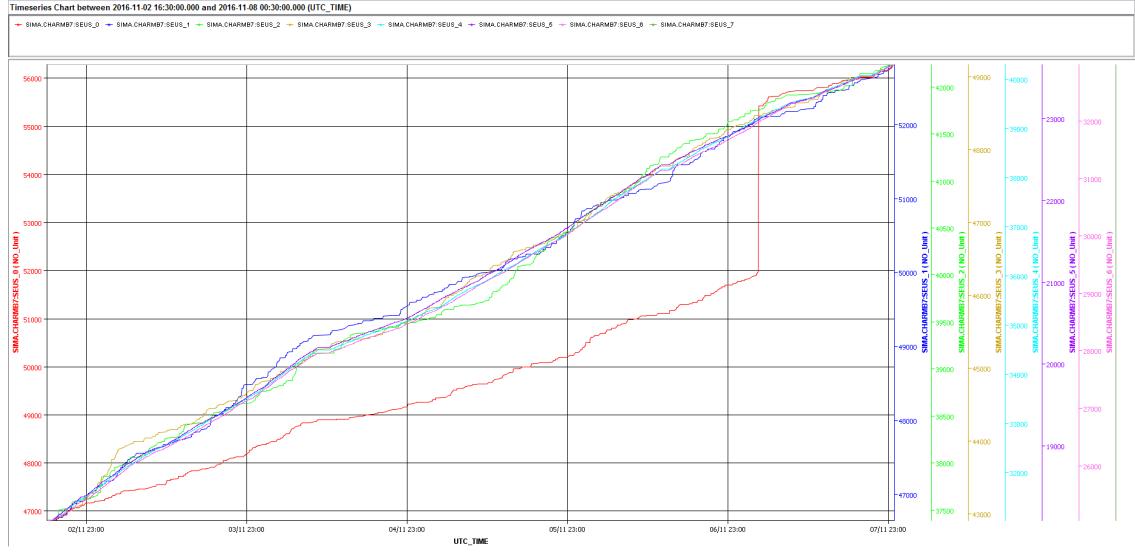


(a) *W41 M0 RadMon 7 Cypress 0123 Toshiba 4567, SEUs single memories.*

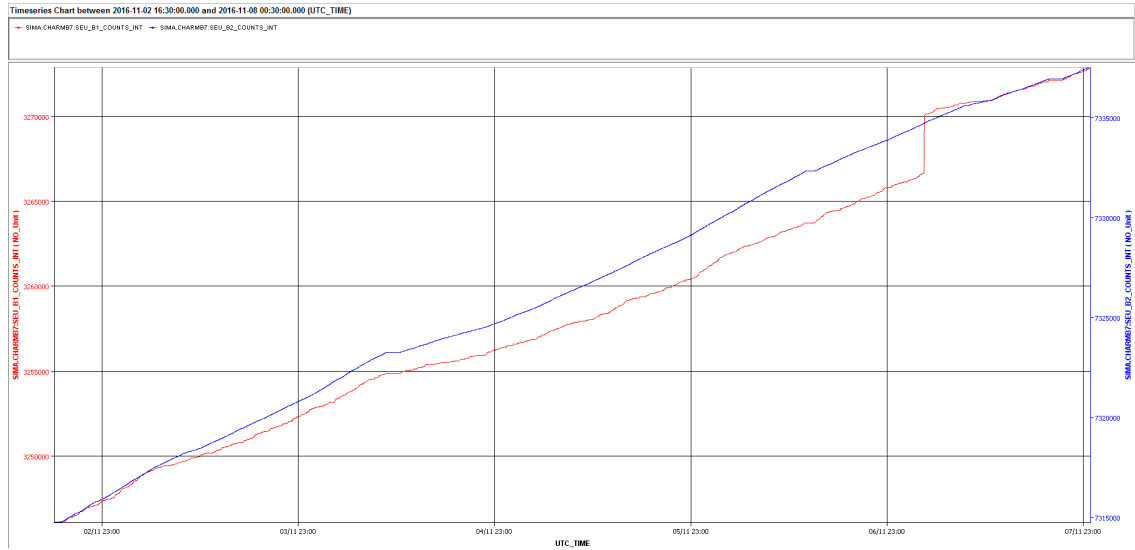


(b) *W41 M0 RadMon 7 Cypress (red) and Toshiba (blue), cumulative SEUs for all the four memories..*

Table 6.4: W41 Radmon 7 on M0, Toshiba and Cypress SEU behaviour.



(a) *W44 M0 RadMon 7 Cypress 0123 Toshiba 4567, SEUs single memories..*



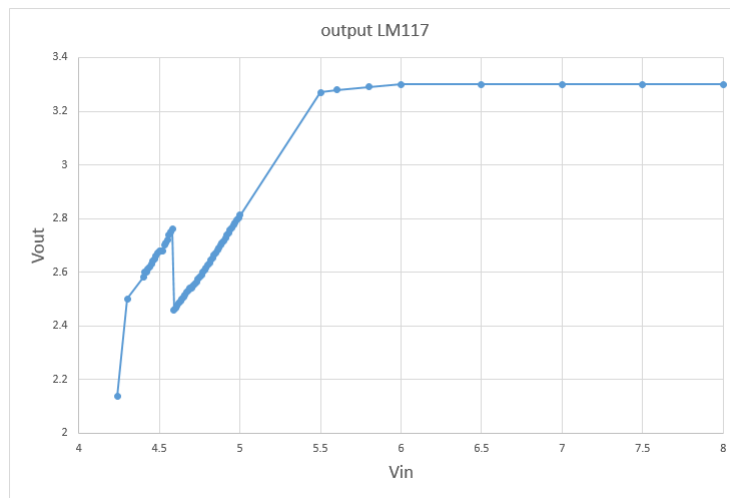
(b) *W44 M0 RadMon 7 Cypress (red) and Toshiba (blue), cumulative SEUs for all the four memories..*

Table 6.5: W44 Radmon 7 on M0, Toshiba and Cypress SEU behaviour..

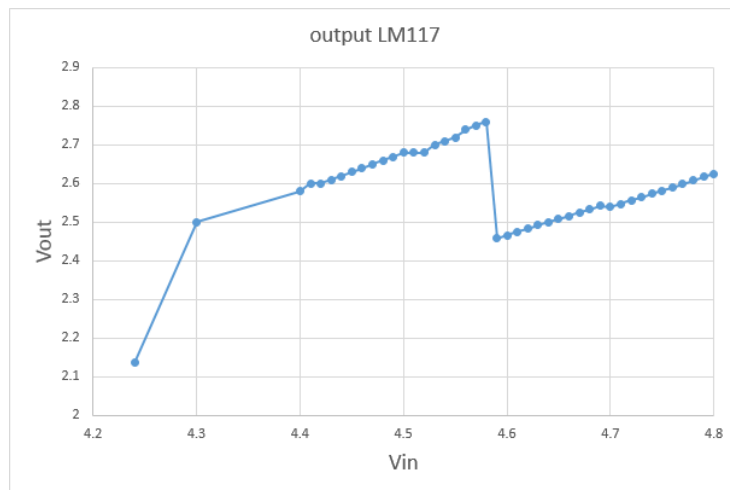
ESA Monitor data communication loss

Several times the communication for reading the memory has been lost. One of the problems was the 5 V power supply. The ESA Monitor board has a voltage regulator that supply the memory to 3.3 V as nominal voltage. The latter is a typical LM117 and it ensures an output voltage of 3.3 V, whenever in input is applied a voltage that satisfy the inequality $3V \leq V_{in} - V_{out} \leq 40V$. Considering the first inequality and imposing 3.3 V as output, the input voltage must be at least 6.6 V. Since the memory can work

within the range of $3.3 \pm 0.3V$ the minimum theoretical voltage is suppose to be of 3 V and therefore 6.3 V as input. Probably the limits of the data-sheet are more restrictive of those measured during normal operation of the board as shown below. By plotting the output voltage as a function of the input voltage (Figure 6.4) measured between GND and the output of the regulator, by using an external adjustable power supply the board operates well up to a minimum input of 4.7 V. With a further voltage reduction, the communication stops and V_{out} increases a little owing to the board LEDs switching-off. A further decrease likely produces some instability effects. On the other way, increasing the voltage after 6 V of input, the output remains constant to 3.3 V.



(a) Output voltage as a function of the input voltage on the board.



(b) zoom over the unstable area around an input voltage of 4.7 V when the communication is lost.

Figure 6.4: ESA Monitor 1104 voltage functioning ranges.

Acknowledgements

I would like to express my gratitude to all the people that helped me along the way of performing my work for this master's thesis.

I want to thank my Professor Simone Gerardin for introducing me into the world of the radiation to electronics with his fondness and knowledge.

Special thanks goes out to the best Supervisor I could have wished Rubén García Alía, who cared so much about my work offering invaluable advices and who answered to my questions so promptly.

Additionally, I want to thank them for always taking the time to proofread all the presentations I held during my time and, together with Markus Brugger, for providing me this unique opportunity of developing this thesis at CERN.

I would also like to thank Angelo Infantino and Fabio Pozzi for helping me with the FLUKA simulations, providing essential inputs.

Finally, I would like to thank my parents for their provided support and all my CERN friends for the good time spent together.

Bibliography

- [1] Robert C. Baumann, Eric B. Smith, *Neutron-induced 10B fission as a major source of soft errors in high density SRAMs*, 2000.
- [2] A. Thornton, *CHARM Facility Test Area Radiation Field Description*, CERN-ACC-NOTE, 2016.
- [3] J. Mekki, *CHARM Secondary Emission Chamber*, CERN EDMS 1553668/1.
- [4] *McGraw-Hill Concise Encyclopedia of Physics*, 2002.
- [5] A. Tsinganis, F. Cerutti, *Energy deposition from collision debris in the LHC and HL-LHC*, indico.cern.ch, April 2017.
- [6] A. Infantino, *CHARM Integral data*, 2016.
- [7] S. Bonaldo, *CHARM - Una nuova facility del CERN per test di elettronica con spettri misti di radiazione ionizzante*, Master Thesis, 2015/2016.
- [8] R. G. Alia M. Brugger, S. Danzeca et al., *Single event effects in high-energy accelerators*, Feb. 2017.
- [9] R. G. Alia et al., *Simplified SEE Sensitivity Screening for COTS Components in Space*, IEEE Trans. Nucl. Sci., vol. 64, no. 2, pp. 882-890, Jan. 2017.
- [10] S. Gerardin, *Corso di Qualità e Affidabilità in Elettronica: Single Event Effects*, 2015/2016.
- [11] R. G. Alia et al., *ESA Monitor CHARM in-beam measurement*, CERN EDMS 1554539.1, June 2015.
- [12] <http://www.analog.com>
- [13] A. Infantino, M. Cecchetto, R. Garcia Alia, et al., *CERN test campaign in Grenoble*, 2017.

- [14] Gary M. Swift, *SEE Testing Lessons from Dickens, Scouting, and Oz*, Jet Propulsion Laboratory, California Institute of Technology.
- [15] <https://radhome.gsfc.nasa.gov/radhome/papers/seeca4.htm>
- [16] JEDEC STANDARD *Measurement and Reporting of Alpha Particle and Terrestrial Cosmic Ray-Induced Soft Errors in Semiconductor Devices*, 2012.
- [17] F. Pozzi, *User manual to operate the irradiators of the RP calibration laboratory*, CERN EDMS 1539975, 22 Feb. 2016.
- [18] F. Pozzi, *CERN Radiation Protection (RP) calibration facilities*, PhD Thesis, July 2016.
- [19] R. G. Alia et al., *SEE cross section calibration and application to quasi-monoenergetic and spallation facilities*, sept. 2017.
- [20] *Beam intensity monitoring at the IRRAD proton facility*, CERN EDMS 1554165, 2015.
- [21] <http://www.fluka.org>
- [22] K. Roed, M. Brugger, D. kramer et al., *Method for measuring mixed field radiation levels relevant for SEEs at the LHC*, IEEE Trans. Nucl. Sci., vol. 59, no. 4, pp. 1040-1047, Aug. 2012.
- [23] F. Wrobel, J.-M. Palau, M.-C. Calvet, and P. Iacconi, *Contribution of SiO₂ in Neutron-Induced SEU in SRAMs*, IEEE Transactions on Nuclear Science, Vol. 50, No.6, Dec. 2003.
- [24] K. Roed, M. Brugger, C. Pignard, *PTB Irradiation tests of the LHC Radiation Monitor (RadMon)*, CERN-ATS-Note-2011-012.
- [25] R. Garcia Alia, *Radiation Fields in High Energy Accelerators and their impact on Single Event Effects*, PhD Thesis, Dec. 2014.
- [26] R. Garcia Alia, M. Brugger, S. Danzeca, V. Ferlet-Cavrois et al., *SEL Hardness Assurance in a Mixed Radiation Field*, IEEE Trans. Nucl. Sci., vol. 62, no. 6, pp. 2555-2562, Dec. 2015.
- [27] S. Uznanski, *System Level Radiation Qualification of COTS-based Control Systems for High Energy Accelerator Applications*, submitted for publication - NSREC 2017.

- [28] D. Lambert, J. Baggio, G. Hubert et al., *Analysis of Quasi-Monoenergetic Neutron and Proton SEU Cross Sections for Terrestrial Applications*, IEEE Trans. Nucl. Sci., vol. 53, no. 4, pp. 1890-1896, Aug. 2006.
- [29] Brian D. Sierawski, Kevin M. Warren, Robert A. Reed, Robert A. Weller, et al., *Contribution of Low-Energy (< 10 MeV) Neutrons to Upset Rate in a 65 nm SRAM*, Reliability Physics Symposium (IRPS), 2010 IEEE International, June 2010.
- [30] D. Kramer, M. Brugger, V. Klupak, C. Pignard, K. Roeed, G. Spiezia, L. Viererbl, and T. Wijnands, *LHC RadMon SRAM Detectors Used at Different Voltages to Determine the Thermal Neutron to High Energy Hadron Fluence Ratio*, IEEE Trans. Nucl. Sci., vol. 58, no. 3, pp. 1117-1122, June 2011.
- [31] J. L. Autran, S. Serre, S. Semikh, D. Munteanu, et al., *Soft-Error Rate Induced by Thermal and Low Energy Neutrons in 40 nm SRAMs*, IEEE Trans. Nucl. Sci., vol. 59, no. 6, pp. 2658-2665, Dec. 2012.
- [32] Shin-ichiro Abe and Yukinobu Watanabe, *Analysis of Charge Deposition and Collection Caused by Low Energy Neutrons in a 25-nm Bulk CMOS Technology*, IEEE Trans. Nucl. Sci., vol. 61, no. 6, pp. 3519-3526, Dec. 2014.
- [33] Takashi Yamazaki, Takashi Kato, Taiki Uemura et al., *Origin analysis of thermal neutron soft error rate at nanometer scale*, Journal of Vacuum Science and Technology B, 2015.
- [34] J. Mekki, M. Brugger, R. G. Alia, A. Thornton, N. C. Dos Santos Mota, and S. Danzeca, *CHARM: A Mixed Field Facility at CERN for Radiation Tests in Ground, Atmospheric, Space and Accelerator Representative Environments*, IEEE Trans. Nucl. Sci., vol. 63, no. 4, pp. 2106-2114, Aug. 2016.
- [35] S. Danzeca, G. Spiezia, M. Brugger, L. Dusseau, G. Foucard, R. Garcia Alia, P. Mala, A. Masi, P. Peronnard, J. Soltes, A. Thornton, and L. Viererbl *Qualification and Characterization of SRAM Memories Used as Radiation Sensors in the LHC*, IEEE Trans. Nucl. Sci., vol. 61, no. 6, pp. 3458-3465, Dec. 2014.
- [36] G. Spiezia, P. Peronnard, A. Masi, M. Brugger, M. Brucoli, S. Danzeca, R. Garcia Alia, R. Losito, J. Mekki, P. Oser, R. Gaillard, *A New RadMon Version for the LHC and its Injection Lines*, IEEE Trans. Nucl. Sci., vol. 61, no. 6, pp. 3424-3431, Dec. 2014.

- [37] R. Secondo, G. Foucard, S. Danzeca, R. Losito, P. Peronnard, A. Masi, M. Brugger, and L. Dusseau, *Embedded Detection and Correction of SEU Bursts in SRAM Memories Used as Radiation Detectors*, IEEE Trans. Nucl. Sci., vol. 63, no. 4, pp. 2168-2175, Aug. 2016.
- [38] R. Harboe-Sorensen, C. Poivey, et al., *From the Reference SEU Monitor to the Technology Demonstration Module On-Board PROBA-II*, IEEE Trans. Nucl. Sci., vol. 55, no. 6, pp. 3082-3087, Dec. 2008.
- [39] Yi-Pin Fang and A. S. Oates, *Thermal Neutron-Induced Soft Errors in Advanced Memory and Logic Devices*, IEEE Trans. Dev. Mat. Reliab., vol. 14, no. 1, pp. 583-586, March 2014.
- [40] Damien Lambert, Francois Desnoyers and Didier Thouvenot, *Investigation of neutron and proton SEU cross-sections on SRAMs between a few MeV and 50 MeV*, RADECS Conference, Sept. 2009.
- [41] R. Garcia Alia, Markus Brugger, Salvatore Danzeca, et al., *SEL Hardness Assurance in a Mixed Radiation Field*, IEEE Trans. Nucl. Sci., vol. 62, no. 6, pp. 2555-2562, Dec. 2015.
- [42] R. Garcia Alia, Markus Brugger, Eamonn Daly, et al. *Simplified SEE Sensitivity Screening for COTS Components in Space*, IEEE Trans. Nucl. Sci., vol. 64, no. 2, pp. 882-890, Feb. 2017.
- [43] R. Garcia Alia, A. Thornton *CHARM Montrac Blown-up Beam Characterization using Aluminium Foils, June 2015*, CERN EDMS 1554364 v.1, Oct. 2015.